Thermal Modelling of Power Semiconductor Modules in Power Electronic Applications



A thesis submitted for the degree of Doctorate in Philosophy

Khaled Redwan Choudhury

Wolfson College

University of Oxford

Michaelmas 2020

Abstract

The power module is an important building block of a power electronic converter used in high power applications. It provides the placement of power semiconductor devices. One of the most important design constraints of power module is maximum junction temperature of semiconductor devices. Therefore, thermal modelling of the power module is important because it gives the maximum junction temperature of the devices. There are three different approaches to do the thermal modelling of the power module: analytical, finite element analysis and thermal network. In this work, the steady-state and transient thermal modelling of a rectangular N-layer structure with an arbitrary number of heat sources on the top surface is obtained by a Fourier series solution based on the separation of variables method. Although a typical power module does not exactly resemble an N-layer rectangular structure but it can be closely approximated as the latter. As the structure of power modules can be closely approximated as a rectangular N-layer structure. Various simplified structures are analyzed to understand the effects of structural approximation on the temperature field.

The steady-state model (RNLF method) is compared with the finite-element method simulation, and an excellent matching (approximately maximum 1.00% temperature error) is found in the centres of the semiconductor dies for this case. Experimental temperature measurements taken at the surface of a commercial SiC power module are also presented demonstrating agreement in the centres of the dies to within 3.5%. The transient model is compared with a finite-element model and an excellent matching (less than 2% error) in the transient region is found in the centres of semiconductor dies. However, in the sub-transient region (this is the region where the rate of die temperature rise is much higher), the error is higher (approximately 15% error) because of finite thermal conductivity of the semiconductor material (SiC is used here). An experimental validation is performed using a high frame-rate thermal camera. After the model outputs have been compensated to match the limited frequency response of the camera, a good agreement is found between model and experiment (less than 6% error). For the points where the rate of rise of temperature is relatively slow, this compensation is not necessary.

Acknowledgements

First and foremost, I would like to express my gratitude to the almighty God without whom I could not even start my research work. After that, I would like to express my sincere gratitude to my supervisor Dr. Daniel Rogers for his continuous support, advice and encouragement in every step of my journey as a DPhil student. His knowledge, enthusiasm and guidance helped me finish this research project and write the thesis. I do not have enough words to thank my parents and wife for their unwavering support through the highs and lows of my life as a research student. I cannot think what would happen if there was no support from them, especially from my wife.

I am also grateful to the authority of Department of Engineering Science at the University of Oxford and the Government of Peoples' Republic of Bangladesh for the financial support for my research work.

At last but not least, I would like to thank my colleagues and friends at various stages of my journey, especially Mohammed Amir Eleffendi, Kawsar Ali and Kevin R. Bagnall who have helped me by giving valuable suggestions and support.

Contents

1 Introduction **21**

1.1 Introduction to Power Electronics 21

1.2 Importance and applications of power electronics in the modern world 23

1.3 Introduction to power modules 29

1.3.1 Definition and examples of power module 29

1.3.2 Structure of a typical power module 30

1.3.3 Comparison between discrete devices and power module 32

1.3.4 Discussion on different materials and manufacturing technologies of power module 34

1.4 Wide bandgap semiconductor-based power module 37

1.5 Motivation 39

1.6 Structure of the thesis 42

1.7 Contribution of this work 42

2 Background **44**

2.1 Introduction 44
2.2 Origin of losses in hard-switched converters 44
2.3 Structure of a SiC power MOSFET 48
2.4 The concept of junction temperature 50
2.5 Different modes of heat transfer and heat transfer in power modules 52
2.6 Equation of heat diffusion 55
2.7 Different approaches to the thermal modelling of semiconductor packages 57
2.7.1 Analytical and semi-analytical approaches 57
2.7.2 Finite element-based or finite-difference based approaches 62
2.7.3 Thermal network-based approaches 63
2.8 Methods of measurement and estimation of junction temperature of power semiconductor devices in power modules 69

3 Steady-state and transient thermal modelling of a rectangular N-layer structure 76

3.1 Mathematical background 76
3.1.1 Separation of variables 77
3.1.2 Application of the separation of variables method for the steady-state case 78
3.1.3 Application of the separation of variables for the transient case 85

3.2 Steady-state thermal modelling of an N-layer rectangular structure . . . 91
3.2.1 Problem Statement . . . 91
3.2.2 Problem Solution: Rectangular $N-$ Layer Fourier method (RNLF Method) . . . 93
3.3 Transient thermal modelling of an N-layer rectangular structure 101
3.3.1 Problem Statement . . . 101
3.4 Problem Solution: Transient Rectangular N- Layer Fourier method (TRNLF Method) . . . 104
3.4.1 Generalised Orthogonal Expansion Technique . . . 106
3.4.2 Determination of $A_{00\bar{l}}$, $A_{\bar{m}0\bar{l}}$, $A_{0\bar{n}\bar{l}}$ and $A_{\bar{m}\bar{n}\bar{l}}$ . . . 110

4 Verification of the thermal models by COMSOL Multiphysics 118

4.1 Validation of the steady-state model by simulation . . . 119
4.2 Convergence analysis of the steady-state thermal model . . . 122
4.3 Application of the thermal model of an N-layer structure to a power module . . . 124
4.3.1 The RNLF method and the simulation of different structures . . . 124
4.3.2 Simulation results and relevant discussion . . . 128
4.3.3 Comparison of the computational time . . . 134
4.4 Some applications of the RNLF method . . . 134
4.4.1 Thermal spreading resistance . . . 135

4.4.2 Temperature distribution in different layers 137
4.5 Effect of the patterned Copper layer on the temperature distribution 140
4.6 Validation and convergence of the transient thermal model or TRNLF method by COMSOL Multiphysics 142
4.7 Application of the TRNLF method for the transient thermal modelling of a power module 144
4.7.1 Simulation results and discussion 145
4.7.2 Comparison of the computational time 147

5 Experimental verification of the steady-state and transient modelling 149

5.1 Experimental set-up 149
5.1.1 Mechanical set-up 150
5.1.2 Preparation of the module 152
5.1.3 Electrical set-up 153
5.2 Validation of the models 155
5.2.1 Validation of the steady-state model 156
5.2.2 Validation of transient thermal model 160

6 Conclusion 166

6.1 Discussion on the merits and limitations of the RNLF and TRNLF methods 167
6.2 Future work 169

Nomenclature

α	Thermal diffusivity
α_{spread}	Spreading angle
β	Separation constant
β_{mn}	Eigenvalue in the y direction
δ_n	Eigenvalue in the y direction
ϵ	Emissivity
η	Separation constant
$\hat{i}$	Unit vector in the direction of x axis
$\hat{j}$	Unit vector in the direction of y axis
$\hat{k}$	Unit vector in the direction of z axis
λ_m	Eigenvalue in the x direction
ν	Separation constant

ρ	Material density
σ	Stefan-Boltzman constant
τ_i	Thermal time-constant
τ_n	Thermal time-constant
θ	Temperature rise with respect to ambient
θ_i	Temperature rise of the i^{th} layer of a rectangular N-layer structure with respect to ambient
θ_s	Steady-state solution of the temperature field
θ_t	Transient solution of the temperature field
$\vec{E}$	Electric field vector
$\vec{J}$	Current density vector
a	Length of a rectangular N-layer structure
$A_{\bar{m}\bar{n}\bar{l}}$	A Fourier coefficient in the transient temperature field of the i^{th} layer of the N-layer structure
A_{i0}	A Fourier coefficient in the steady-state temperature field of the i^{th} layer of the N-layer structure
A_{imn}	Fourier coefficient in the steady-state temperature field of the i^{th} layer of the N-layer structure

A_{im} A Fourier coefficient in the steady-state temperature field of the i^{th} layer of the N-layer structure

A_{in} A Fourier coefficient in the steady-state temperature field of the i^{th} layer of the N-layer structure

b Width of a rectangular N-layer structure

B_{i0} A Fourier coefficient in the steady-state temperature field of the i^{th} layer of the N-layer structure

B_{imn} Fourier coefficient in the steady-state temperature field of the i^{th} layer of the N-layer structure

B_{im} Fourier coefficient in the steady-state temperature field of the i^{th} layer of the N-layer structure

B_{in} A Fourier coefficient in the steady-state temperature field of the i^{th} layer of the N-layer structure

C Capacitance

c Length of a heat source (chip)

c_p Specific heat capacity

d Width of a heat source (chip)

g Heat generation

h Convective heat transfer coefficient

I_L Load current

k Thermal conductivity

Q Heat generated by each heat source of the rectangular N-layer structure

$q(\hat{r}, t)$ heat flux vector representing heat flow per unit of time, per unit area of the isothermal surface in the direction of the decreasing temperature gradient

q_{conv} Convective heat flux

q_{rad} Radiative heat flux

R Resistance

R_{th} Thermal resistance

T Temperature

T_a Ambient temperature

t_i Thickness of the i^{th} layer of a rectangular N-layer structure

T_∞ Tempearture of the surroinding fluid

V_p Miller plateau voltage

V_{DS} Drain-source voltage of a MOSFET

V_{GS} Gate-source voltage of a MOSFET

$V_{GS}(th)$ Threshold value of the gate-source voltage of a MOSFET

X_c x co-ordinate of the centre of the chip

Y_c y co-ordinate of the centre of the chip

List of Figures

1.1 Power Electronic system: a block diagram 22

1.2 Block diagram of a motor drive system 24

1.3 Typical power electronic system used for solar energy 26

1.4 Typical full-scale power electronic system used for wind energy 26

1.5 Typical power electronic system used for a hybrid electric vehicle 27

1.6 Block diagram of a bipolar HVDC system 28

1.7 (a) External view of a conventional power module (adapted from [6]), (b) Internal view of a conventional power module [7] 30

1.8 (a) Cross-section of the material-stack of a typical IGBT module placed on a heatsink, (b) Top view of the interior of a typical power module [10] 31

1.9 Discrete component (TO-220 packaging) (Replicated from [12]) 33

2.1 A basic circuit to demonstrate current switching characteristics of MOSFET 45

2.2 Turn-on ((a),(b),(c),(d) and (e)) and turn-off ((f),(g),(h),(i) and (j)) switching periods of the MOSFET 46

2.3 (a) Cross-section of a basic cell of a vertically diffused power MOSFET and the distribution of current (shown by the dotted region), (b) Top view of a typical power MOSFET chip 49
2.4 (a) Chip with uniform heat distribution (Case 1), (b) Chip with heat distribution in 20% of its volume (Case 2), (c) Chip with heat distribution in 20% of its volume around the centre (Case 3) (d) Position of the examination line AB on the top surface of the chip. 51
2.5 Temperature along AB for different heat distributions 52
2.6 An element of homogeneous isotropic material of volume dV . 55
2.7 Constant heat spreading angle 61
2.8 Cauer Network 64
2.9 Cauer Network for IGBT and diode package with heatsink . . 66
2.10 Foster Network 67

3.1 (a) Schematic of a single layer structure (b) Side view with heat flux 78
3.2 (a) Schematic of an N-layer structure (b) Side view of the structure with heat flux 91
3.3 Process to determine A_{1m} 99
3.4 Flowchart to determine the first N eigenvalues 109
3.5 Flowchart to determine the temperature at a point in time and space 115

3.6 An arbitrary waveshape with staircase approximation 117

4.1 Cross-section of the structure considered for the verification of the thermal models 119

4.2 Comparison between the model and simulation along the line Y = 22.282 (mm) 120

4.3 Comparison between the model and simulation along the line X = 20.152 (mm) 121

4.4 Comparison between the model and simulation along the line X = 20.152 (mm) 123

4.5 Comparison between the model and simulation along the line Y = 22.282 (mm) 124

4.6 (a) Top view of a commercial power module (courtesy of Microsemi Power Module Products), (b) Equivalent schematic view showing the devices (heat sources) and the lines AB, CD and EF. 125

4.7 (a) Three dimensional view of the PVU (presence of die), (b) Magnified view of the upper part of the structure. 128

4.8 (a) Three dimensional view of the PAU (No die, only solder), (b) Magnified view of the upper part of the structure. 129

4.9 (a) Three dimensional view of the CVU (presence of die), (b) Magnified view of the upper part of the structure. 129

4.10 (a) Three dimensional view of both the CAU (No die, only solder) and CAR, (b) Magnified view of the upper part of the structure. 130
4.11 (a) 3D view of the CAC, (b) Magnified view of the upper part of the structure. 130
4.12 (a) Side views of the lines AB and CD corresponding to COMSOL FEM (PVU) model, (b) Side views of lines AB and CD corresponding to the RNLF method, (c) Side view of line EF corresponding to COMSOL FEM (PVU) model, (d) Side view of line EF corresponding to the RNLF method. 131
4.13 Comparison of the simulation results for different structures along the line AB ($N_m = N_n = 200$ for CAC (RNLF)). 132
4.14 Temperature differences between different structures at the midpoint of line AB ($N_m = N_n = 200$ for CAC RNLF). 132
4.15 Temperature distribution in the middle of the second layer (Solder) of the rectangular N-layer structure 137
4.16 Temperature distribution in the middle of the second layer (Solder) of the rectangular N-layer structure 138
4.17 Temperature distribution in middle of the third layer (Copper) of the rectangular N-layer structure 138
4.18 Temperature distribution in middle of the fourth layer of the rectangular N-layer structure 139

4.19 Temperature distribution in middle of the fifth layer of the rectangular N-layer structure 139
4.20 Temperature distribution in middle of the fifth layer of the rectangular N-layer structure 140
4.21 Convergence of the temperature of the midpoint of MOSFET 3 at $t = 60$ ms 143
4.22 Comparison between the PVU and the CAC for point the midpoint of MOSFET 1 145
4.23 Comparison between the PVU and the CAC for point the midpoint of MOSFET 3 146

5.1 Experimental set-up showing the positioning of the IR camera and the power module. 151
5.2 Model in COMSOL Multiphysics showing the isothermal plane within the heat diffuser (note the low temperature difference across the plane). 152
5.3 (a) Schematic diagram of the circuit of the experiment (current path shown in bold), (b) Front view of the module with the matt black paint applied. 153
5.4 Pin diagram of the half-bridge power module 154
5.5 Thermal image in the region of interest captured by the IR camera showing lines AB, CD and EF. 156

5.6 Thermal distribution in the region of interest obtained by the model 157
5.7 Comparison between the experiment, RNLF method and COMSOL FEM (PVU) model along line CD. 158
5.8 Comparison between the experiment, RNLF method and COMSOL FEM (PVU) Model along line EF. 158
5.9 Experimental set-up showing the thermal camera and power module 161
5.10 Location of MOSFET dies M1-4 and points A, B and C on the power module 161
5.11 A series of frames showing the temperature on the surface of the module 162
5.12 Comparison between experimental, simulation and low-pass filtered simulation for point A in the subtransient region . . . 163
5.13 Comparison between experimental, simulation and low-pass filtered simulation for point A in the transient region 164
5.14 Comparison between the experiment and simulation for point C165

List of Tables

1.1 Relevant properties of typical insulating materials for substrates used in power module 37

1.2 Comparison of wide bandgap materials' properties versus Silicon 38

1.3 Coefficient of thermal expansion of different materials used in a typical power module 41

2.1 Analogy between electrical and thermal systems 64

4.1 Material assembly of the SiC power module 120

4.2 Comparison between the RNLF method and simulation 121

4.3 Material assembly and the relevant properties of the SiC power module (courtesy of Microsemi Power Module Products) . . . 126

4.4 Different structures for simulation 127

4.5 One dimensional and spreading thermal resistances of MOSFETs for the SiC power module 136

4.6 Comparison for different values of thickness of the patterned copper layer 141

4.7 Material properties for the SiC power module (part no. APTMC120AM20CT1NG, Courtesy of Microsemi Power Module Products) 144

5.1 Comparison between the experiment, COMSOL FEM (PVU) model and the RNLF method 159

Chapter 1

Introduction

The aim of this work is to develop thermal models of the standard power electronic module which may be useful for fast numerical design optimisation and provides physical insights when conduction plays a dominant role in the heat transfer process (within a power electronic module). To that end, basics of power modules and motivation of this work are presented in this chapter.

1.1 Introduction to Power Electronics

Power Electronics is the branch of Electrical and Electronic Engineering which deals with the processing of electrical power by solid-state electronic converters [1] known as power electronic converters. These converters may deal with the power ranging from tens of watts to several Gigawatts.

A power electronic system consists of a power input, a power processing

unit, load and a switching control unit; the schematic of which is shown in Figure 1.1. Power drawn from the input passes through the power processing unit and is supplied to the load. A feedback system monitors the output voltage or current and feeds the switching control unit. This unit produces gate/switching signal to maintain the output at the required level. Pulse Width Modulation (PWM) strategy may be used to control the power devices of the power processing unit. Power electronic converters can perform

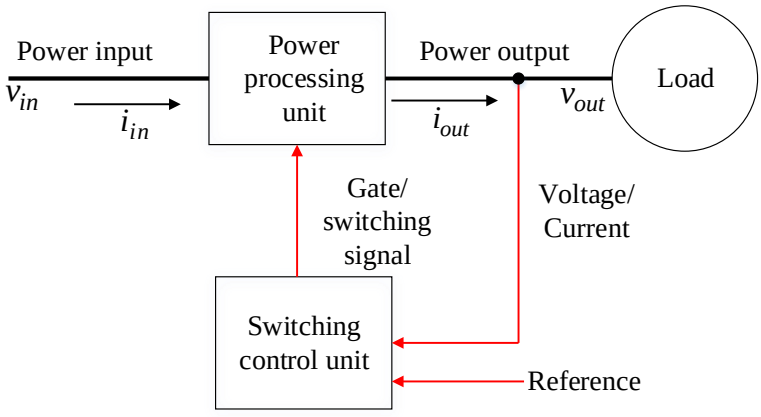


Figure 1.1: Power Electronic system: a block diagram

a number of operations or power conversions. For example, in a DC-DC converter, the DC input voltage is converted to a DC output voltage of a larger or smaller magnitude, sometimes with opposite polarity or with the isolation of the input and output ground references. In an AC-DC converter, an AC input voltage is rectified producing a DC output voltage. The DC output voltage and/or AC input current waveform can be controlled. DC-AC in-

version involves transforming a DC input voltage into an AC output voltage of controllable magnitude and frequency. AC-AC cycloconversion involves converting an AC input voltage to a given AC output voltage of controllable magnitude and frequency.

Power electronics systems consist of semiconductor devices and passive components; such as capacitor, inductor and resistor which are combined to accomplish the desired functionality of the power converter. Among these components, semiconductor devices are the electrical switches that control the flow of current (commutation) in the converter. These switches are of different types, such as - Bipolar Junction Transistors (BJTs), Metal Oxide Silicon Field Effect Transistors (MOSFETs), Insulated Gate Bipolar Transistors (IGBTs), diodes etc. which have different voltage and current rating and switching speeds.

1.2 Importance and applications of power electronics in the modern world

A significant portion of the world's power requirements are currently met by the electrical energy and it is expected to rise as many countries are prioritising the reduction of carbon emissions and shift to renewable energy sources. As the trend towards more electrification and using renewable energies increases, power electronic technologies are becoming ever more important. Some typical applications of power electronics are described below:

(a) Motor drives: A traditional application area of power electronics is variable speed drives for electrical motors as shown in Figure 1.2. Power

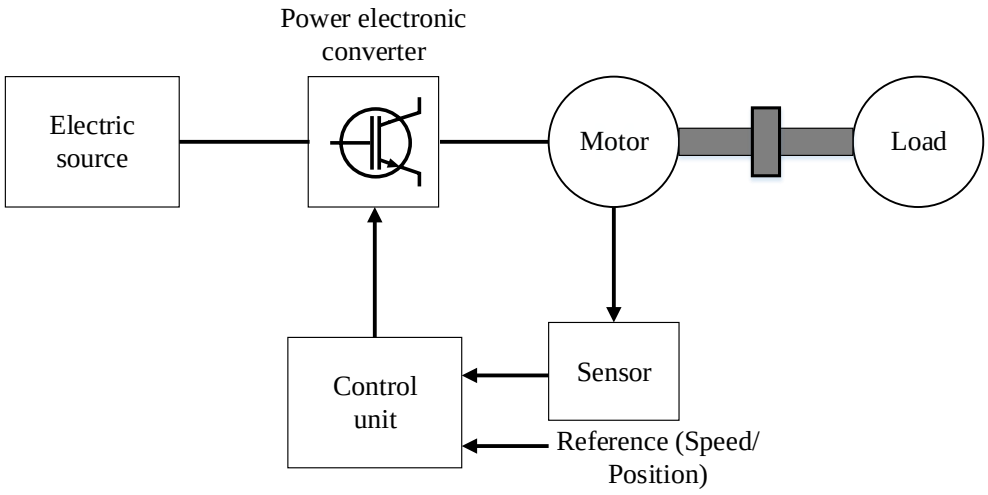


Figure 1.2: Block diagram of a motor drive system

electronic converters are able to vary the speed of motors making processes more efficient by reducing the consumption of energy. A common example is the motor driven air conditioning systems. Without power electronic converters, the motors of these systems would continually be running at the rated speed fixed by the supply frequency consuming vast amount of energy. Variable speed drives control the speed of motors depending on the load. These also control the process to ensure a consistent level of quality. Applied to HVAC systems, machinery in factories and on planes, trains and ships, the motors deliver precisely the right amount of power needed at any given time, conserving energy and also permitting trains and elevators to accelerate and

decelerate smoothly.

(b) Renewable energy generation: The production of renewable energy has increased rapidly over the past years. Consumption of energy produced from renewable sources such as wind, solar, tidal and hydro power for power generation grew by 16.3% of the overall energy consumption in 2013 [2]. This figure is increasing each year with the constructions of new onshore and offshore wind farms all over the world [3]. Currently, the renewable energy share of global electricity production is approximately 26.5% [4]. A study stated that renewable sources could meet the overall energy requirements of the world [5]. Power electronic technologies work as an interface between the renewable energy sources and conventional grid. For example, in the case of solar energy system, power electronic converters transform DC voltage produced by a solar panel into AC which is fed into a commercial electricity grid. Figure 1.3 shows the typical structure of a power electronic system for the solar energy. A similar conversion from DC to AC is needed for wind energy which must be fed into the grid at a constant frequency despite fluctuating wind conditions. Figure 1.4 shows typical structure of a full-scale power electronic system of a wind turbine. Wind power is converted by a permanent magnet synchronous generator into electrical power which can be of variable voltage and variable frequency. This AC power is usually converted then into a DC power using an AC/DC converter which is connected using a DC link to a DC/AC converter that allows interfacing the wind turbine with the

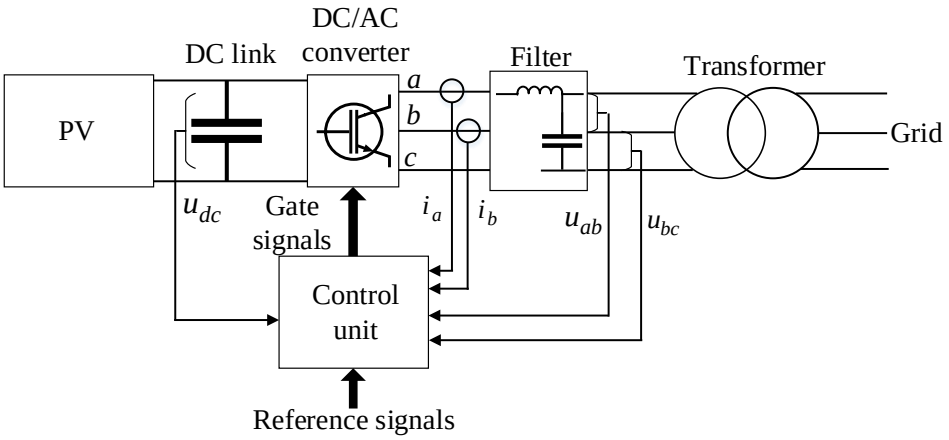


Figure 1.3: Typical power electronic system used for solar energy power grid.

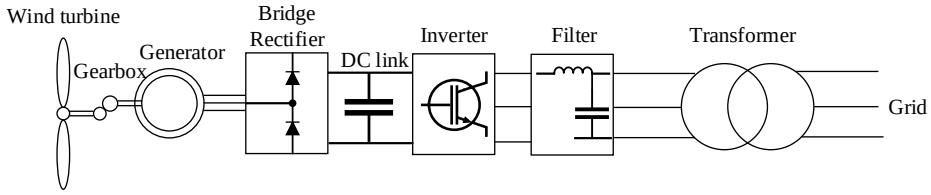


Figure 1.4: Typical full-scale power electronic system used for wind energy

(c) Electric vehicles: Electrification is opening up more applications for power electronics such as drive-trains for electric vehicles (EVs) as well as DC fast-charging stations which can charge the batteries of electric vehicles relatively quickly compared with the many hours it takes using standard residential charging ports. In the case of electric vehicles, power electronics can

be used to supply the braking energy back to the battery as needed. Figure 1.5 shows an example of a Plug-in Hybrid EV power electronic system. The energy is stored in a battery. A DC/DC converter boosts the voltage level in order to supply the DC link which distributes the energy to the inverter unit. The inverter drives the electric motor by converting the DC power into AC power with variable voltage/frequency which allows controlling the speed of the motor. The electrical system is assisted by an internal combustion engine which is used to drive an AC machine and charge the battery using the generator.

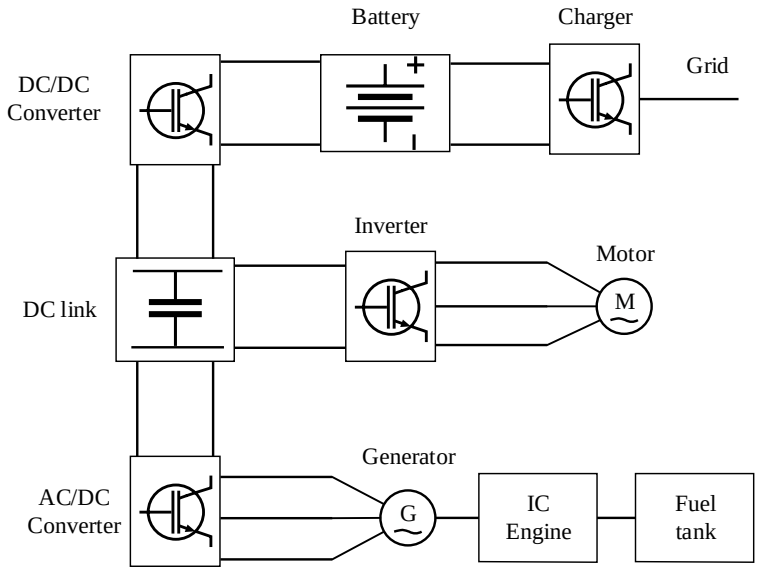


Figure 1.5: Typical power electronic system used for a hybrid electric vehicle

(e) High Voltage DC (HVDC) transmission system: As well as variable speed drives to control the speed of motors, power electronic technologies are used to transport electricity over huge distances with minimal losses. This is accomplished by power electronic converters which transform the AC voltage into a high DC voltage and vice-versa as shown in Figure 1.6.

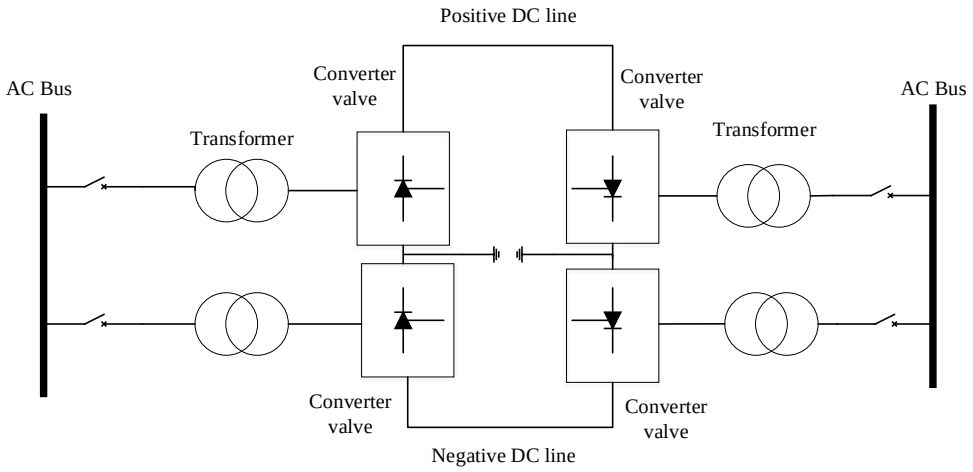


Figure 1.6: Block diagram of a bipolar HVDC system

Although power stations generate AC power and the power delivered to consumers is AC as well, HVDC is better for transmitting electricity over the long distance because an HVDC transmission line is much smaller and needs less corridor than AC lines for the same power capacity. It can be used to connect power from different systems, such as wind turbines and solar panels.

Apart from these applications, power electronics are used in data centres

and electronic consumer-products. However, discussion of these applications are omitted here because power modules are not typically much used in these applications.

1.3 Introduction to power modules

1.3.1 Definition and examples of power module

The power module is a building block which is used to provide placement, electrical connection and thermal management of several semiconductor devices (IGBT, MOSFET, diode etc.) in high-performance power electronic converters. It is a power circuit of different materials assembled together using various technologies, such as semiconductor die attachment, wire bonding, encapsulation, etc. It is typically used in high power applications, such as - motor drives, renewable energy systems, modern transmission system etc.

Power modules can come in multiple packages with different configurations, voltage and current ratings. Single switch, dual switch, chopper and half-bridge are some common configurations of power modules. External and internal views of a conventional IGBT module are given in Figure 1.7 (External view is adapted from [6] and internal view is replicated from [7]).

Research is going on in the academia and industry to improve the design of power module. One of the main objectives of this research is to develop three-dimensional packaging where gate drives, control circuits and passive

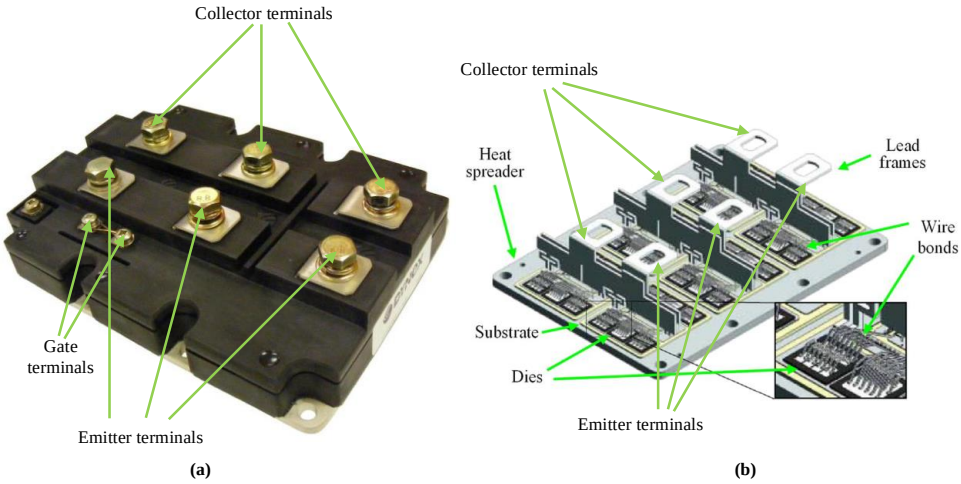


Figure 1.7: (a) External view of a conventional power module (adapted from [6]), (b) Internal view of a conventional power module [7]

components are integrated with the semiconductor devices [8]- [9]. However, detailed discussion of this advanced packaging is beyond the scope of this work and therefore, will not be elaborated further.

1.3.2 Structure of a typical power module

The structure of a typical IGBT power module is shown in Figure 1.8 (Top view of of the interior of a typical power module is replicated from [10]). Multiple IGBT/Diode chips are combined on a DBC (Direct-Bonded Copper) stack. The DBC substrate serves three purposes: providing thermal path for the semiconductor devices, providing electrical path and completing electrical layout and supporting the robust assembly of the module. One

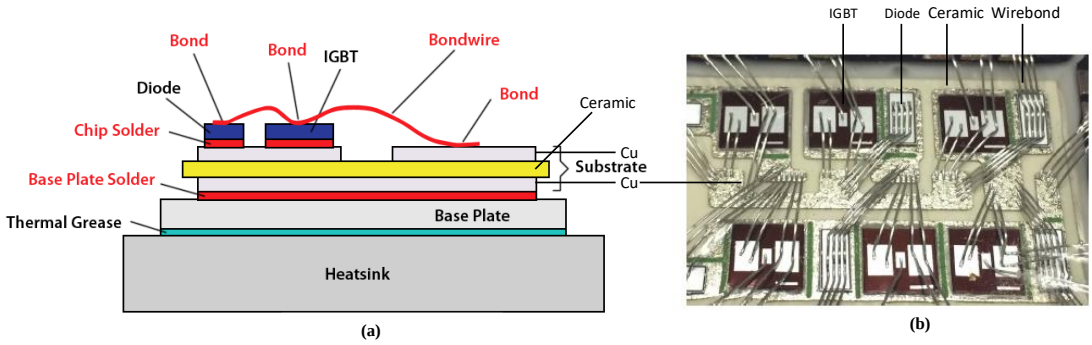


Figure 1.8: (a) Cross-section of the material-stack of a typical IGBT module placed on a heatsink, (b) Top view of the interior of a typical power module [10]

or more DBC stacks can be used within the package. It is usually made of ceramic with Copper layers attached to the upper and lower faces of that ceramic layer. Top copper layer is patterned because this layer is used for die-attachment and electrical connection. The bottom copper layer is uniform. Material of the ceramic layer can be Al_2O_3, AlN or Si_3N_4. A solder layer is typically used to attach the semiconductor device to the top copper layer of the DBC stack. It provides the electrical connection between the collector (in the case of IGBT)/drain (in the case of MOSFET) which constitutes the backside of the chip and the copper trace on the substrate. The DBC stack is attached to the baseplate using another solder layer providing mechanical attachment. The baseplate is normally made of Copper (Cu) or Aluminium or metal matrix composite (MMC), such as - Aluminium Silicon-Carbide (AlSiC) or Copper Molybdenum (CuMo). Bondwires made of Aluminium provide electrical connection between the chip surface and the

terminals. This assembly is ultimately encapsulated with silicone gel and a plastic casing for improved electrical isolation.

This stack of materials of a power module provides the path for heat flow. Power semiconductors dissipate heat during their normal operation which causes the temperature of the power modules to increase. This heat propagates through the multilayer structure from the chips towards the base-plate and the heatsink which removes the heat from the power module and release it to the surrounding environment. Sometimes, DBA (Direct Bonded Aluminium) stack is used in power modules. DBA stack consists of two sheets of thick aluminium sheets eutectic bonded to a ceramic substrate. Due to malleability of the Aluminium metal, DBA substrates have been reported to be more reliable in thermal cycling tests especially when conventional Aluminium wire bonds are used on the bare Aluminium [11].

1.3.3 Comparison between discrete devices and power module

Power semiconductor devices can be packaged as discrete components (shown in Figure 1.9 replicated from [12]).

Different types of discrete packaging are available, such as - TO-220, TO-247 etc. These discrete devices can withstand voltage typically up to 650 V while the continuous current conduction rating can be as high as 30 A. Although useful for relatively low power applications, discrete components

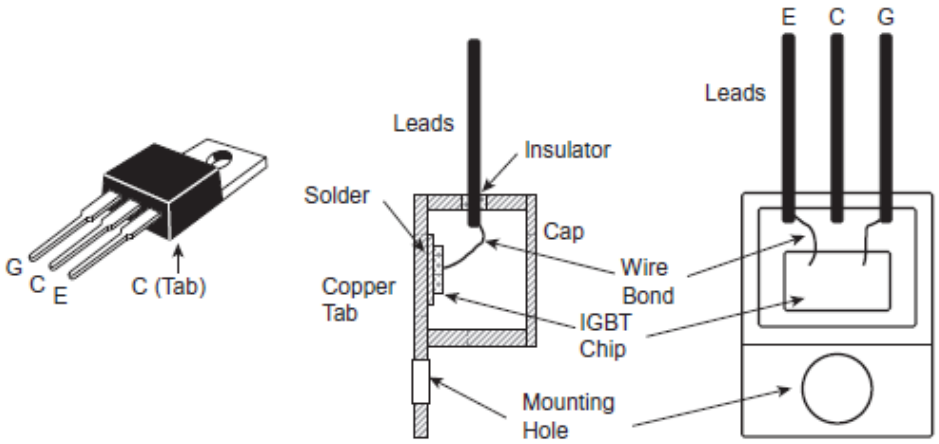


Figure 1.9: Discrete component (TO-220 packaging) (Replicated from [12])

are not typically used in high power applications because of its relatively high junction-to-case thermal resistance compared to that of a power module. For example, the junction-to-case thermal resistance of TO-220 packaged device ranges from 0.5 K/W to 4.0 K/W [13] and for TO-247 packaging, it ranges from 1.0 K/W to 2.5 K/W [14]. On the other hand, the junction-to-case thermal resistance per transistor of the commercial IGBT can be as low as 0.22 K/W [15] which allows the power modules to be used in high power applications.

Apart from the lower thermal resistances, another advantage of power module is it enables better thermal management due to its structure. For a discrete device, the metal plate for heat sink connection is typically non-isolated as shown in Figure 1.9, whereas in the power module, all semiconductor devices are thermally coupled to the baseplate but are electrically

isolated from it. Moreover, discrete devices are not always easy to mount to the heat sink. There is always the risk of inappropriate mounting (due to the lack of pressure or too much pressure, lack of thermal compound etc.) associated with the discrete devices. Power modules also offer better electrical insulation due to the rugged housings with large insulation and creepage distances. From this discussion, it is clear that power module is the most appropriate choice for high power applications.

1.3.4 Discussion on different materials and manufacturing technologies of power module

The reliability of a power module is dependent on its materials and manufacturing technologies. Therefore, it is worthwhile to discuss some important materials and manufacturing technologies of the power module as given below.

(a) Die-attach technologies: Common die attach technologies are based on soft solders with melting points below 250°C [16]. As long as the operation temperature of the semiconductor devices is limited to temperatures well below the melting point temperature of the used materials (For example, melting temperature is 183°C for Sn60Pb40 and 221°C for SnAg3.5 [17]), soft solders have been the materials of choice for a reliable chip-to-substrate interconnect in power electronics packaging. With the development of new generations of semiconductors (based on wide band gap materials like SiC

and GaN), the operating temperature will increase up to more than 200°C. This will lead to a significant decrease of the solder's strength and reliability (solder fatigue). Therefore, alternative technology is required to ensure the reliable operation of the power module. In this context, silver sintering is becoming an attractive alternative to soldering, especially for high temperature applications and high reliability. Sintering is the process of compacting and forming a solid mass of material by heat and/or pressure without melting it to the point of liquefaction. It is a combined surface, volume, and grain boundary diffusion process. In sintering process, a metal powder is mixed with organic materials (thinner, binder, dispersant) to form a paste. Silver is usually chosen as the metal, because of its excellent thermal and electrical performances. The thermal conductivity of Silver is 240 W/(mK) and melting temperature is 961°C [18]. Moreover, its price is reasonable and it can be sintered at low temperature (< 300°C) [18]. Furthermore, silver can be sintered in the presence of air. The silver paste is printed or dispensed on a substrate, exactly like a solder paste, and the die is placed on top of the paste. High pressure (several tens of MPa) and temperature (around 240°C) are then applied for the sintering to occur. It should be mentioned that the pressure applied during sintering requires specific tooling to avoid breaking the semiconductor dies. It is possible to use silver particles with a smaller size to reduce the need of pressure.

(b) Insulating material of the ceramic substrate: The insulating substrate must have following characteristics:

1) Serving as the supporting structure for the circuitry of the power module. It acts as the surface for depositing conductive, dielectric and resistive materials that form the passive circuit elements.

2) It should have high tensile and flexural strength to provide mechanical support for all active and passive chip components. It should be machinable and metallisable (compatible with metallization techniques; such as – Direct Bonded Copper (DBC) or Active Metal Brazing (AMB)).

3) Electrically, it must be able to isolate various conductive paths of the circuit.

4) It must have sufficient thermal conductivity to remove the heat generated by the components. It should have a coefficient of thermal expansion close with that of the power semiconductor chips for minimising thermal stress and providing high thermal stability.

5) It must have high resistance against various processing solvents and should be non-toxic.

Considering the above criteria, the substrate material can be Al_2O_3, AlN or Si_3N_4. Some important properties (from thermal point of view) of these materials are listed in Table 1.1. The data of this table is taken from [19–22].

Materials	Thermal conductivity (W/(mK))	Electrical resistivity (Ωcm)	Density (kg/m^3)	Specific heat capacity (J/(kgK)	CTE (ppm/°C)
Al_2O_3	30	$\approx 10^{14}$	3.95×10^3	775	≈ 6.00-7.00
AlN	180	$10^{11} \sim 10^{13}$	3.26×10^3	740	≈ 7.00
Si_3N_4	90	$\approx 10^{15}$	3.10×10^3	700	≈ 3.00

Table 1.1: Relevant properties of typical insulating materials for substrates used in power module

1.4 Wide bandgap semiconductor-based power module

Wide-bandgap semiconductors are semiconductor materials which have a relatively large bandgap between conduction band and valence band compared to that of typical semiconductors. Typical semiconductor, such as - Silicon has a bandgap in the range of 1 eV, whereas wide-bandgap materials have a bandgap in the range of 2 - 5 eV [23]. Wide bandgap semiconductors such as Gallium Nitride (GaN) and Silicon Carbide (SiC) require more energy to move electrons from valence bands to conduction band resulting in the enhancement of various properties as shown in Table 1.2 (Data of this table is taken from [24]). These devices offer exciting opportunities to improve the performance of power electronic systems in terms of improved efficiency, high voltage and higher temperature operation.

Major advantages of the SiC power devices are high voltage handling capability and high temperature operation of greater than 175°C. However, these advantages pose great challenges to the power module designer. For ex-

Properties	**Si**	**SiC**	**GaN**
Bandgap energy (eV)	1-1.5	3.26	3.45
Thermal conductivity (W/m/K)	160	390	220
Critical field strength (V/cm)	3.0×10^5	2.2×10^6	2.0×10^6
Maximum operating temperature (°C)	175	500	600

Table 1.2: Comparison of wide bandgap materials' properties versus Silicon

ample, high voltage operation of the power electronic module requires careful reduction of electric field intensification within the device as well as the module. Encapsulating materials with the desired dielectric breakdown strength as well as temperature performance must be applied on top of these devices to prevent premature voltage breakdown. For high temperature operations, proper die attach must be utilised because the melting temperature of the solder used in commercially available silicon IGBT power devices is around 200°C – 220°C [16, 18]. At high operation temperatures, polymeric materials utilized for electrical isolation inside the power modules break down more readily presenting a major reliability problem. Besides these, comparatively high parasitic inductance of conventional Si-based power module can induce high overshoot voltage during the fast turn-off operation of wide bandgap-based semiconductor device which might be higher than the breakdown voltage of the device. Wide bandgap semiconductor based module should be designed such a way that the parasitic inductance is reduced as much as possible. Therefore, simple drop-in replacement of Si devices in conventional power modules is not enough to manufacture wide bandgap semiconductor-

based power module.

1.5 Motivation

Power converters have the highest failure rate in electrical energy generating systems. Power converters are stated as the component with the highest failure rate in wind turbines in [25]. Similar observations are found in photovoltaic systems. In a study of a utility-scale photovoltaic plant in the US [26], it is noticed from maintenance data that the power inverter has recorded the highest failure rate and it was responsible of the highest number of unscheduled maintenance events which consequently contributed heavily to maintenance cost. Some recent studies focused on reliability quantification of power converters components by the examination of statistical samples [27–30]. It has been concluded in those studies that power module is one of the most fragile components in the power converter. Designing a power module is a challenging task because of a number of competing requirements. For example, mass and/or volumetric power density need to be maximised against electrical, thermal, mechanical and economic constraints during the design process. Due to the switching transients and on-state resistance, power devices in a power module dissipate heat during the operation of a power converter. Depending on the properties of different materials used in the power module, the devices experience temperature rise above ambient. Each power device in power has a maximum allowable junction temperature, violation

of which degrades its performance and damages it eventually. It also plays a critical role in monitoring the condition of a power device [31]. Besides these, maximum junction temperature essentially limits the power density of a power module. Thermal management of a power module is also strongly related with the maximum junction temperature which in turn affects the overall size and cost of the power electronic system. Therefore, accurate or reliable prediction of the steady-state junction temperature as well as the temperature-profile throughout a power module is an important part of the module design process from the perspective of design optimisation and power density.

In automotive, rail-traction and renewable energy applications the environmental and load-imposed thermal cycling or the combination of both can result in not only high peak junction temperature [32] but also large and frequent fluctuations in junction temperature [33] and temperature at the interfaces of different materials of a power module. This fluctuation causes stress at the interface of different materials due to the mismatch of CTE (shown in Table 1.3). The accurate estimation of the time-varying junction temperature is of interest in the real-time control, health management and active thermal management of power electronic converters [34, 35]. Methods to estimate the junction temperature profile are demonstrated in [36] and [37] for the implementation of real-time health management in applications with an uncertain load-profile. Additionally, it is often suggested that a continuous monitoring of junction temperature as a failure indicator is re-

Materials	**CTE (ppm/°C)**
Aluminium	22
Si	3
Solder	28
Cu	17
Ceramic	3-7

Table 1.3: Coefficient of thermal expansion of different materials used in a typical power module

quired to enable effective prognostics of semiconductor devices [38,39]. From the above discussion, it is clear that not only the steady-state value of the junction temperature but also the transient response of the semiconductor devices to varying heat loads is important when trying to predict or monitor system lifetime. Therefore, transient thermal modelling is an important addition to steady-state thermal modelling of the power module.

There are a number of ways thermal modelling can be done. These approaches or models are either too slow (Finite Element/Difference Method) or not flexible enough to take into account important physical phenomena (RC network based approach). As such, it is important to develop a model which is relatively fast with reasonable accuracy which may be used for design optimisation and provides physical insights and this is the primary motivation behind this work. It is worth mentioning that the acceptable accuracy may vary from sector to sector depending upon different constraints. For example, space-constraint is an important factor in automotive and aerospace application. Therefore, the error margin should be minimised as much as

possible in these applications.

1.6 Structure of the thesis

Chapter 2 lays the foundation of heat transfer analysis used subsequently in the following chapters. It also describes the available thermal modelling methods to estimate junction temperature in power modules.

Chapter 3 describes the detailed derivation of the steady-state thermal modelling and validation of the mathematical model by simulation. It also discusses some numerical issues associated with the computation.

Chapter 4 describes the detailed derivation of the transient thermal modelling and validation of the mathematical model by simulation.

Chapter 5 describes the experimental set-up and verification.

Chapter 6 concludes the thesis with some discussion on the applications and the limitations of the derived models.

1.7 Contribution of this work

This work has resulted in following journal papers published in IEEE Transactions on Power Electronics.

1. K. R. Choudhury and D. J. Rogers, "Steady-State Thermal Modeling of a Power Module: An N-Layer Fourier Approach," in *IEEE Transactions on Power Electronics*, vol. 34, no. 2, pp. 1500-1508, Feb. 2019.

(DOI: 10.1109/TPEL.2018.2828439)

2. K. R. Choudhury and D. J. Rogers, "Transient Thermal Modelling of a Power Module: An N-layer Fourier Approach," in *IEEE Transactions on Power Electronics*. (In-Print, DOI: 10.1109/TPEL.2020.2983248)

Chapter 2

Background

2.1 Introduction

This chapter presents a background about the origin and distribution of power loss in the devices, thermal modelling of power modules and methods to measure the junction temperature.

2.2 Origin of losses in hard-switched converters

In a hard-switched converter, a power semiconductor device is switched while there is an overlap between voltage and current of the device. This overlapping causes switching loss. Apart from that, voltage-drop across the device during the turn-on state causes conduction loss. These are explained with

the help of Figures 2.1 and 2.2.

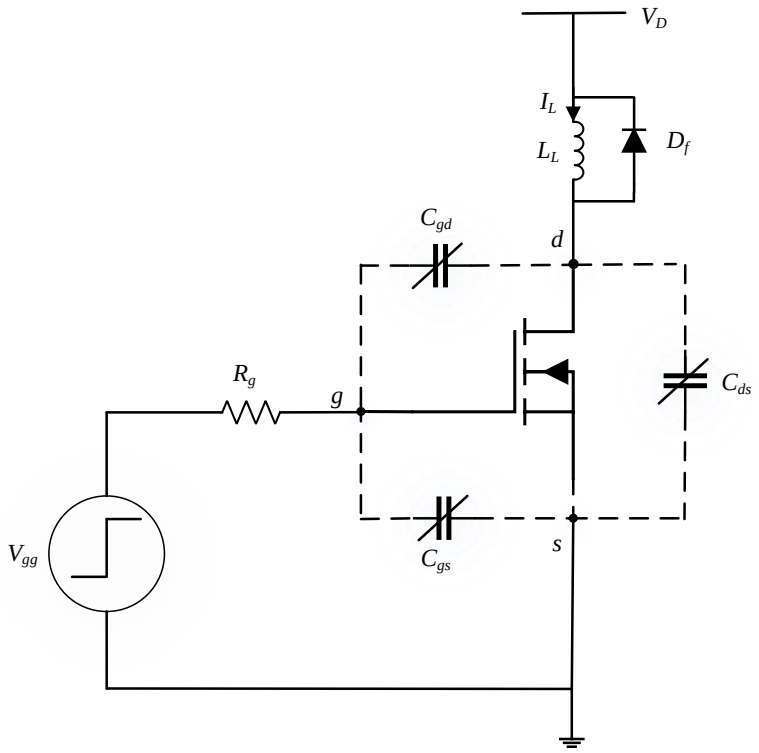


Figure 2.1: A basic circuit to demonstrate current switching characteristics of MOSFET

Figure 2.1 essentially shows a DC-DC buck converter which illustrates how device capacitances influence switching with an inductance L_L. The reason to choose this particular topology is it represents a basic building block of many power electronic converters, such as - three-phase or single-phase Voltage Source Converters (VSC). To be more precise, the combination of MOSFET and Diode in this circuit is called an 'N-cell' which is an important

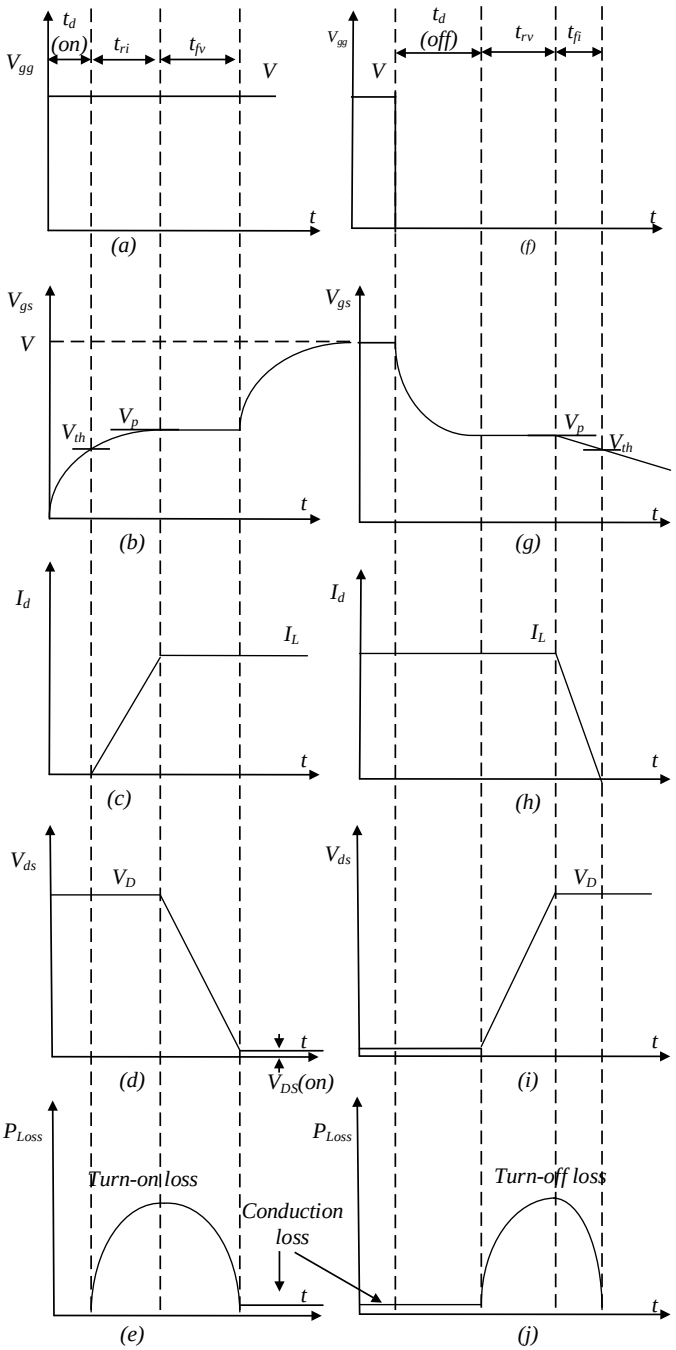


Figure 2.2: Turn-on ((*a*),(*b*),(*c*),(*d*) and (*e*)) and turn-off ((*f*),(*g*),(*h*),(*i*) and (*j*)) switching periods of the MOSFET

building block of H-bridge converters [40].

If L_L is high, the inductive load can be modelled as a constant current source. The gate of MOSFET is driven by an ideal voltage source whose output impedance is R_g. It is assumed that diode D_f is ideal.

The turn-on waveforms are shown in Figure 2.2. The gate drive voltage V_{gg} changes instantaneously at $t = 0$ from zero to V which is much higher than $V_{GS}(th)$ of the device. During turn-on delay time $t_d(on)$, gate-source voltage rises to $V_{GS}(th)$. Beyond this point, gate-source voltage continues to rise and drain current starts to increase. During the rise time t_{ri}, drain-source voltage is clamped at V_D because of the conducting diode. When I_d becomes equal to I_L, the gate-source voltage V_{gs} becomes clamped at V_p (Miller plateau) because the MOSFET is in active region. As a result, the gate current becomes constant which charges the Miller capacitance C_{dg} and forces the drain-source voltage to drop. Once the drain-source voltage has completed its drop to the on-state value V_{DS}, the gate-source voltage becomes unclamped and continues its rise to V_D. Beyond this point, conduction loss occurs as shown in Figure 2.2.

The turn-off of the MOSFET involves the inverse sequence of events that occurred during turn-on. The same basic analytical approach used to find the turn-on switching waveforms can be used to find the turn-off waveforms ((f),(g),(h),(i) and (j) in Figure 2.2).

Apart from the switching and conduction losses, there is an another type loss - off-state loss or leakage loss. Through a practical semiconductor device

in off-state, leakage current flows. However, the value of leakage current is very low for the voltages below the breakdown level.

2.3 Structure of a SiC power MOSFET

It is important to understand the structure of a SiC power MOSFET in order to appreciate the distribution of power loss within this device. A power MOSFET is typically of vertical structure where the top side of the device contains source and gate and the bottom side is for drain connection. The schematic diagram of a basic cell of a power MOSFET is shown in Figure 2.3 . As shown in this figure, P/P^+ wells are embedded in a lightly doped N^- region called drift region. It supports the space-charge region during the reverse bias condition. These P wells contain heavily-doped N^+ regions which act as source. Gate is made of polysilicon and insulated from gate by a layer of oxide material. It is important to highlight that a real device is made of thousands of cells. For example, power MOSFETs and IGBT chips have up to 50000 cells per mm^2 [41]. On the top of the chip, typically there are several source pads and one gate pad as shown in Figure 2.3. When gate-source voltage is greater than threshold voltage, an inversion channel is formed at the surface of the P-base region under the gate electrode. If the potential of drain is higher than that of source, electron flows from source to drain through channel and drift region. After being transported through the JFET region, the electrons enter the N^- drift region below junction J1. The

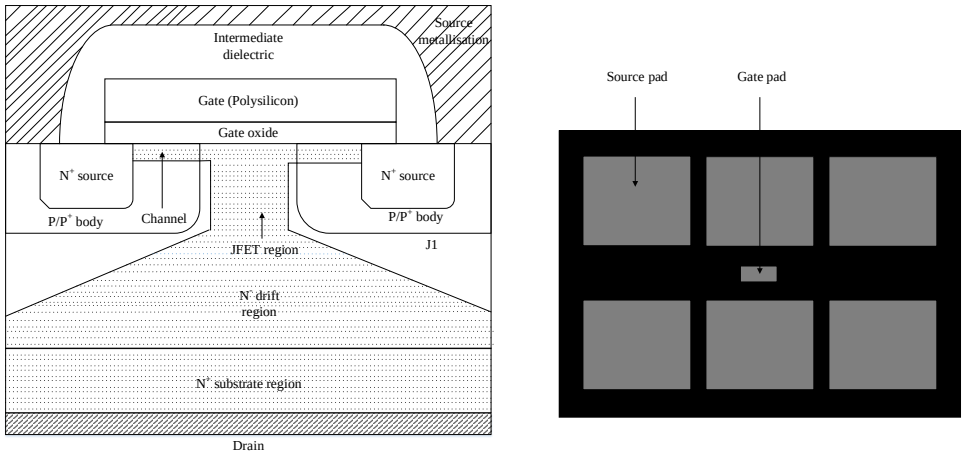


Figure 2.3: (a) Cross-section of a basic cell of a vertically diffused power MOSFET and the distribution of current (shown by the dotted region), (b) Top view of a typical power MOSFET chip

current spreads from the relatively narrow JFET region to the entire width of the cross-section of the cell. After that, the distribution and direction of current become uniform and perpendicular respectively. The resistance of each region of a power MOSFET is different due to the difference in doping density and current spreading of different regions.

From the above discussion, it is understood that heat is generated throughout the accumulation region, JFET region, majority of the drift region and substrate region. As the thermal conductivity of the material of semiconductor device is typically high (approximately 150 W/m/K for Si and 370 W/m/K for SiC), heat flux diffuses almost evenly throughout the device. Therefore, it is not unreasonable to assume uniform heat dissipation within

the device. Infact, it is a common practice to consider loss distribution in semiconductor devices as uniform.

2.4 The concept of junction temperature

The junction temperature basically means the temperature in the junction area of a power semiconductor device. This term became popular in the early days of semiconductor thermal analysis. By 'junction temperature', it is assumed that the die's temperature is almost uniform on its top surface. This is a reasonable assumption given the small volume and high thermal conductivity of the power semiconductor device. An example is given below to demonstrate this.

Let us assume that the thickness of a typical SiC MOSFET is 0.18 mm, cross-sectional area of the chip is 5.00×5.00 mm^2. This device is attached to a Copper baseplate (7.50 mm×7.50 mm×1 mm) by a solder layer of the thickness of 0.09 mm. Let us consider that this baseplate is attached to an ideal heatsink and the bottom of the baseplate is isothermal. The thermal conductivity of the solder material is 30 W/m/K. Figure 2.4 shows the cross-section of this arrangement for different heat distributions in the chip and the examination line AB on the top surface of the chip. AB goes through the middle of the surface and is parallel to the y axis. Let us assume that heat dissipation in the chip is 100 W. Figure 2.5 shows the temperature distribution along AB for different heat distributions within the chip. It

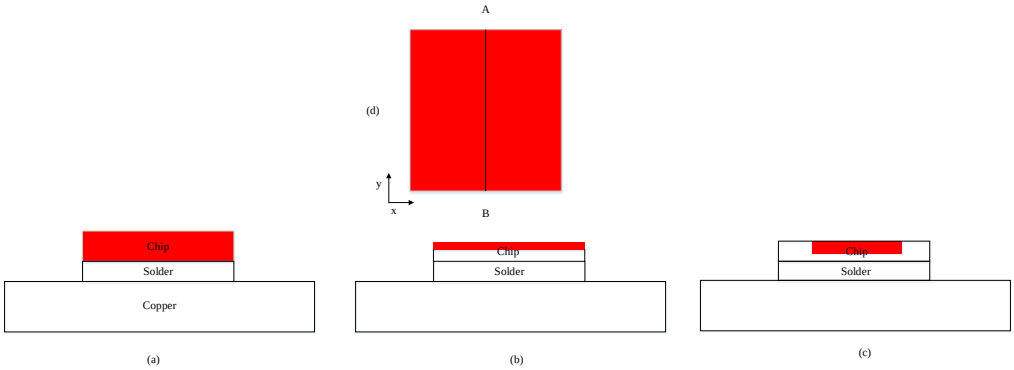


Figure 2.4: (a) Chip with uniform heat distribution (Case 1), (b) Chip with heat distribution in 20% of its volume (Case 2), (c) Chip with heat distribution in 20% of its volume around the centre (Case 3) (d) Position of the examination line AB on the top surface of the chip.

is observed that in cases 1 and 2, the maximum variation in temperature distribution is approximately 1.8°C. In case 3, the maximum variation is approximately 2°C. However, in the vicinity of the midpoint of the surface, the temperature is almost uniform (temperature difference is less than 0.5°C) for all cases. The maximum temperature of the surface in all cases are relatively close (the maximum temperature difference being approximately 1.5°C)

It is, however, important to highlight that considering junction temperature being uniform is a simplified approach because it ignores thermal spreading effect which can be large during high power conditions or in the presence of multiple heat sources.

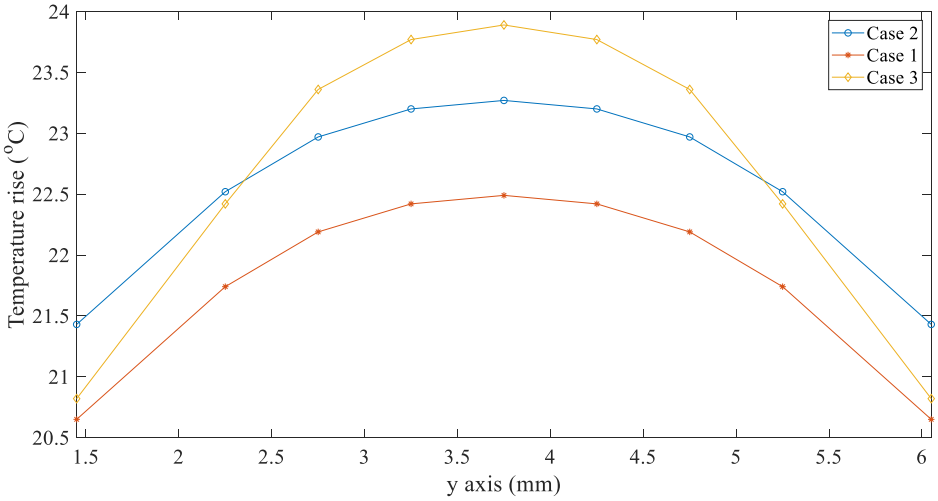


Figure 2.5: Temperature along AB for different heat distributions

2.5 Different modes of heat transfer and heat transfer in power modules

Heat transfer can take place by three different mechanisms: conduction, convection and radiation. Heat conduction is the transmission of heat energy in solid materials from high temperature to low temperature. This process is governed by Fourier's law of heat conduction. For a homogeneous and isotropic solid, Fourier's law is given below :

$$q(\hat{r}, t) = -k\nabla T(\hat{r}, t) \tag{2.1}$$

where the temperature gradient $\nabla T(\hat{r}, t)$ is a vector normal to the isothermal surface, $q(\hat{r}, t)$ is the heat flux vector representing heat flow per unit of time,

per unit area of the isothermal surface in the direction of the decreasing temperature gradient (that is why a minus sign is used in the equation) and k is the thermal conductivity. In the rectangular system, (2.1) can be written in the following form.

$$q(x, y, z, t) = -\hat{i}k\frac{\partial\, T}{\partial x} - \hat{j}k\frac{\partial\, T}{\partial y} - \hat{k}k\frac{\partial\, T}{\partial z} \tag{2.2}$$

where $\hat{i}$, $\hat{j}$ and $\hat{k}$ are the unit vectors in the direction of x, y and z respectively.

Convection is the heat transfer between solids and adjacent fluids (e.g. air, water, oil, ...). It has two forms: forced and natural. Forced convection happens when the fluid motion is induced by external sources (e.g. fan, pump, ...). Natural convection happens when no external factor is affecting the fluid motion. Convection is roughly governed by Newton's law of cooling. According to Newton's law,

$$q_{conv} = h(T - T_\infty) \tag{2.3}$$

where h is the convection heat transfer coefficient and T_∞ is the reference temperature of the surrounding fluid (gas or liquid). It should be noted that unlike Fourier's law, Newton's law is not so much a particular law as it is the definition of the heat transfer coefficient. In other words,

$$h = \frac{q_{conv}}{T - T_\infty} \tag{2.4}$$

It shows the dependency of h on the actual heat flux, and the difference between the surface temperature and a suitable reference temperature. Here h varies with the type of flow (laminar, turbulent or the mixture of both), the geometry of the body and flow passage area, the physical properties of the fluid, the average surface and fluid temperatures, and many other parameters. As a result, there is a wide difference in the range of values of the heat transfer coefficient for various applications.

Radiation is the heat transfer by electromagnetic field through vacuum and it is governed by Stefan-Boltzmann law of thermal radiation [42]. According to Stefan-Boltzmann law,

$$q_{rad} = \epsilon\sigma T^4 \tag{2.5}$$

where ϵ is the total, hemispherical emissivity (unitless) of the surface, σ is the Stefan-Boltzmann constant (5.67×10^{-8} W/(m^{2}K^4)) A commonly used approximation for the net radiation heat flux between a surface and a surrounding medium is given by (2.6).

$$q_{rad} = \epsilon\sigma(T^4 - T_\infty^4) \tag{2.6}$$

where T_∞ is the temperature of the surrounding medium with the assumption that ambient surroundings form an ideal enclosure. This is valid if the surroundings are isothermal and of a much larger surface area and the emitting surface is a gray body (i.e., surface emissivity and absorptivity is independent

of the wavelength).

It is common in the field of power electronics to assume that the heat transfer happens only by conduction inside the power module [43]. The main reason behind this assumption is that a typical power module is encapsulated with plastic and heat cannot escape through the sidewalls of the power module easily. It is only when the heat reaches the heatsink, heat is removed by convection. For example, if the flow rate of the coolant at the convective interface of the heatsink is constant, the heat transfer will only be affected by the solid conductive materials. Therefore, convection and radiation can be neglected when only the thermal stack of an power module is considered for modelling.

2.6 Equation of heat diffusion

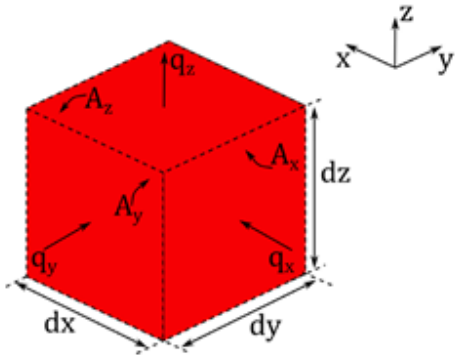


Figure 2.6: An element of homogeneous isotropic material of volume dV

Heat diffusion equation is a differential equation whose solution gives the

temperature distribution in a given medium over time. It can be derived from Fourier's law of heat conduction and the energy conservation principle [44]. For derivation, an infinitesimally small (differential) element of a homogeneous isotropic material of density ρ, thermal conductivity k and specific heat capacity c_p as shown in Figure 2.6 can be considered. The element volume is $dV = dxdydz$, its mass is $dm = \rho dV$ and the energy generation is g. The heat diffusion equation in a three-dimensional space is given as:

$$\frac{\partial}{\partial x}\left(k\frac{\partial T}{\partial x}\right) + \frac{\partial}{\partial y}\left(k\frac{\partial T}{\partial y}\right) + \frac{\partial}{\partial z}\left(k\frac{\partial T}{\partial z}\right) + g = \rho c_p \frac{\partial T}{\partial t} \tag{2.7}$$

The above equation states that at any point in the medium the rate of energy transfer by conduction into a unit volume plus the volumetric rate of thermal energy generation must be equal the rate of change of thermal energy stored within the volume. If thermal conductivity is constant, the heat equation is simplified as

$$\frac{\partial^2 T}{\partial x^2} + \frac{\partial^2 T}{\partial y^2} + \frac{\partial^2 T}{\partial z^2} + \frac{g}{k} = \frac{1}{\alpha}\frac{\partial T}{\partial t} \tag{2.8}$$

where α (m^2/s) is the thermal diffusivity of the medium. It is defined by the following equation.

$$\alpha = \frac{k}{\rho c_p} \tag{2.9}$$

Without any heat generation (2.8) reduces to

$$\frac{\partial^2 T}{\partial x^2} + \frac{\partial^2 T}{\partial y^2} + \frac{\partial^2 T}{\partial z^2} = \frac{1}{\alpha}\frac{\partial T}{\partial t} \tag{2.10}$$

2.7 Different approaches to the thermal modelling of semiconductor packages

Different approaches to the thermal modelling of semiconductor packages can be broadly classified into three categories: analytical and/or semi-analytical approaches, Finite Element Modelling (FEM) based or Finite Difference Method (FDM) based and RC thermal network. These approaches are briefly described below.

2.7.1 Analytical and semi-analytical approaches

In order to simplify the solution of the thermal problem the heat spreading may be neglected by assuming surfaces of constant temperature (isotherms) in the direction of heat conduction such that the temperature of a single point represents the temperature of the isotherm. This is a common assumption in order to simplify heat transfer problems in power electronics modules. Therefore, (2.10) is simplified into

$$\frac{\partial^2 T}{\partial x^2} = \frac{1}{\alpha}\frac{\partial T}{\partial t} \tag{2.11}$$

Some authors proposed solutions of the heat diffusion problem based on the above equation. As a matter of fact, analytical solutions for heat heat diffusion problem in electronics are being proposed since the introduction of power semiconductors in the 1950s. Mortenson [45] in 1957 showed analytically that the step response of the heat flow path of a transistor can be represented by an infinite summation of exponential terms. He assumed a one-dimensional rectangular heat flow path with a finite length and expressed the step response of the heat flow path by the following formula:

$$T_j(t) = T_a + QR_{th}\left(1 - \frac{8}{\pi}\sum_{n=1,3..}^{\infty}\frac{\exp(-t/\tau_n)}{n^2}\right) \tag{2.12}$$

where $T_j(t)$ is the junction temperature, T_a is the ambient temperature, Q is the power dissipation in transistor, R_{th} is the thermal resistance and τ_n is the thermal time-constant. Here, R_{th} and τ_n are given by the following equations.

$$R_{th} = \frac{L}{8.36kA} \tag{2.13}$$

$$\tau_n = \frac{n^2\pi^2\alpha}{4L^2} \tag{2.14}$$

where L, k, α and A are the length, thermal conductivity, thermal diffusivity and cross-sectional area of the transistor respectively. n is index number of the terms associated with each time constant.

Kennedy derived the formula of spreading resistance for a circular heat source situated on a finite cylinder [46]. Kokkas [47] has derived analytical solutions (both steady-state and transient) for a three-layer structure (containing multiple heat sources on top) situated on an isothermal surface. In doing so, he used Laplace's transformation. Ellison [48] derived an exact 3-D solution for the steady-state conduction for a single layer (the bottom of which is cooled by convection) with one rectangular source. A general solution of a steady-state temperature-rise due to an arbitrary number of heat sources situated on a rectangular single-layer structure and a double-layer structure is proposed in [49]. It is extended in [50] to include the effect of interfacial resistance in a rectangular double-layer structure with a very thin interfacial layer between them. Analytical solutions of the heat conduction equation have also been developed for systems with four layers using Green's functions in [51]. In [52], a general solution for the steady-state temperature-rise in multilayer rectangular domains with nonuniform internal heat generation is presented. It can consider the interface resistances between the layers. Interfacial defects, such as delamination or air voids, between the devices and the interconnect layers may be included in the model. Although applicable in many problems, such as – microelectronics, integration and packaging of computer chips, this technique requires manipulation of a large sparse matrix to determine the Fourier coefficients, which may be computationally very demanding depending upon the number of layers. Zommer [53] obtained an analytical transient solution for a two-layer and

three-layer structure under the semi-infinite approximation (the last layer being semi-infinite) of semiconductor packages by solving the heat conduction equation for all layers simultaneously with boundary conditions coupling adjacent layers. In that work, inverse Laplace transform is used for obtaining the final solution. In [54], the author proposed an analytical steady-state solution for a rectangular hybrid circuit. The model which is based upon the solution of three-dimensional Laplace‘s equation using Fourier techniques gives the temperature of each power dissipating element in the hybrid circuit. In obtaining the Fourier coefficients, matrix calculation is performed the size of which increases with the number of layers. In The analytical solutions discussed above, however, have found little applications in power electronics. For example, in [55], analytical thermal modelling for a central circular heat source situated on a cylindrical power module with three layers is presented. However, in practice, cylindrical power modules and circular semiconductor devices are not often seen (apart from high-power thyristor-type devices). Moreover, there are almost always more than three layers in practical power modules. In [56] and [57], Fourier-series-based techniques are used, but the presented method does not directly solve Laplace's equation for each layer; rather, the whole system is implemented as a chain of blocks in MATLAB/Simulink.

In [58] and [59], the spreading or variable angle model has been proposed. Spreading angle is defined as the angle at which heat is spread in a particular layer as demonstrated in Figure 2.7. It shows that a cross-section of a circular

power dissipating element of radius a on a substrate of thickness of w with a heat spreading angle α_{spread}. In a situation where the substrate extends to

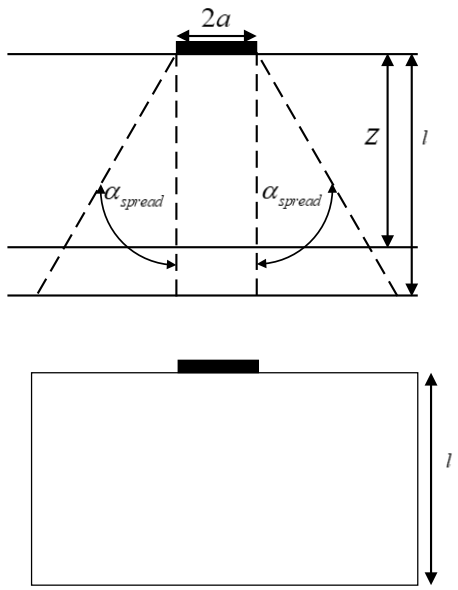


Figure 2.7: Constant heat spreading angle

infinity in the planar directions (x and y directions), the thermal resistance using the constant spreading angle is given by

$$R_{th} = \frac{1}{k}\int_0^l \frac{dl}{A} = \frac{l}{k\pi a(a + l\tan\alpha_{spread})} \tag{2.15}$$

2.7.2 Finite element-based or finite-difference based approaches

The finite-element method is a computational method that subdivides a CAD model or problem geometry into very small but finite-sized elements of geometrically simple shapes. The collection of all these simple-shapes constitutes the finite-element mesh. The next step is to take a system of field equations, mathematically represented by partial differential equations (PDEs) describing the physics of the problem and formulate these equations for each element. This is handled by approximating the fields within each element as a simple function, such as a linear or quadratic polynomial, with a finite number of degrees of freedom. This gives an approximate local description of the physics by a set of simple linear (but sometimes non-linear) equations. When the contributions from all elements are assembled you end up with a large sparse matrix equation system that can be solved by a sparse-matrix-solver. In [60] thermal and thermally induced response of a 3-D power modules packaged by a stacked plate structure was investigated using Finite Element Method.

The finite-difference method is the most direct approach to discretize partial differential equations. In this method, the problem geometry or the CAD model is divided into a grid of nodes. In each node in space, the continuum representation of the equations is replaced with a set of discrete equations called finite-difference equations. The finite difference method is typically defined on a regular grid and the accuracy of this method increases

with fineness of the grid. However, this method is not usually used for irregular geometries, but more often for rectangular or block-shaped models.

2.7.3 Thermal network-based approaches

(a) Cauer network equivalent: Fourier's law of heat conduction has an analogy with Ohm's law which governs the current conduction in a conductive material. This analogy allows transforming the heat conduction problem into an electrical network which can be solved using a circuit simulator such as SPICE. Therefore, it allows the incorporation of the thermal model of the semiconductor package within the electrical simulator so that electro-thermal simulation can be performed. Ohm's law can be expressed in the following form:

$$\vec{J} = -\sigma\left(\hat{i}\frac{\partial\ \vec{E}}{\partial x} + \hat{j}\frac{\partial\ \vec{E}}{\partial y} + \hat{k}\frac{\partial\ \vec{E}}{\partial z}\right) \tag{2.16}$$

where $\vec{J}$ is the current density (A/m^2), σ is the conductivity and $\vec{E}$ is the electric field (V/m). Similarity between Ohm's and Fourier laws encourages to compare between the differential equation in (2.16) and the differential equation that governs an electrical transmission line which can be expressed by the following differential equation with zero series inductance and zero shunt conductance:

$$\frac{\partial^2 u}{\partial x^2} = RC\frac{\partial u}{\partial t} \tag{2.17}$$

where $\frac{\partial u}{\partial x}$ is the voltage gradient in the x direction, C is the distributed capac-

Electrical parameters		**Thermal parameters**	
Current density	J (A/m^2)	Heat flux	q (W/m^2)
Current	I (A)	Power dissipation	P (W)
Resistance	R (Ω)	Resistance	R_{th} (K/W)
Voltage	V (V)	Temperature	T (K)
Capacitance	C (F)	Capacitance	C_{th} (J/K)

Table 2.1: Analogy between electrical and thermal systems

itance per meter (F/m), R is the distributed resistance per meter (Ω/m). The similarity between (2.17) and (2.11) suggests that the solutions of two differential equations are similar. This analogy was first stated by Newell [61] who represented the heat conduction path by a uniform electrical transmission line using basic RC circuits blocks. Therefore, the heat conduction path can be modelled by an electrical transmission line as shown in Figure 2.8. In this

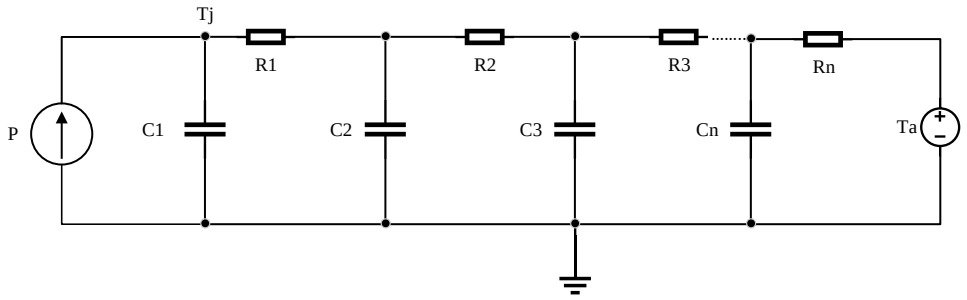


Figure 2.8: Cauer Network

electrical equivalent model, R_i and C_i represent thermal resistance and thermal capacitance of the heat conduction path. This model is called the Cauer network or the ladder network. The analogy between electrical and thermal terms is detailed in Table 2.1. Newell defined the thermal step response

equivalent to the transfer function of the transmission line which relates the input voltage (temperature) to the input current (power dissipation). This step response function (or thermal impedance function) describes temperature rise relative to a reference temperature. The Cauer network model has two advantages. It preserves the physical meaning of thermal resistance and thermal capacitances where the internal circuit nodes can theoretically be correlated to internal locations within the modelled heat conduction path. This is explained by the fact that a current pulse applied as an input to the Cauer network charges up the capacitors in sequence since they are all referenced to a common ground. This behaviour is in physical correlation with the heat diffusion phenomenon in solid structures where heat propagates from one isotherm to another in the direction of decreasing temperature. The other advantage is that the Cauer network allows the power semiconductor package and the heatsink to be modelled separately and then combined to obtain an extended thermal model which describes the thermal path from junction-to-ambient [62] as shown in Figure 2.9.

However, one major disadvantage of the Cauer network model is that the parameterization of the network is a difficult process and it suffers from inaccuracies due to the heat spreading effect. Cauer network parameterization can be done following the procedure presented by Newell, where the values of thermal resistances R_{th} and time constants τ_{th} of the thermal path layers can be determined from the material properties and geometrical information

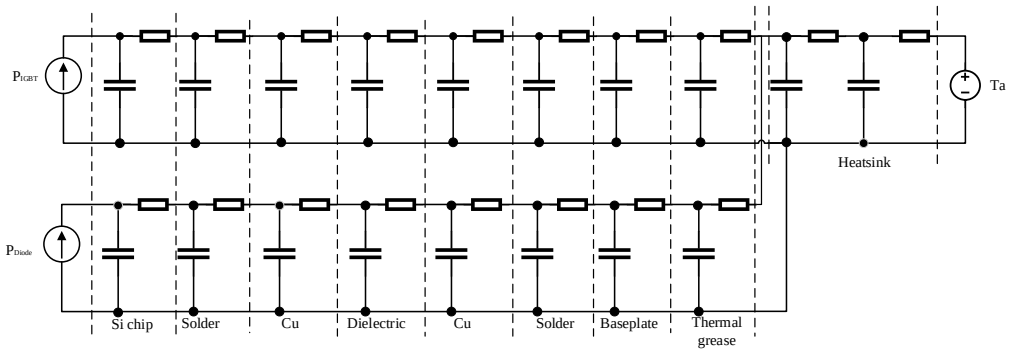


Figure 2.9: Cauer Network for IGBT and diode package with heatsink

of the structure:

$$\tau_{th} = \frac{\pi}{4}\frac{c_p \rho}{k} l^2 = \frac{\pi}{4} R_{th} C_{th} \tag{2.18}$$

$$R_{th} = \frac{1}{A}\left(\frac{\pi \tau_{th}}{4 k c_p \rho}\right)^{\frac{1}{2}} \tag{2.19}$$

where ρ (Kg/m^3) is the material density, c_p (Ws/(KgK)) is the specific heat capacity of material, k (W/(mK)) is the thermal conductivity, l (m) is the thickness of the layer and A (m^2) is the cross sectional area. (2.18) and (2.19) assume a rectangular structure and ignore the effect of heat spreading which reduces the accuracy of the resulting model for many geometries where heat spreading is significant.

Szekely [63] proposed a method which starts from the thermal impedance measurement to work out by deconvolution a "time-constant spectrum" which is principally the impulse response of the thermal diffusion path. The "time-constant spectrum" describes the time constants of the thermal path and

their corresponding thermal resistances. A Foster network (described in the next paragraph) is then obtained by discretizing the "time-constant spectrum" then circuit transformation techniques [64] are used to obtain the parameters of the Cauer network.

(b) Foster network equivalent: A behavioural model is an acceptable solution in cases where the interest is limited to the knowledge of the temperature at a specific location in the thermal path regardless of the internal temperature distribution along that path. This can be achieved by a black-

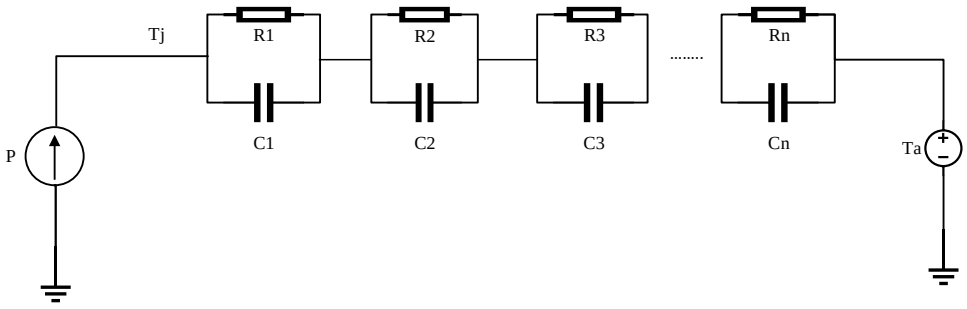


Figure 2.10: Foster Network

box model that describes the step response of the thermal conduction path. This type of model can be obtained from experimental measurement of thermal impedance and is commonly called a Foster network equivalent model.

Strickland [65] demonstrated the possibility of using a Foster network as an electrical equivalent to describe the thermal impedance of power semiconductor package.

Foster network shown in Figure 2.10 is a series connection of RC pairs. The step response of a Foster network can be described mathematically by a sum of exponential terms. The time step response (unit step response) of the electrical equivalent network shown in Figure 2.10 is expressed by:

$$T(t) = \sum_{i=1}^{n} R_i(1 - \exp(-t/\tau_i)) \tag{2.20}$$

where R_i and τ_i are the thermal resistance and time constant of the i^{th} term and n is the number of RC blocks.

Contrary to the Cauer network, the Foster network is considered a black-box model and has no physical correlation to the thermal diffusion path because all capacitors in Foster network start charging instantaneously in response to a power pulse applied at the input. This results in the development of voltages at the internal circuit nodes. Since voltage is analogous to temperature as described earlier, this means that the temperature of the internal nodes changes instantaneously in response to a power pulse. This disagrees with the physical process of heat diffusion. Therefore, Foster network is considered a behavioural model that can be used to describe the step response of a thermal conduction path at a specific location relative to a reference temperature. Hence, Foster network represents the thermal response of any thermal path regardless of its geometry. In addition to its physical insignificance, the Foster network model describes the "temperature rise" from a constant reference temperature (e.g. case temperature or ambient

temperature). Therefore, if the reference temperature is variable with time, the model becomes invalid or at least needs some modification. Moreover, a Foster network cannot be partitioned and combined as is the case with Cauer model. Instead, a characterization of the complete setup of the power semiconductor package including its heat sink must be done to generate a Foster model. An important advantage of the Foster model is the decoupled nature of its RC components which simplifies its numerical solution and allows computationally efficient thermal models to be obtained directly from experimental measurement of thermal impedance. This can be seen by the Laplace transformation of (2.20) which shows that the thermal impedance can be expressed by a partial fraction expansion:

$$Z_{th}(s) = \sum_{i=1}^{n} \frac{R_i}{sR_iC_i + 1} \tag{2.21}$$

2.8 Methods of measurement and estimation of junction temperature of power semiconductor devices in power modules

It is very important to measure or practically estimate the temperature of power semiconductor devices. One of the objectives of this measurement is to validate different thermal models.

(a) Integrated sensors: One way to obtain an online measurement of power semiconductor device temperature is via integrated sensors. Two types of sensors are typically integrated into power modules: negative temperature coefficient (NTC) resistors and on-chip diodes.

While NTC resistors are mounted on the DBC substrate and return the baseplate temperature with a time constant in the range of few seconds [66], on-chip diodes are integrated within the IGBT chip itself and return the local chip temperature with a time constant of about 1ms [67]. Both types require special consideration during the design of the package and manufacturing process to ensure electrical isolation from high voltage copper traces on the substrate and require separate copper traces and external pins which might increase manufacturing cost and give rise to new reliability issues.

Normally, NTC integrated sensors provide the temperature of the baseplate at the location it is mounted. A thermal RC network can then be used to calculate the junction temperature of the semiconductor chip [68]. However, integrated sensors give the local temperature at a specific location on the substrate. Therefore, they might not be affected by thermal degradation caused by solder fatigue at die-attach layer and substrate solder layer which can increase chip temperature. Consequently, depending on the location of the integrated sensor, an increment of temperature may not be seen by the NTC sensor.

(b) Temperature-sensitive electrical parameter (TSEP): TSEPs are parameters which characterize the electrical performance of power semiconductor devices, such as - on-state voltage V_{CE}(ON) (for IGBTs) or V_{DS} (for MOSFET), gate threshold voltage (V_{th}), gate resistance (R_G), turn-on and turn-off timing. These parameters show variations with chip temperature. Therefore, these allow the semiconductor chip itself to be used as a temperature sensor and can provide updated information about the real temperature of the power semiconductor chip. Therefore, they can provide up-to-date information about the real temperature of the power semiconductor chip. These serve as indirect methods of virtual junction temperature measurement. Not all possible TSEPs are appropriate for that purpose. Selection of TSEPs is based on several criteria discussed below [69]:

• Temperature sensitivity: TSEPs have different values of temperature sensitivity. A TSEP with greater temperature-sensitivity gives better measurement results.

• Measurement error: The influence of non-thermal effects during measurement is different for each TSEP. These introduce errors in measurement. Therefore, these non-thermal effects should be minimum. For example, the measured forward voltage drop of an IGBT or diode can be influenced by the resistance of the electrical connections. Since connection resistance varies with temperature, significant measurement errors can be created. Ageing can also adversely affect the temperature measurement.

• Linearity: The linear relation between TSEP and temperature is a de-

sired because it allows us to use less data points to measure the temperature.

• Repeatability: There should be no large scattering of TSEP values between different samples.

TSEPs have been used for thermal characterization of power modules for a long time. Electrical methods for junction temperature measurement have been used for many decades on transistors, particularly for offline thermal characterisation of devices. Forward voltage drop of IGBTs, diodes and some other devices has a linear correlation with chip temperature at low current which encouraged its use as a way to measure the thermal impedance of power modules. Other parameters such as threshold voltage V_{th} and on-resistance R_{ON} are used for the same purpose [70]. The use of TSEPs to measure junction temperature during the normal operation of power converters has been limited due to many difficulties. Some of these are discussed below.

• The lack of a flexible data acquisition platform that achieves the measurement on the power converter and sends it through the isolation barrier to the processing endpoint.

• The noisy working environment of power converters characterized by high voltage, high current, and electromagnetic fields makes an accurate online measurement of TSEPs a challenging task.

• Measurement inaccuracies can stem from the high common-mode noise, switching and modulation signals and the EMI of the working environment.

These factors can increase measurement errors and consequently affect the accuracy of the measured T_j [71]. Moreover, some TSEPs are affected

by the progressive degradation of power modules. For example, on-state voltage V_{CE}(ON) is affected by wire-bond lift-off. This can lead to large errors in the resolved T_j from V_{CE}(ON) when wire-bonds are lifted. Multiple studies have investigated TSEPs in details [35, 72]. Avenas et. al [34] investigated multiple electrical parameters for estimating junction temperature. He compared V_{CE}(ON) at high current, V_{CE}(ON) at low current, threshold voltage V_{th}, gate-emitter voltage V_{ge}, saturation current and switching times. He concluded that V_{CE}(ON) at low current is the most suitable TSEP due to its linearity and high sensitivity. Switching times and V_{CE}(ON) at high current have better online measurability at the expense of lower sensitivity. Kuhn [73] studied turn-on delay time, turn-off time and di/dt. He found that t_d(ON) and t_{off} are better in terms of linearity and current dependency than di/dt rendering them better candidates for online measurement of T_j. A linear correlation of the TSEP with temperature is desirable as it means a constant sensitivity to temperature and makes translating the TSEP measurement into T_j easier. On the other hand, a non-linear relationship to temperature can result in a variable sensitivity of the TSEP to temperature where the sensitivity can be lower for some operating points compared to others.

(c) Temperature measurement by InfraRed (IR) camera: A direct measurement method that works independently of the operating condition of the power converter is clearly desirable. Infrared (IR) temperature measure-

ment fulfils this requirement. It provides a strict separation of the converter and the measurement system with high speed and precision. The use of an IR camera provides a temperature map of the surface of the power module. An IR camera is a device based on infrared thermography that forms an image using infraRed radiation, similar to a common camera that forms an image using visible light. It detects infrared energy (heat) and converts it into an electronic signal, which is then processed to produce a thermal image on a video monitor and perform temperature calculations. Infrared thermography technique is a non-contact and non-destructive test method which uses infrared imaging to detect, display and record thermal patterns and temperature across the surface of an object.

Emissivity is a very important aspect of infrared thermography. It is defined as the ratio of the thermal radiation from a surface to the radiation from an ideal black surface at the same temperature as given by the Stefan–Boltzmann law. As no object can emit more thermal radiation than a perfect black surface, therefore emissivity of an object cannot be greater than 1. It is important to highlight that if an infrared camera is used to measure the surface temperature of a shiny object, black paint should be used on the surface to increase the emissivity close to 1. This technique is used in this work which is explained in chapter 5.

(d) Temperature measurement by fibre optic sensors: Fibre optic sensor can be used for the measurement of temperature. Now-a-days opti-

cal probes are widely used for temperature measurement. They have fast response times and are very accurate. Moreover, temperature measurement by these do not necessitate to carry any electrical signals and are not influenced by electromagnetic and radio frequency interferences. Therefore, fibre optic temperature sensor technologies for direct hotspot temperature measurements have matured and become generally accepted by transformer users and manufacturers during the last three decades or so [74]. However, to the knowledge of the author, this technique is still not used widely for power modules.

Fundamentally, an optical source coupled to a fibre optic transmission line constitutes the fibre optic sensors. This source directs the radiation towards the head of a sensor [75]. An optical fibre sensor comprises the following elements: an optical fibre, a sensing component, a detector, and a light source. It operates in such a way that some parameters of the optical system (wavelength, phase, polarization, intensity, etc.) are modulated by the sensing element, which produces a change in the characteristics of the optical signal at the detector. The main idea is to measure an external physical parameter by inducing changes in one or more of the optical properties of the light beam travelling inside the optical fibre.

Chapter 3

Steady-state and transient thermal modelling of a rectangular N-layer structure

3.1 Mathematical background

Throughout this work, the following mathematical methods and techniques are used to obtain the solutions for the temperature distribution of the different models under study. At first, these methods are described before deriving the detailed thermal models.

3.1.1 Separation of variables

Separation of variables is a widely used method to solve linear partial differential equations (PDEs) including the heat equation, wave equation and the Helmholtz equation. The main idea of the method of separation of variables is to seek solutions to a PDE represented in the form of product of functions, each of which depends on one variable [76], in which the PDE is separated into ordinary differential equations (ODEs) that can be solved individually. Thereafter, solutions of those ODEs are used to find the solution of original PDE [77]. However, the direct application of this method has some requirements on the PDE and the boundary conditions of the system under study. Such requirements are [78]: 1) Linear and homogenous PDE;

2) Linear boundary conditions;

3) For steady-stare problems, all the boundary conditions are homogenous with the exception of a single non-homogeneous boundary condition.

4) For transient problems, all the boundary conditions are homogeneous and the initial condition is non-homogeneous.

If the above requirements are not satisfied, other approaches have to be applied first before using separation of variables, such as the principle of superposition, shifting, splitting the problem, using mathematical transformations or other relevant techniques.

3.1.2 Application of the separation of variables method for the steady-state case

The application of the separation of variables method to a linear PDE defined in an orthogonal coordinate system (like, Cartesian, cylindrical, and spherical coordinate systems) can be applied by expressing the dependent variable of the PDE in a separable form of the orthogonal coordinates. To illustrate this application, let us consider a three-dimensional single layer homogeneous rectangular structure with no internal heat generation as illustrated in Figure 3.1. The bottom surface is isothermal, on the top surface there is a heat

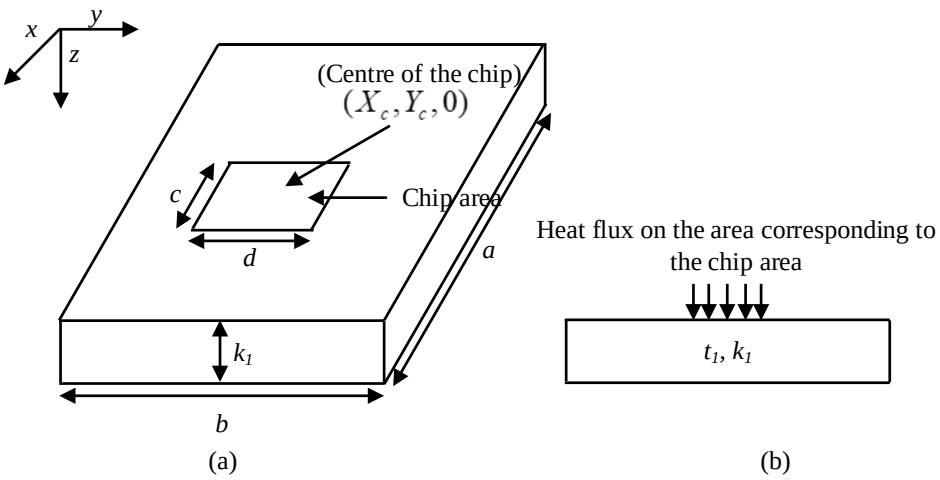


Figure 3.1: (a) Schematic of a single layer structure (b) Side view with heat flux

source of constant flux. The position of the source is given by its centre (X_c , Y_c , 0) and its length and width are c and d, respectively. This source

generates heat Q uniformly over the surface is situated. Except the area corresponding to heat flux, the top surface is adiabatic. All the sides are adiabatic as well. The mathematical formulation of the steady-state problem is given by following equation.

$$\frac{\partial^2\theta}{\partial x^2} + \frac{\partial^2\theta}{\partial y^2} + \frac{\partial^2\theta}{\partial z^2} = 0 \tag{3.1}$$

The system is subject to the following boundary conditions.

$$\text{BC1:} \quad \theta\Big|_{z=t_1} = 0 \tag{3.2}$$

$$\text{BC2:} \quad \frac{\partial\theta}{\partial x}\Big|_{x=0,a} = 0 \tag{3.3}$$

$$\text{BC3:} \quad \frac{\partial\theta}{\partial y}\Big|_{y=0,b} = 0 \tag{3.4}$$

For the area corresponding to the heat source,

$$\text{BC4:} \quad k_1\frac{\partial\theta}{\partial z}\Big|_{z=0} = -\frac{Q}{cd} \tag{3.5}$$

For the area outside the heat source,

$$\text{BC5:} \quad \frac{\partial\theta}{\partial z}\Big|_{z=0} = 0 \tag{3.6}$$

The problem formulation contains four homogenous boundary conditions and a single non-homogeneity at BC4; hence separation of variables is appropriate. We assume the separation of the form

$$\theta(x, y, z) = X(x)Y(y)Z(z) \tag{3.7}$$

Substituting (3.7) in (3.1 and dividing the both sides by the product of the variables, we get

$$\frac{1}{X}\frac{\partial^2 X}{\partial x^2} + \frac{1}{Y}\frac{\partial^2 Y}{\partial y^2} + \frac{1}{Z}\frac{\partial^2 Z}{\partial z^2} = 0 \tag{3.8}$$

We have two homogenous dimensions for this problem, so we elect to separate the homogeneous x dimension first:

$$\frac{1}{Y}\frac{\partial^2 Y}{\partial y^2} + \frac{1}{Z}\frac{\partial^2 Z}{\partial z^2} = -\frac{1}{X}\frac{\partial^2 X}{\partial x^2} = \lambda_m^2 \tag{3.9}$$

where λ^2 is the first separation constant, selected to yield a boundary value problem in the x dimension, as formulated here

$$\frac{\partial^2 X}{\partial x^2} + \lambda_m^2 X = 0 \tag{3.10}$$

which is subject to BC2. Solution of (3.10) yields

$$X = C_1 \cos(\lambda_m x) + C_2 \sin(\lambda_m x) \tag{3.11}$$

Due to the separation of variables, BC2 implies

$$\left.\frac{\partial X}{\partial x}\right|_{x=0,a} = 0 \tag{3.12}$$

For x = 0,

$$C_2 \lambda_m = 0 \tag{3.13}$$

Or

$$C_2 = 0 \tag{3.14}$$

For x = a,

$$C_1 \sin(\lambda_m x) = 0 \tag{3.15}$$

As C_1 cannot be zero, it implies

$$\sin(\lambda a) = 0 \tag{3.16}$$

Therefore,

$$\lambda_m a = m\pi \tag{3.17}$$

where m = 0, 1, 2, 3,... Now,

$$X = C_1 \cos(\lambda_m x) \tag{3.18}$$

We now separate the remaining homogeneous y dimension by setting:

$$\frac{1}{Z}\frac{\partial^2 Z}{\partial z^2} + \frac{1}{X}\frac{\partial^2 X}{\partial x^2} = -\frac{1}{Y}\frac{\partial^2 Y}{\partial y^2} = \delta_n^2 \tag{3.19}$$

As

$$\frac{1}{X}\frac{\partial^2 X}{\partial x^2} = -\lambda_m^2, \tag{3.20}$$

it implies that

$$\frac{1}{Z}\frac{\partial^2 Z}{\partial z^2} - \lambda_m^2 = -\frac{1}{Y}\frac{\partial^2 Y}{\partial y^2} = \delta_n^2 \tag{3.21}$$

where δ_n^2 is the second separation constant, selected to yield a boundary value problem in the y dimension, as formulated here:

$$\frac{\partial^2 Y}{\partial y^2} + \delta_n^2 Y = 0 \tag{3.22}$$

Therefore,

$$Y = C_3 \cos(\delta_n y) \tag{3.23}$$

where

$$\delta_n = \frac{n\pi}{b} \tag{3.24}$$

where $n = 0, 1, 2, 3,...$

Finally, we consider the non-homogenous z dimension as given by

$$\frac{\partial^2 Z}{\partial z^2} - (\lambda_m^2 + \delta_n^2) Z = 0 \tag{3.25}$$

which is subject to BC4. Because the eigenvalues λ_m and δ_n are defined, it is convenient to introduce the parameter β_{mn}

$$\beta_{mn}^2 = \lambda_m^2 + \delta_n^2 \tag{3.26}$$

For $m = 0$ and $n = 0$, $\beta_{mn} = 0$ which reduces (3.25) to

$$\frac{\partial^2 Z}{\partial z^2} = 0 \tag{3.27}$$

Or,

$$Z = A + Bz \tag{3.28}$$

which is also a solution of (3.1). Apart from the solution corresponding to $m = 0$ and $n = 0$, equation (3.25) yields

$$Z = C_5 \exp^{\beta_{mn} z} + C_6 \exp^{-\beta_{mn} z} \tag{3.29}$$

It is not difficult to show that (3.29) can be written as

$$Z = C_7 \cosh \beta_{mn} z + C_8 \sinh \beta_{mn} z \tag{3.30}$$

Therefore, the most general solution is now constructed by a summation of

all solutions

$$\theta(x,y,z) = A+Bz+\underbrace{\sum_{m=0}^{\infty}\sum_{n=0}^{\infty} C_1C_3\cos(\lambda_m x)\cos(\delta_n y)(C_7\cosh\beta_{mn}z + C_8\sinh\beta_{mn}z)}_{\text{both } m \text{ and } n \text{ cannot be 0 at the same time}} \tag{3.31}$$

Or,

$$\theta(x,y,z) = A + Bz + \underbrace{\sum_{m=0}^{\infty}\sum_{n=0}^{\infty} \cos(\lambda_m x)\cos(\delta_n y)(C\cosh\beta_{mn}z + D\sinh\beta_{mn}z)}_{\text{both } m \text{ and } n \text{ cannot be 0 at the same time}} \tag{3.32}$$

where $C = C_1C_3C_7$ and $D = C_1C_3C_8$

Now, (3.32) can be written as

$$\begin{aligned}\theta(x,y,z) &= A + Bz + \sum_{m=1}^{\infty}\cos(\lambda_m x)[A_m\cosh(\lambda_m z) + B_m\sinh(\lambda_m z)] \\ &+ \sum_{n=1}^{\infty}\cos(\delta_n y)[A_n\cosh(\delta_n z) + B_n\sinh(\delta_n z)] \\ &+ \sum_{m=1}^{\infty}\sum_{n=1}^{\infty}\cos(\lambda_m x)\cos(\delta_n y)[A_{mn}\cosh(\beta_{mn}z) + B_{mn}\sinh(\beta_{mn}z)]\end{aligned} \tag{3.33}$$

where A, B, A_m, B_m, A_n, B_n, A_{mn} and B_{mn} are Fourier coefficients which can be obtained by using orthogonality relations and boundary conditions. The detailed process will be explained later.

3.1.3 Application of the separation of variables for the transient case

The mathematical formulation of the problem is given as

$$\frac{\partial^2\theta}{\partial x^2} + \frac{\partial^2\theta}{\partial y^2} + \frac{\partial^2\theta}{\partial z^2} = \frac{1}{\alpha}\frac{\partial\theta}{\partial t} \tag{3.34}$$

At $t = 0$, the initial condition is

$$\text{IC: } \theta = 0 \tag{3.35}$$

The heat flux is a step input such that it changes instantaneously from zero for $t < 0$ to q_0 for $t \geq 0$. Therefore, θ can be written as a sum of the steady-state solution (θ_s) and the transient solution (θ_t):

$$\theta = \theta_s + \theta_t. \tag{3.36}$$

Now, θ_s is subject to the following boundary conditions. Underneath the heat source,

$$\left.\frac{\partial\theta_s}{\partial z}\right|_{z=0} = -\frac{q_0}{k_1} = -\frac{Q}{k_1 cd} \tag{3.37}$$

Outside the source, the boundary condition is

$$\left.\frac{\partial\theta_s}{\partial z}\right|_{z=0} = 0. \tag{3.38}$$

Because of the adiabatic sides of the structure,

$$\left.\frac{\partial \theta_s}{\partial x}\right|_{x=0,a} = 0 \tag{3.39}$$

$$\left.\frac{\partial \theta_s}{\partial y}\right|_{y=0,b} = 0 \tag{3.40}$$

Therefore, the solution of θ_s is given by (3.33). θ_t is subject to the following boundary conditions.

$$\left.\frac{\partial \theta_t}{\partial z}\right|_{z=0} = 0 \tag{3.41}$$

$$\left.\theta_t\right|_{z=t_1} = 0 \tag{3.42}$$

$$\left.\frac{\partial \theta_t}{\partial x}\right|_{x=0,a} = 0 \tag{3.43}$$

$$\left.\frac{\partial \theta_t}{\partial y}\right|_{y=0,b} = 0 \tag{3.44}$$

The initial condition is

$$\theta_t = -\theta_s \tag{3.45}$$

θ_t can be found by solving the following equation

$$\frac{\partial^2 \theta_t}{\partial x^2} + \frac{\partial^2 \theta_t}{\partial y^2} + \frac{\partial^2 \theta_t}{\partial z^2} = \frac{1}{\alpha}\frac{\partial \theta_t}{\partial t} \tag{3.46}$$

The problem formulation contains all homogenous boundary conditions and a single non-homogeneous initial condition. Therefore, (3.46) can be solved by the separation of variable method. Let's consider

$$\theta_t = X(x)Y(y)Z(z)T(t) \tag{3.47}$$

Substituting equation (3.47) into the PDE of equation (3.46) and rearranging yields

$$\alpha\frac{1}{X}\frac{\partial^2 X}{\partial x^2} + \alpha\frac{1}{Y}\frac{\partial^2 Y}{\partial y^2} + \alpha\frac{1}{Z}\frac{\partial^2 Z}{\partial z^2} = \frac{1}{T}\frac{\partial T}{\partial t} = -\zeta^2 \tag{3.48}$$

We consider first the time-dependent equation:

$$\frac{\partial T}{\partial t} + \zeta^2 T = 0 \tag{3.49}$$

which yields the expected decaying exponential solution

$$T(t) = C_1 \exp(-\zeta^2 t) \tag{3.50}$$

where ζ will be determined by the homogeneous spatial dimensions. We now consider the spatial variables of equation (3.48), rearranging as

$$\frac{1}{Y}\frac{\partial^2 Y}{\partial y^2} + \frac{1}{Z}\frac{\partial^2 Z}{\partial z^2} + \zeta^2/\alpha = -\frac{1}{X}\frac{\partial^2 X}{\partial x^2} = \beta^2/\alpha \tag{3.51}$$

Separating the x dimension as our first boundary value problem and using

the relevant boundary conditions yield

$$X(x) = C_2 \cos(\frac{\beta x}{\sqrt{\alpha}}) \tag{3.52}$$

where

$$\frac{\beta}{\sqrt{\alpha}} = \frac{m\pi}{a} \tag{3.53}$$

We now rearrange equation (3-110) to separate the next homogeneous dimension:

$$\frac{1}{Z}\frac{\partial^2 Z}{\partial z^2} + \zeta^2/\alpha - \beta^2/\alpha = -\frac{1}{Y}\frac{\partial^2 Y}{\partial y^2} = \eta^2/\alpha \tag{3.54}$$

Having forced the y dimension as the next boundary value problem and using the relevant boundary conditions yields

$$Y(y) = C_3 \cos(\frac{\eta y}{\sqrt{\alpha}}) \tag{3.55}$$

where

$$\frac{\beta}{\sqrt{\alpha}} = \frac{n\pi}{b} \tag{3.56}$$

We now consider the last homogeneous dimension from equation (3.54)

$$\frac{1}{Z}\frac{\partial^2 Z}{\partial z^2} + \zeta^2/\alpha - \beta^2/\alpha - \eta^2/\alpha = 0 \tag{3.57}$$

Letting $\nu^2/\alpha = \zeta^2/\alpha - \beta^2/\alpha - \eta^2/\alpha$ yield the final boundary value problem,

giving

$$Z(z) = C_5 \sin(\frac{\nu z}{\sqrt{\alpha}}) + C_6 \cos(\frac{\nu z}{\sqrt{\alpha}}) \tag{3.58}$$

Applying the relevant boundary condition, we get

$$C_5 = 0 \tag{3.59}$$

Now, for $z = t_1$

$$Z(z) = 0 \tag{3.60}$$

It implies that

$$\frac{\nu t_1}{\sqrt{\alpha}} = \frac{(2l-1)\pi}{2} \tag{3.61}$$

Or,

$$\nu = \frac{(2l-1)\sqrt{\alpha}\pi}{2t_1} \tag{3.62}$$

With all homogeneous boundary conditions satisfied, we combine the separated functions:

$$\theta_t = C_1 C_2 C_3 C_6 \cos(\frac{\beta x}{\sqrt{\alpha}}) \cos(\frac{\eta y}{\sqrt{\alpha}}) \cos(\frac{\nu z}{\sqrt{\alpha}}) \exp(-\zeta^2 t) \tag{3.63}$$

Or,

$$\theta_t = A_{mnl} \cos(\frac{\beta x}{\sqrt{\alpha}}) \cos(\frac{\eta y}{\sqrt{\alpha}}) \cos(\frac{\nu z}{\sqrt{\alpha}}) \exp(-\zeta^2 t) \tag{3.64}$$

where $C_1 C_2 C_3 C_6 = A_{mnl}$ and $\zeta^2 = \beta^2 + \eta^2 + \nu^2$

The most general solution is now constructed by a summation of all so-

lutions

$$\theta_t = \sum_{m=0}^{\infty}\sum_{n=0}^{\infty}\sum_{l=1}^{\infty} A_{mnl}\cos(\frac{\beta x}{\sqrt{\alpha}})\cos(\frac{\eta y}{\sqrt{\alpha}})\cos(\frac{\nu z}{\sqrt{\alpha}})\exp(-\zeta^2 t) \tag{3.65}$$

For simplicity, (3.65) can be written as

$$\theta_t = M_1 + M_2 + M_3 + M_4 \tag{3.66}$$

where

$$M_1 = \sum_{l=1}^{\infty} A_{00l}\cos(\frac{\nu z}{\sqrt{\alpha}})\exp(-t\nu^2) \tag{3.67}$$

$$M_2 = \sum_{m=1}^{\infty}\sum_{l=1}^{\infty}\left(A_{m0l}\cos\left(\frac{m\pi}{a}x\right)\cos\left(\frac{\nu z}{\sqrt{\alpha}}\right)\exp\left(-t\left(\left(\frac{m\pi\sqrt{\alpha}}{a}\right)^2+\nu_l^2\right)\right)\right) \tag{3.68}$$

$$M_3 = \sum_{n=1}^{\infty}\sum_{l=1}^{\infty}\left(A_{0nl}\cos\left(\frac{n\pi}{b}x\right)\cos\left(\frac{\nu z}{\sqrt{\alpha}}\right)\exp\left(-t\left(\left(\frac{\bar{n}\pi\sqrt{\alpha_1}}{b}\right)^2+\nu_l^2\right)\right)\right) \tag{3.69}$$

$$\begin{aligned} M_4 = \sum_{m=1}^{\infty}\sum_{n=1}^{\infty}\sum_{l=1}^{\infty}\Bigg(A_{mnl}\cos\left(\frac{m\pi}{a}x\right)\cos\left(\frac{n\pi}{b}y\right)\cos\left(\frac{\nu z}{\sqrt{\alpha}}\right) \\ \exp\left(-t\left(\left(\frac{\bar{m}\pi\sqrt{\alpha_1}}{a}\right)^2+\left(\frac{\bar{n}\pi\sqrt{\alpha_1}}{b}\right)^2+\nu_l^2\right)\right)\Bigg) \end{aligned} \tag{3.70}$$

The final step is to determine the Fourier constants using the non-homogeneous initial condition of this problem which will be explained later.

3.2 Steady-state thermal modelling of an N-layer rectangular structure

3.2.1 Problem Statement

At first, let us consider a rectangular structure with N different layers containing only one rectangular heat source as shown in Fig. 3.2 (The effect of multiple heat sources will be considered later.). The thickness and thermal

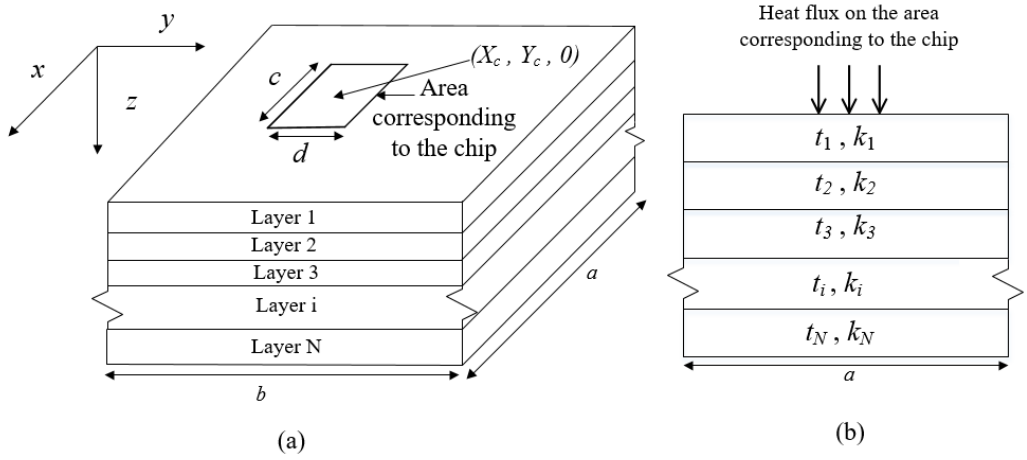


Figure 3.2: (a) Schematic of an N-layer structure (b) Side view of the structure with heat flux

conductivity of j^{th} layer of the rectangular structure in the Fig. 3.2 are t_j and k_j respectively. The bottom surface of the structure has a convection

coefficient h and is cooled convectively by a cooling fluid of uniform temperature T_f. The rectangular heat source is situated on the surface of layer 1. The position of the source is given by its centre $(X_C, Y_C, 0)$. The length and width of it are c and d respectively. This source generates heat Q uniformly over the surface it is situated. It is also assumed all the surfaces of the rectangular structure are adiabatic except the bottom surface which is subject to the convective boundary condition. Now, the governing equation of the system is Laplace‘s equation given in (3.71:

$$\frac{\partial^2\theta_i}{\partial x^2} + \frac{\partial^2\theta_i}{\partial y^2} + \frac{\partial^2\theta_i}{\partial z^2} = 0 \tag{3.71}$$

where θ_i is the temperature rise of the i^{th} layer with respect to the temperature of the cooling fluid.

Underneath the heat source, the first layer is subject to the boundary condition (3.72).

$$\left.\frac{\partial\theta_1}{\partial z}\right|_{z=0} = -\frac{Q}{k_1 cd} \tag{3.72}$$

Outside the source, the boundary condition is

$$\left.\frac{\partial\theta_1}{\partial z}\right|_{z=0} = 0. \tag{3.73}$$

Considering the perfect contact between the layers, the boundary conditions

at the interfaces are

$$k_i \frac{\partial \theta_i}{\partial z}\bigg|_{z=z_i} = k_{i+1} \frac{\partial \theta_{i+1}}{\partial z}\bigg|_{z=z_i} \tag{3.74}$$

and

$$\theta_i(x, y, z_i) = \theta_{i+1}(x, y, z_i) \tag{3.75}$$

where

$$z_i = \sum_{j=1}^{i} t_j.$$

The boundary condition for the bottom layer is

$$k_N \frac{\partial \theta_N}{\partial z}\bigg|_{z=z_N} = -h\theta_N|_{z=z_N}. \tag{3.76}$$

3.2.2 Problem Solution: Rectangular $N-$ Layer Fourier method (RNLF Method)

Top layer (Layer 1)

The governing equation and all the boundary conditions are homogeneous except (3.72). Therefore, this problem can be solved by the separation of

variables method. As discussed before, the solution can be expressed as

$$\begin{aligned}\theta_i(x,y,z) &= A_{i0} + B_{i0}z + \sum_{m=1}^{\infty}\cos(\lambda_m x)[A_{im}\cosh(\lambda_m z) + B_{im}\sinh(\lambda_m z)] \\ &+ \sum_{n=1}^{\infty}\cos(\delta_n y)[A_{in}\cosh(\delta_n z) + B_{in}\sinh(\delta_n z)] \\ &+ \sum_{m=1}^{\infty}\sum_{n=1}^{\infty}\cos(\lambda_m x)\cos(\delta_n y)[A_{imn}\cosh(\beta_{mn} z) + B_{imn}\sinh(\beta_{mn} z)]\end{aligned} \tag{3.77}$$

where $\lambda_m = m\pi/a$, $\delta_n = n\pi/b$ and $\beta_{mn} = \sqrt{(\lambda_m^2 + \delta_n^2)}$.

Considering the first layer boundary condition:

$$\begin{aligned}k_1\frac{\partial\theta}{\partial z}\bigg|_{z=0} &= k_1 B_{10} + k_1\sum_{m=1}^{\infty} B_{im}\lambda_m\cos(\lambda_m x) \\ &+ k_1\sum_{n=1}^{\infty} B_{1n}\delta_n\cos(\delta_n y) + k_1\sum_{m=1}^{\infty}\sum_{n=1}^{\infty}\beta_{1mn}\cos(\lambda_m x)\cos(\delta_n y)\end{aligned} \tag{3.78}$$

Now considering the following integration over the surface $z = 0$ for the x direction coefficients:

$$\int_0^a\int_0^b\left(k_1\frac{\partial\theta}{\partial z}\bigg|_{z=0}\right)\cos(\lambda_m x)\mathrm{d}x\mathrm{d}y = \lambda_m k_1 B_{1m}\int_0^a\int_0^b\cos^2(\lambda_m x)\mathrm{d}x\mathrm{d}y$$

Therefore,

$$\int_{X_c-c/2}^{X_c+c/2}\left(-\frac{Q}{cd}\right)\cos(\lambda_m x)\mathrm{d}x\int_{Y_c-d/2}^{Y_c+d/2}\mathrm{d}y = k_1 B_{1m}\int_0^a\cos^2(\lambda_m x)\mathrm{d}x\int_0^b\mathrm{d}y$$

Hence,

$$B_{1m} = \frac{-4Q\cos(\lambda_m X_c)\sin(\lambda_m c/2)}{abck_1\lambda_m^2} \tag{3.79}$$

Similarly,in the y direction,

$$B_{1n} = \frac{-4Q\cos(\delta_n Y_c)\sin(\delta_n d/2)}{abdk_1\delta_n^2} \tag{3.80}$$

And for the cross-coefficient B_{1mn},

$$B_{1mn} = \frac{-16Q\cos(\lambda_m X_c)\sin(\lambda_m c/2)\cos(\delta_n Y_c)\sin(\delta_n d/2)}{abcdk_1\lambda_m\delta_n\beta_{mn}} \tag{3.81}$$

And for B_{10},

$$\int_{X_c-c/2}^{X_c+c/2}\left(-\frac{Q}{cd}\right)\mathrm{d}x\int_{Y_c-d/2}^{Y_c+d/2}\mathrm{d}y = k_1 B_{10}\int_0^a \mathrm{d}x\int_0^b \mathrm{d}y$$

Therefore,

$$B_{10} = \frac{-Q}{k_1 ab} \tag{3.82}$$

Other Fourier coefficients A_{1m}, A_{1n}, A_{1mn} and A_{10} can be determined from the relevant boundary conditions which is explained in the next sections.

Bottom layer

For the bottom layer or N^{th} layer, the following relation can be obtained by replacing (3.77) in (3.76) and equating the coefficient of $\cos(\lambda_m)$ of both

sides :

$$\frac{-h}{k_N}\Big[A_{Nm}\cosh(\lambda_m z_N) + B_{Nm}\sinh(\lambda_m z_N)\Big] = A_{Nm}\lambda_m\sinh(\lambda_m z_N) + B_{Nm}\lambda_m\cosh(\lambda_m z_N)$$

Therefore,

$$B_{Nm} = -\sigma_N(\lambda_m)A_{Nm} \tag{3.83}$$

where

$$\sigma_N(\lambda_m) = \frac{\lambda_m\sinh(\lambda_m z_N) + h/k_N\cosh(\lambda_m z_N)}{\lambda_m\cosh(\lambda_m z_N) + h/k_N\sinh(\lambda_m z_N)} \tag{3.84}$$

It should be mentioned that $\sigma_N(\delta_n)$ and $\sigma_N(\beta_{mn})$ can be obtained by replacing λ_m with δ_n and β_{mn} respectively. If the convection coefficient h is very large, the bottom surface becomes isothermal. In this case,

$$\sigma_N(\lambda_m) = \coth(\lambda_m z_N) \tag{3.85}$$

Middle layers ($i < N$)

The interface boundary conditions (3.74) and (3.75) are applied in the middle layers. To illustrate the process, consider a three-layer structure for the sake of simplicity. In the interface between first and second layer, following relations can be obtained from (3.74):

$$A_{2m}\sinh(\lambda_m t_1) + B_{2m}\cosh(\lambda_m t_1) = k_2/k_1(A_{1m}\sinh(\lambda_m t_1) + B_{1m}\cosh(\lambda_m t_1)) \tag{3.86}$$

From (3.75),

$$A_{2m}\cosh(\lambda_m t_1)+B_{2m}\sinh(\lambda_m t_1) = A_{1m}\cosh(\lambda_m t_1)+B_{1m}\sinh(\lambda_m t_1) \quad (3.87)$$

Now,(3.87)$\times\cosh(\lambda_m t_1)$ - (3.86)$\times\sinh(\lambda_m t_1)$ yields the following relation:

$$A_{2m} = A_{1m}\phi_1 + B_{1m}\psi_1 \quad (3.88)$$

where

$$\phi_1 = \cosh^2(\lambda_m t_1) - k_2/k_1 \sinh^2(\lambda_m t_1)$$

and,

$$\psi_1 = \sinh(\lambda_m t_1)\cosh(\lambda_m t_1)(1 - k_2/k_1)$$

Similarly,

$$B_{2m} = -(A_{1m}\psi_1 + B_{1m}\rho_1) \quad (3.89)$$

where

$$\rho_1 = \sinh^2(\lambda_m t_1) - k_2/k_1 \cosh^2(\lambda_m t_1)$$

Similarly, it can be shown that for other layers,

$$A_{3m} = A_{2m}\phi_2 + B_{2m}\psi_2 \quad (3.90)$$

$$B_{3m} = -(A_{2m}\psi_2 + B_{2m}\rho_2) \quad (3.91)$$

where

$$\phi_2 = \cosh^2(\lambda_m(t_1+t_2)) - k_2/k_3 \sinh^2(\lambda_m(t_1+t_2))$$

$$\psi_2 = \sinh(\lambda_m(t_1+t_2)) \cosh(\lambda_m(t_1+t_2))(1-k_2/k_3)$$

$$\rho_2 = \sinh^2(\lambda_m(t_1+t_2)) - k_2/k_3 \cosh^2(\lambda_m(t_1+t_2))$$

Now, from Eq.(3.91) and (3.90),

$$\frac{B_{3m}}{A_{3m}} = \frac{-(A_{2m}\psi_2 + B_{2m}\rho_2)}{A_{2m}\phi_2 + B_{2m}\psi_2}$$

From (3.83)

$$\sigma_3 = \frac{(A_{2m}\psi_2 + B_{2m}\rho_2)}{A_{2m}\phi_2 + B_{2m}\psi_2}$$

Hence,

$$\sigma_2 = \frac{-B_{2m}}{A_{2m}} = \frac{\sigma_3\phi_2 - \psi_2}{\sigma_3\psi_2 - \rho_2} \tag{3.92}$$

Similarly,

$$\sigma_1 = \frac{-B_{1m}}{A_{1m}} = \frac{\sigma_2\phi_1 - \psi_1}{\sigma_2\psi_1 - \rho_1} \tag{3.93}$$

This process may be repeated for successive layers in the case of an N layer structure,i.e. σ_i may be found from σ_{i+1} from the following equation:

$$\sigma_i = \frac{-B_{im}}{A_{im}} = \frac{\sigma_{i+1}\phi_i - \psi_i}{\sigma_{i+1}\psi_i - \rho_i} \tag{3.94}$$

where

$$\phi_i = \cosh^2(\lambda_m \sum_{j=1}^{i} t_j) - k_i/k_{i+1} \sinh^2(\lambda_m \sum_{j=1}^{i} t_j)$$

$$\psi_i = \sinh(\lambda_m \sum_{j=1}^{i} t_j) \cosh(\lambda_m \sum_{j=1}^{i} t_j)(1 - k_i/k_{i+1})$$

$$\rho_i = \sinh^2(\lambda_m \sum_{j=1}^{i} t_j) - k_i/k_{i+1} \cosh^2(\lambda_m \sum_{j=1}^{i} t_j)$$

Eq.(3.94) thus provides a route to calculate all σ_i starting from σ_{N-1}: σ_{N-1} from σ_N, σ_{N-2} from σ_{N-1}, σ_{N-3} from σ_{N-2} and so on. Once σ_1 is obtained by this successive substitution method, A_{1m} is obtained from Eq.(3.83) as B_{1m} is directly calculated from (3.79). Similarly, $\sigma_1(\delta_n)$ and $\sigma_1(\beta_{mn})$ can be obtained and from these A_{1n} and A_{1mn} can be calculated directly. A block diagram is given in Figure 3.3 . to illustrate this process. It now only remains

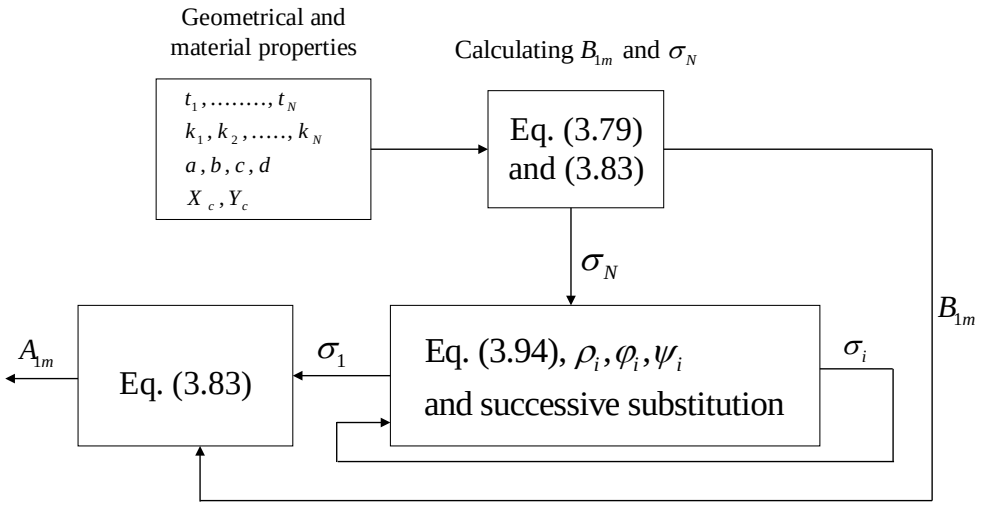


Figure 3.3: Process to determine A_{1m}

to find A_{10}. For the sake of simplicity, a two-layer structure is considered. From the convective boundary condition, following relation is obtained:

$$-(h/k_2)A_{20} = B_{20}(1 + h(t_1 + t_2)/k_2) \tag{3.95}$$

From the interface boundary condition (1.4),

$$k_1 B_{10} = k_2 B_{20} \tag{3.96}$$

From (3.96),

$$B_{20} = \frac{-Q}{k_2 ab} \tag{3.97}$$

Now, substituting B_{20} in (3.96),

$$A_{20} = \frac{-Q}{ab}\left(\frac{t_1 + t_2}{k_2} + \frac{1}{h}\right) \tag{3.98}$$

Again from (1.5),

$$A_{10} + B_{10}t_1 = A_{20} + B_{20}t_1$$

Hence,

$$A_{10} = \frac{Q}{ab}\left(\frac{t_1}{k_1} + \frac{t_2}{k_2} + \frac{1}{h}\right) \tag{3.99}$$

Similarly, for an N layer structure, it can be shown that

$$A_{10} = \frac{Q}{ab}\left(\sum_{i=1}^{N} \frac{t_i}{k_i} + \frac{1}{h}\right) \tag{3.100}$$

As the heat problem is linear, if multiple heat sources are present, temperature field is given simply by the summation of the individual temperature field produced by each heat source considered alone.

3.3 Transient thermal modelling of an N-layer rectangular structure

3.3.1 Problem Statement

The physical structure is identical to that used in the previous section. Therefore, it is not repeated here. The system is governed by the following equation:

$$\frac{\partial^2 \theta_i}{\partial x^2} + \frac{\partial^2 \theta_i}{\partial y^2} + \frac{\partial^2 \theta_i}{\partial z^2} = \frac{1}{\alpha_i} \frac{\partial \theta_i}{\partial t} \tag{3.101}$$

At $t = 0$, the initial condition is

$$\theta_i = 0 \tag{3.102}$$

The heat flux is a step input such that it changes instantaneously from zero for $t < 0$ to q_0 for $t \geq 0$. The system is subject to the following boundary conditions. For the first layer and underneath the heat source,

$$\left. \frac{\partial \theta_1}{\partial z} \right|_{z=0} = -\frac{q_0}{k_1} = -\frac{Q}{k_1 cd} \tag{3.103}$$

Outside the source, the boundary condition is

$$\left.\frac{\partial \theta_1}{\partial z}\right|_{z=0} = 0. \tag{3.104}$$

Because of the adiabatic sides of the structure,

$$\left.\frac{\partial \theta_i}{\partial x}\right|_{x=0,a} = 0 \text{ and } \left.\frac{\partial \theta_i}{\partial y}\right|_{y=0,b} = 0.$$

Assuming perfect thermal contact between the layers, the boundary conditions at the interfaces are

$$k_i \left.\frac{\partial \theta_{i,s}}{\partial z}\right|_{z=z_i} = k_{i+1} \left.\frac{\partial \theta_{(i+1),s}}{\partial z}\right|_{z=z_i} \tag{3.105}$$

and

$$\theta_i(x, y, z_i) = \theta_{i+1}(x, y, z_i) \tag{3.106}$$

where

$$z_i = \sum_{j=1}^{i} t_j.$$

The boundary condition for the bottom layer is

$$k_N \left.\frac{\partial \theta_N}{\partial z}\right|_{z=z_N} = -h\theta_N \Big|_{z=z_N} \tag{3.107}$$

θ_i can be written as a sum of the steady-state solution ($\theta_{i,s}$) and the transient solution ($\theta_{i,t}$):

$$\theta_i = \theta_{i,s} + \theta_{i,t}. \tag{3.108}$$

Now, $\theta_{i,s}$ is subject to the following boundary conditions. For the first layer and underneath the heat source,

$$\left.\frac{\partial \theta_{1,s}}{\partial z}\right|_{z=0} = -\frac{q_0}{k_1} = -\frac{Q}{k_1 cd} \tag{3.109}$$

Outside the source, the boundary condition is

$$\left.\frac{\partial \theta_{1,s}}{\partial z}\right|_{z=0} = 0. \tag{3.110}$$

Because of the adiabatic sides of the structure,

$$\left.\frac{\partial \theta_{i,s}}{\partial x}\right|_{x=0,a} = 0 \text{ and } \left.\frac{\partial \theta_{i,s}}{\partial y}\right|_{y=0,b} = 0.$$

Assuming perfect thermal contact between the layers, the boundary conditions at the interfaces are

$$k_i \left.\frac{\partial \theta_{i,s}}{\partial z}\right|_{z=z_i} = k_{i+1} \left.\frac{\partial \theta_{(i+1),s}}{\partial z}\right|_{z=z_i} \tag{3.111}$$

and

$$\theta_{i,s}(x, y, z_i) = \theta_{(i+1),s}(x, y, z_i) \tag{3.112}$$

where

$$z_i = \sum_{j=1}^{i} t_j.$$

The boundary condition for the bottom layer is

$$k_N \frac{\partial \theta_{N,s}}{\partial z}\bigg|_{z=z_N} = -h\theta_{N,s}\bigg|_{z=z_N} \tag{3.113}$$

$\theta_{i,t}$ is subject to similar boundary conditions for $t \geq 0$ except

$$\frac{\partial \theta_{1,t}}{\partial z}\bigg|_{z=0} = 0. \tag{3.114}$$

The boundary condition for the bottom layer is given as

$$\theta_{N,t}\bigg|_{z=z_N} = 0. \tag{3.115}$$

$\theta_{i,t}$ is subject to the following initial condition.

$$\theta_{i,t} = -\theta_{i,s} \tag{3.116}$$

3.4 Problem Solution: Transient Rectangular N- Layer Fourier method (TRNLF Method)

The steady-state part of (3.108) is derive previously. For the transient part, the governing equation and all the boundary conditions are linear and homo-

geneous. The initial condition is non-homogeneous. Therefore, the transient problem can be solved by the separation of variables method. The transient solution can be expressed as

$$\theta_{i,t} = \sum_{\bar{m}=0}^{\infty}\sum_{\bar{n}=0}^{\infty}\sum_{\bar{l}=1}^{\infty} A_{\bar{m}\bar{n}\bar{l}} X_{i\bar{n}}(x) Y_{i\bar{n}}(y) Z_{i\bar{l}}(z) T_i(t). \tag{3.117}$$

As we are mainly interested in the temperature distribution of the first layer, it is sufficient to know $\theta_{1,t}$ which is given by

$$\theta_{1,t} = \sum_{\bar{m}=0}^{\infty}\sum_{\bar{n}=0}^{\infty}\sum_{\bar{l}=1}^{\infty} A_{\bar{m}\bar{n}\bar{l}} X_{1\bar{m}}(x) Y_{1\bar{n}}(y) Z_{1\bar{l}}(z) T_1(t) \tag{3.118}$$

where

$$X_{1\bar{m}}(x) = \cos\left(\frac{\bar{m}\pi}{a}x\right), Y_{1\bar{n}}(y) = \cos\left(\frac{\bar{n}\pi}{b}y\right), T_1(t) = \exp(-\zeta^2 t)$$

and

$$Z_{1\bar{l}}(z) = A_{1\bar{l}}\sin\left(\frac{\nu_{l'}z}{\sqrt{\alpha_1}}\right) + B_{1\bar{l}}\cos\left(\frac{\nu_{l'}z}{\sqrt{\alpha_1}}\right).$$

Here,

$$\zeta^2 = \left(\frac{\bar{m}\pi\sqrt{\alpha_1}}{a}\right)^2 + \left(\frac{\bar{n}\pi\sqrt{\alpha_1}}{b}\right)^2 + {\nu_{\bar{l}}}^2.$$

The relevant coefficients and eigenvalues ($\nu_{\bar{l}}$) are calculated in the next sections.

3.4.1 Generalised Orthogonal Expansion Technique

This technique is well-documented in [79] for one-dimensional cases. However, it can be extended for three-dimensional cases as follows.

(a) Determination of the eigenvalues

For the sake of clarity, a rectangular structure of two layers is considered here. The eigenfunctions corresponding to each layer are given below.

$$Z_{1\bar{l}}(z) = A_{1\bar{l}} \sin\left(\frac{\nu_{\bar{l}} z}{\sqrt{\alpha_1}}\right) + B_{1\bar{l}} \cos\left(\frac{\nu_{\bar{l}} z}{\sqrt{\alpha_1}}\right) \tag{3.119}$$

$$Z_{2\bar{l}}(z) = A_{2\bar{l}} \sin\left(\frac{\nu_{\bar{l}} z}{\sqrt{\alpha_2}}\right) + B_{2\bar{l}} \cos\left(\frac{\nu_{\bar{l}} z}{\sqrt{\alpha_2}}\right) \tag{3.120}$$

Applying (3.114) to (3.119), $A_{1\bar{l}}$ is found to be 0. Therefore,

$$Z_{1\bar{l}}(z) = B_{1l'} \cos\left(\frac{\nu_{l'} z}{\sqrt{\alpha_1}}\right). \tag{3.121}$$

Now, applying relevant boundary conditions to (3.119) and (3.120); it is found that

$$\frac{k_1}{k_2}\frac{B_{1\bar{l}}}{\sqrt{\alpha_1}} \sin\left(\frac{\nu_{\bar{l}} t_1}{\sqrt{\alpha_1}}\right) + \frac{A_{2\bar{l}}}{\sqrt{\alpha_2}} \cos\left(\frac{\nu_{\bar{l}} t_1}{\sqrt{\alpha_2}}\right) - \frac{B_{2\bar{l}}}{\sqrt{\alpha_2}} \sin\left(\frac{\nu_{\bar{l}} t_1}{\sqrt{\alpha_2}}\right) = 0, \tag{3.122}$$

$$B_{1\bar{l}}\cos\left(\frac{\nu_{\bar{l}}t_1}{\sqrt{\alpha_1}}\right) - A_{2\bar{l}}\sin\left(\frac{\nu_{\bar{l}}t_1}{\sqrt{\alpha_2}}\right) - B_{2\bar{l}}\cos\left(\frac{\nu_{\bar{l}}t_1}{\sqrt{\alpha_2}}\right) = 0 \tag{3.123}$$

and

$$A_{2\bar{l}}\sin\left(\frac{\nu_{\bar{l}}(t_1+t_2)}{\sqrt{\alpha_2}}\right) + B_{2\bar{l}}\cos\left(\frac{\nu_{\bar{l}}(t_1+t_2)}{\sqrt{\alpha_2}}\right) = 0 \tag{3.124}$$

Therefore,

$$AX = 0 \tag{3.125}$$

where A is given by the following matrix:

$$\begin{bmatrix} \frac{k_1}{k_2}\frac{1}{\sqrt{\alpha_1}}\sin\left(\frac{\nu_{\bar{l}}t_1}{\sqrt{\alpha_1}}\right) & \frac{1}{\sqrt{\alpha_2}}\cos\left(\frac{\nu_{\bar{l}}t_1}{\sqrt{\alpha_2}}\right) & -\frac{1}{\sqrt{\alpha_2}}\sin\left(\frac{\nu_{\bar{l}}t_1}{\sqrt{\alpha_2}}\right) \\ \cos\left(\frac{\nu_{\bar{l}}t_1}{\sqrt{\alpha_1}}\right) & -\sin\left(\frac{\nu_{\bar{l}}t_1}{\sqrt{\alpha_2}}\right) & -\cos\left(\frac{\nu_{\bar{l}}t_1}{\sqrt{\alpha_2}}\right) \\ 0 & \sin\left(\frac{\nu_{\bar{l}}(t_1+t_2)}{\sqrt{\alpha_2}}\right) & \cos\left(\frac{\nu_{\bar{l}}(t_1+t_2)}{\sqrt{\alpha_2}}\right) \end{bmatrix}$$

and

$$X = \begin{bmatrix} B_{1\bar{l}} \\ A_{2\bar{l}} \\ B_{2\bar{l}} \end{bmatrix}$$

Now, For X to have a non-trivial solution the following relation must hold:

$$\det(A) = 0 \tag{3.126}$$

This is a transcendental equation and it must be solved numerically to find the first N eigenvalues $(\nu_1, \nu_2, \nu_3, \nu_4, ..., \nu_N)$. The flowchart of the algorithm used in this work to find the first N eigenvalues is given in Fig. 3.4. This flowchart is described here briefly. The main objective of this method is to find the first N positive roots of the equation denoted by (3.126). The basic inputs are increment Δx and the number of desired eigenvalues N. At first, it is examined whether there is any root of Eq. (3.126) in [0, Δx] by checking if $\det(A(\bar{l}))$ changes sign. A sign-change implies there is a root in this interval and it is found by applying a standard MATLAB function fzero. If the root is r, then it is stored in array and the search continues in the interval [r, $r + \Delta x$]. This process is continued until N roots are found.

(b) Determination of the coefficients of the eigenfunctions

The system described by (3.126) is linear and homogeneous. Therefore, the non-trivial solution of (3.126) can be expressed as a multiple of any Fourier coefficients. Therefore, without the loss of generality $B_{1\bar{l}}$ can be considered equal to 1. Setting $B_{1\bar{l}} = 1$ in (3.122) and (3.123) a set of Fourier coefficients can be obtained corresponding to each eigenvalue by using any standard method (for example, matrix inversion or Cramer's rule). For example, A_{21} and B_{21} can be obtained from ν_1, A_{22} and B_{22} can be obtained from ν_2 and so on.

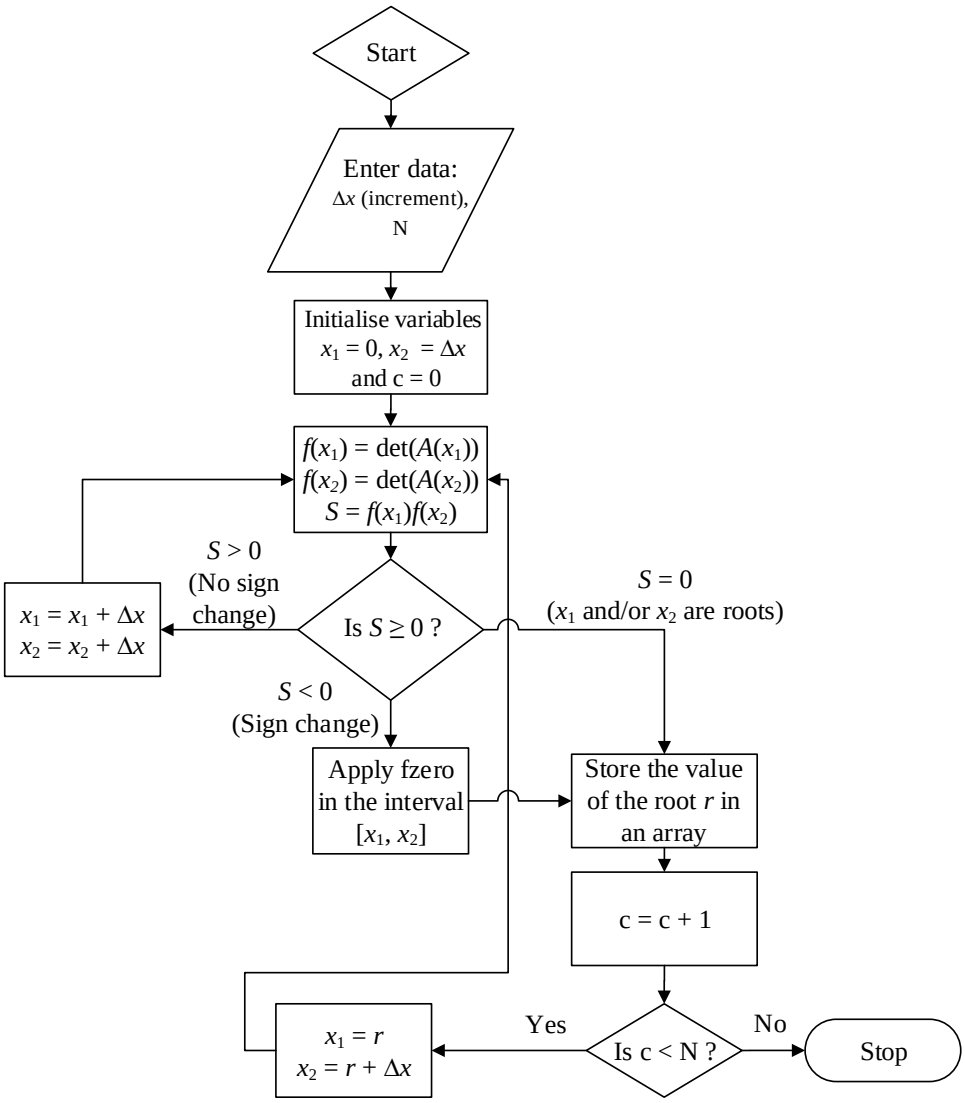


Figure 3.4: Flowchart to determine the first N eigenvalues

3.4.2 Determination of $A_{00\bar{l}}$, $A_{\bar{m}0\bar{l}}$, $A_{0\bar{n}\bar{l}}$ and $A_{\bar{m}\bar{n}\bar{l}}$

Now it remains to find $A_{\bar{m}\bar{n}\bar{l}}$ (of (3.118)) which can be expressed by the following equation:

$$A_{\bar{m}\bar{n}\bar{l}} = \frac{1}{N_{\bar{m}} N_{\bar{n}} N_{\bar{l}}}(S_1 + S_2) \tag{3.127}$$

where

$$S_1 = \frac{k_1}{\alpha_1}\int_0^a \int_0^b \int_0^{t_1} \left(F_1(x,y,z)\cos\left(\frac{\bar{m}\pi}{a}x\right)\cos\left(\frac{\bar{n}\pi}{b}y\right) Z_{1\bar{l}}\right)\mathrm{d}x\mathrm{d}y\mathrm{d}z$$

and

$$S_2 = \frac{k_2}{\alpha_2}\int_0^a \int_0^b \int_{t_1}^{t_1+t_2} \left(F_2(x,y,z)\cos\left(\frac{\bar{m}\pi}{a}x\right)\cos\left(\frac{\bar{n}\pi}{b}y\right) Z_{2\bar{l}}\right)\mathrm{d}x\mathrm{d}y\mathrm{d}z$$

Here, F_1 and F_2 are initial temperature distributions in layer 1 and 2 respectively. $N_{\bar{m}}$, $N_{\bar{n}}$ and $N_{\bar{l}}$ are given by the following equations.

$$N_{\bar{m}} = \int_0^a \cos^2\left(\frac{\bar{m}\pi}{a}x\right)\mathrm{d}x = \begin{cases} a & \text{if } \bar{m} = 0 \\ a/2 & \text{otherwise} \end{cases} \tag{3.128}$$

$$N_{\bar{n}} = \int_0^b \cos^2\left(\frac{\bar{n}\pi}{b}y\right)\mathrm{d}y = \begin{cases} b & \text{if } \bar{n} = 0 \\ b/2 & \text{otherwise} \end{cases} \tag{3.129}$$

$$N_{\bar{l}} = \frac{k_1}{\alpha_1}\int_0^{t_1} Z_{1\bar{l}}^2 \mathrm{d}z + \frac{k_2}{\alpha_2}\int_{t_1}^{t_1+t_2} Z_{2\bar{l}}^2 \mathrm{d}z \tag{3.130}$$

Now, for ease of implementation (3.118) can be written as:

$$\theta_{1,t} = M_1 + M_2 + M_3 + M_4 \tag{3.131}$$

where

$$M_1 = \sum_{\bar{l}=1}^{\infty} A_{00\bar{l}} Z_{1\bar{l}} \exp(-t\nu_{\bar{l}}^2) \tag{3.132}$$

$$M_2 = \sum_{\bar{m}=1}^{\infty}\sum_{\bar{l}=1}^{\infty}\left(A_{\bar{m}0\bar{l}}\cos\left(\frac{\bar{m}\pi}{a}x\right)Z_{1\bar{l}}\exp\left(-t\left(\left(\frac{\bar{m}\pi\sqrt{\alpha_1}}{a}\right)^2+\nu_{\bar{l}}^2\right)\right)\right) \tag{3.133}$$

$$M_3 = \sum_{\bar{n}=1}^{\infty}\sum_{\bar{l}=1}^{\infty}\left(A_{0\bar{n}\bar{l}}\cos\left(\frac{\bar{n}\pi}{b}x\right)Z_{1\bar{l}}\exp\left(-t\left(\left(\frac{\bar{n}\pi\sqrt{\alpha_1}}{b}\right)^2+\nu_{\bar{l}}^2\right)\right)\right) \tag{3.134}$$

$$M_4 = \sum_{\bar{m}=1}^{\infty}\sum_{\bar{n}=1}^{\infty}\sum_{\bar{l}=1}^{\infty}\left(A_{\bar{m}\bar{n}\bar{l}}\cos\left(\frac{\bar{m}\pi}{a}x\right)\cos\left(\frac{\bar{n}\pi}{b}y\right)Z_{1\bar{l}}\exp\left(-t\left(\left(\frac{\bar{m}\pi\sqrt{\alpha_1}}{a}\right)^2+\left(\frac{\bar{n}\pi\sqrt{\alpha_1}}{b}\right)^2+\nu_{\bar{l}}^2\right)\right)\right) \tag{3.135}$$

Now, from (3.77),

From (2) and (3),

$$F_1 = -\theta_{1,s}(x, y, z) \tag{3.136}$$

and

$$F_2 = -\theta_{2,s}(x, y, z) \tag{3.137}$$

where $\theta_{1,s}(x, y, z)$ and $\theta_{2,s}(x, y, z)$ can be derived from (3.77). As

$$\int_0^a \cos\left(\frac{m\pi}{a}x\right)\mathrm{d}x = 0 \text{ and } \int_0^b \cos\left(\frac{n\pi}{b}y\right)\mathrm{d}y = 0 \ ,$$

$$A_{00\bar{l}} = -\frac{1}{N_{\bar{l}}}\left[\frac{k_1}{\alpha_1}\int_0^{t_1} A_{10}Z_{1\bar{l}}\mathrm{d}z + \frac{k_2}{\alpha_2}\int_{t_1}^{t_1+t_2} A_{20}Z_{2\bar{l}}\mathrm{d}z + \frac{k_1}{\alpha_1}\int_0^{t_1} B_{10}zZ_{1\bar{l}}\mathrm{d}z + \frac{k_2}{\alpha_2}\int_{t_1}^{t_1+t_2} B_{20}zZ_{2\bar{l}}\mathrm{d}z\right]. \tag{3.138}$$

By using the orthogonality relations of the cosine function it can be shown that

$$\begin{aligned} A_{\bar{m}0\bar{l}} = -\frac{1}{N_{\bar{l}}}\Bigg[&\frac{k_1}{\alpha_1}\int_0^{t_1}\left(A_{1\bar{m}}\sinh\left(\frac{\bar{m}\pi}{a}z\right) + B_{1\bar{m}}\cosh\left(\frac{\bar{m}\pi}{a}z\right)\right)Z_{1barl}\mathrm{d}z \\ &+\frac{k_2}{\alpha_2}\int_{t_1}^{t_1+t_2}\left(A_{2\bar{m}}\cosh\left(\frac{\bar{m}\pi}{a}z\right) + B_2\sinh\left(\frac{\bar{m}\pi}{a}z\right)\right)Z_{2\bar{l}}\mathrm{d}z\Bigg] \end{aligned} \tag{3.139}$$

Similarly,

$$A_{0\bar{n}\bar{l}} = -\frac{1}{N_{\bar{l}}}\left[\frac{k_1}{\alpha_1}\int_0^{t_1}\left(A_{1\bar{n}}\cosh\left(\frac{\bar{n}\pi}{b}z\right)+B_{1\bar{n}}\sinh\left(\frac{\bar{n}\pi}{b}z\right)\right)Z_{1\bar{l}}\mathrm{d}z \right. \\ \left. +\frac{k_2}{\alpha_2}\int_{t_1}^{t_1+t_2}\left(A_{2\bar{n}}\cosh\left(\frac{\bar{n}\pi}{b}z\right)+B_{2\bar{n}}\sinh\left(\frac{\bar{n}\pi}{b}z\right)\right)Z_{2\bar{l}}\mathrm{d}z\right] \tag{3.140}$$

and

$$A_{\bar{m}\bar{n}\bar{l}} = -\frac{1}{N_{\bar{l}}}\left[\frac{k_1}{\alpha_1}\int_0^{t_1}\left(A_{1\bar{m}\bar{n}}\cosh(\beta_{\bar{m}\bar{n}}z)+B_{1\bar{m}\bar{n}}\sinh(\beta_{\bar{m}\bar{n}}z)\right)Z_{1\bar{l}}\mathrm{d}z \right. \\ \left. +\frac{k_2}{\alpha_2}\int_{t_1}^{t_1+t_2}\left(A_{2\bar{m}\bar{n}}\cosh(\beta_{\bar{m}\bar{n}}z)+B_{2\bar{m}\bar{n}}\sinh(\beta_{\bar{m}\bar{n}}z)\right)Z_{2\bar{l}}\mathrm{d}z\right]. \tag{3.141}$$

where

$$\beta_{\bar{m}\bar{n}} = \sqrt{\left(\frac{\bar{m}\pi}{a}\right)^2+\left(\frac{\bar{n}\pi}{b}\right)^2}$$

and A_{10}, A_{20}, B_{10}, B_{20}, $A_{1\bar{m}}$, $A_{2\bar{m}}$, $B_{1\bar{m}}$, $A_{1\bar{n}}$, $B_{1\bar{n}}$, $A_{1\bar{m}\bar{n}}$ and $B_{1\bar{m}\bar{n}}$ are the Fourier coefficients in the steady-state solution derived previously.

Now, the transient thermal modelling of a two-layer structure with a single heat source is formally completed. As the system is linear, for multiple heat sources, the temperature field is simply obtained by the summation of the individual temperature field produced by each heat source considered alone. As a result, the procedure detailed above can be used for transient thermal modelling of an N-layer rectangular structure with any number of rectangular heat sources on its top surface. The generalised expression (for

an N-layer structure) of the Fourier coefficients are:

$$A_{00\bar{l}} = -\frac{1}{N_{\bar{l}}}\left[\sum_{i=1}^{N}\frac{k_i}{\alpha_i}\int_{z_i}^{z_{i+1}}\left(A_{i0}+zB_{i0}\right)Z_{i\bar{l}}\mathrm{d}z\right] \tag{3.142}$$

$$A_{\bar{m}0\bar{l}} = -\frac{1}{N_{\bar{l}}}\left[\sum_{i=1}^{N}\frac{k_i}{\alpha_i}\int_{z_i}^{z_{i+1}}\left(A_{i\bar{m}}\cosh\left(\frac{\bar{m}\pi}{a}z\right)+B_{i\bar{m}}\sinh\left(\frac{\bar{m}\pi}{a}z\right)\right)Z_{i\bar{l}}\mathrm{d}z\right] \tag{3.143}$$

$$A_{0\bar{n}\bar{l}} = -\frac{1}{N_{\bar{l}}}\left[\sum_{i=1}^{N}\frac{k_i}{\alpha_i}\int_{z_i}^{z_{i+1}}\left(A_{i\bar{n}}\cosh\left(\frac{\bar{n}\pi}{b}z\right)+B_{i\bar{n}}\sinh\left(\frac{\bar{n}\pi}{b}z\right)\right)Z_{i\bar{l}}\mathrm{d}z\right] \tag{3.144}$$

and

$$A_{\bar{m}\bar{n}\bar{l}} = -\frac{1}{N_{\bar{l}}}\left[\sum_{i=1}^{N}\frac{k_i}{\alpha_i}\int_{z_i}^{z_{i+1}}\left(A_{i\bar{m}\bar{n}}\cosh(\beta_{\bar{m}\bar{n}}z)+B_{i\bar{m}\bar{n}}\sinh(\beta_{\bar{m}\bar{n}}z)\right)Z_{i\bar{l}}\mathrm{d}z\right] \tag{3.145}$$

where

$$N_{\bar{l}} = \sum_{i=1}^{N}\frac{k_i}{\alpha_i}\int_{z_i}^{z_{i+1}}Z_{i\bar{l}}^2\mathrm{d}z$$

and

$$Z_{i\bar{l}}(z) = A_{i\bar{l}}\sin\left(\frac{\nu_{\bar{l}}z}{\sqrt{\alpha_i}}\right)+B_{i\bar{l}}\cos\left(\frac{\nu_{\bar{l}}z}{\sqrt{\alpha_i}}\right) \tag{3.146}$$

It is important to highlight that the eigenvalues and the coefficients of eigen-

functions need only be determined once for a particular problem geometry. Once found, these can be readily used in the calculation of the temperature for any transient heat input. The complete procedure to determine the temperature of a particular point in space and time is explained in Fig. 3.5. For convenience, it is described here briefly. A major part of calculation of the

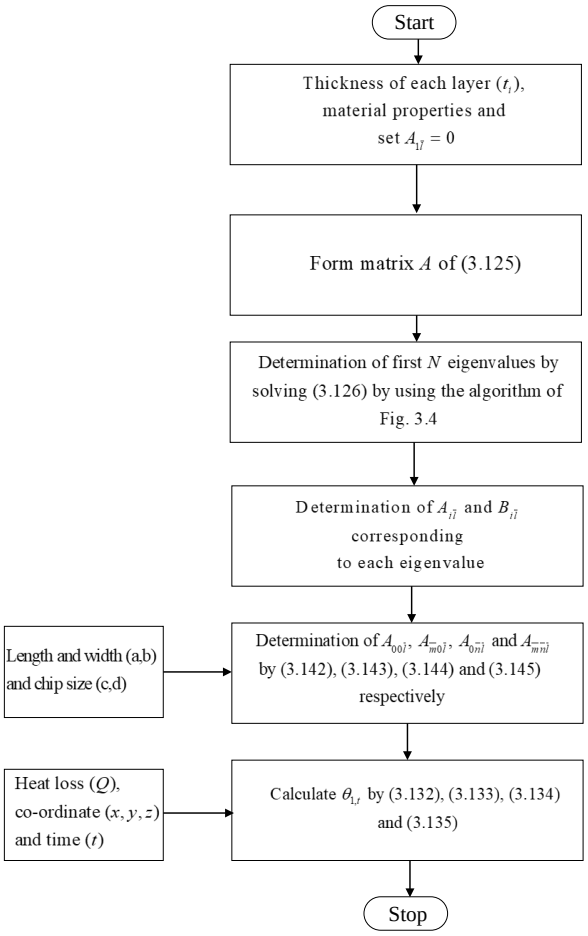


Figure 3.5: Flowchart to determine the temperature at a point in time and space

temperature of a particular point and time is the formation of matrix A and the subsequent determination of the first N roots of (3.126). In order to do that, thickness, thermal conductivity and thermal diffusivity of each layer. By using this information and setting $A_{1\bar{l}} = 0$, matrix A is formed. After that, first N eigenvalues are obtained by solving (3.126) . The next step is to find $A_{i\bar{l}}$ and $B_{i\bar{l}}$ corresponding to each eigenvalue. With the information of length and width of the structure and chip size, $A_{00\bar{l}}$, $A_{\bar{m}0\bar{l}}$, $A_{0\bar{n}\bar{l}}$ and $A_{\bar{m}\bar{n}\bar{l}}$ can be determined. Using these co-efficient and with the information of heat loss in each device, position (x,y,z) and time, temperature can be calculated. In real power electronic applications, the power losses in the semiconductor devices are far more complex than a simple step. Therefore, to apply the TRNLF method in practice it is necessary to determine the temperature-response to an arbitrary load profile. The waveshape in Fig. 3.6 ($f(t)$) is approximated by a sequence of a rectangular pulses. If θ is the temperature response to the waveshape then using the linearity of the system the following equation can be written.

$$\theta = a_1\theta_0 + (a_2 - a_1)\theta_1 + ... + (a_N - a_{N-1})\theta_{N-1} - a_N\theta_N \tag{3.147}$$

where θ_0 is the temperature response to heat pulse $u(t)$, θ_1 is the temperature response to $u(t - t_1)$, θ_2 is the temperature response to $u(t - t_2)$ and so on. If the waveshape is approximated by more rectangular pulses of shorter duration the accuracy of the result will tend to increase.

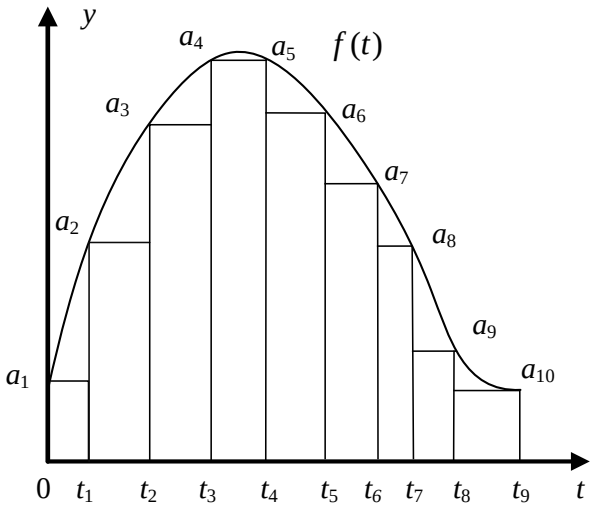


Figure 3.6: An arbitrary waveshape with staircase approximation

Chapter 4

Verification of the thermal models by COMSOL Multiphysics

In this chapter, the thermal models developed in the previous chapter are validated by COMSOL Multiphysics. At first, the RNLF method (steady-state thermal model is validated. After that, it is successfully applied to a power module. The TRNLF method (transient thermal modelling) is validated and applied in the same manner.

4.1 Validation of the steady-state model by simulation

In this work, a rectangular structure as described in Figure 4.1 is considered. There are 8 layers in total. The rationale behind choosing this particular structure is that it will be used for subsequent analysis. Key dimensions and properties of that structure are given in Table 4.1. The thermal model

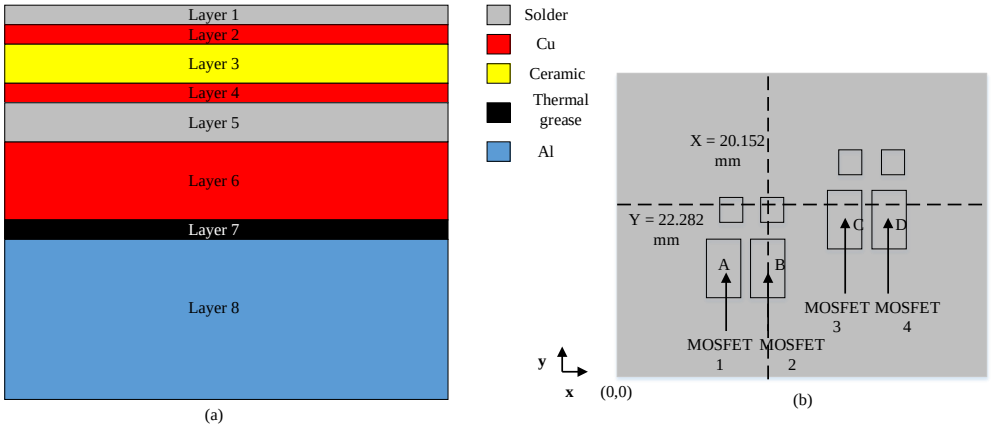


Figure 4.1: Cross-section of the structure considered for the verification of the thermal models

developed here is validated by COMSOL Multiphysics. Two lines Y = 22.282 mm and X = 20.152 mm on the surface of the model-structure are considered (Figure (4.1)). The boundary conditions are exactly the same as described in section and the temperature of the isothermal surface is 52.635^{o}C (The reason for choosing for this particular value is discussed later). Figures 4.2 and 4.3 show the comparison between the model and simulation data. Table

Table 4.1: Material assembly of the SiC power module

Material	Serial of the materials	Thickness (mm)	Thermal conductivity (W/m/K)
Solder	1	0.09	30
Copper	2	0.3	390
Si_3N_4	3	0.32	90
Copper	4	0.3	390
Solder	5	0.2	30
Copper baseplate	6	2.5	390
Thermal grease	7	0.07	30
Aluminium alloy	8	30.77	180

4.2 shows the difference between the model and simulation data for the centre points of the chip areas (A,B,C and D).

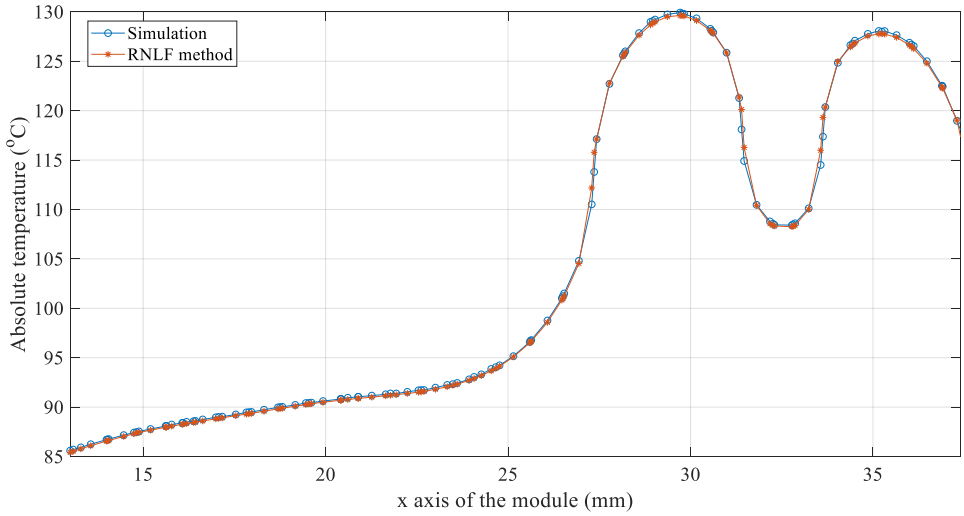


Figure 4.2: Comparison between the model and simulation along the line Y = 22.282 (mm)

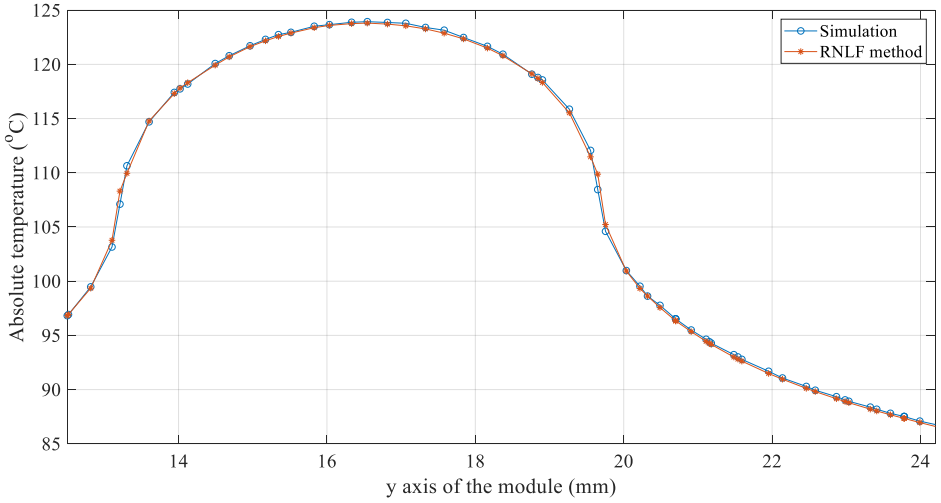


Figure 4.3: Comparison between the model and simulation along the line X = 20.152 (mm)

The line Y = 22.282 mm falls on the areas corresponding to MOSFET 3 and 4. Therefore, two peaks are observed. Between these peaks, one local minima is observed. Similarly, the line X = 20.152 mm falls on the area corresponding to MOSFET 2. Therefore, one peak is observed. It is also observed from the graphs that temperature distribution is not exactly uniform. There is approximately 5°C difference across the chip. These figures

Table 4.2: Comparison between the RNLF method and simulation

Position of the centre (mm)	Model temperature (°C)	Simulation temperature(°C)	Error(%)
(14.41,16.43,0)	120.73	120.81	-0.12
(20.34,16.43,0)	123.80	123.88	-0.11
(29.38,21.03,0)	131.67	131.81	-0.18
(35.65,21.03,0)	129.29	129.43	-0.18

and the table demonstrate an excellent agreement between the model and simulation. The percentage error for a particular point is calculated by the following definition:

$$\text{Error } (\%) = \frac{\theta_M - \theta_S}{\theta_S - 52.635} \tag{4.1}$$

where θ_M, θ_S and 52.635 are model, simulation and ambient temperature respectively (in °C). It is important to highlight that $N_m = N_n = 200$ is used for the above analysis.

4.2 Convergence analysis of the steady-state thermal model

If a function meets the following conditions called 'Dirichlet's Conditions', it converges at every point of continuity. These conditions are sufficient for convergence. (For details, readers are referred to [80]).

a) The function is piecewise regular (i.e. the function is analytic and single-valued in every point).

b) It has a finite number of discontinuities.

c) It has a finite number of extrema.

The expressions of temperatures derived in the previous chapter meet all these requirements. Therefore, these converge at every point as there is no discontinuity. Theoretically, the Fourier series representation of a function contains an infinite number of terms. However, in practice it is not possible

to use infinite number of terms. Therefore, a truncated form of the Fourier series is used. Figure 4.4 and 4.5 demonstrate the convergence of the steady-state thermal model for X = 20.152 mm and Y = 22.282 mm respectively.

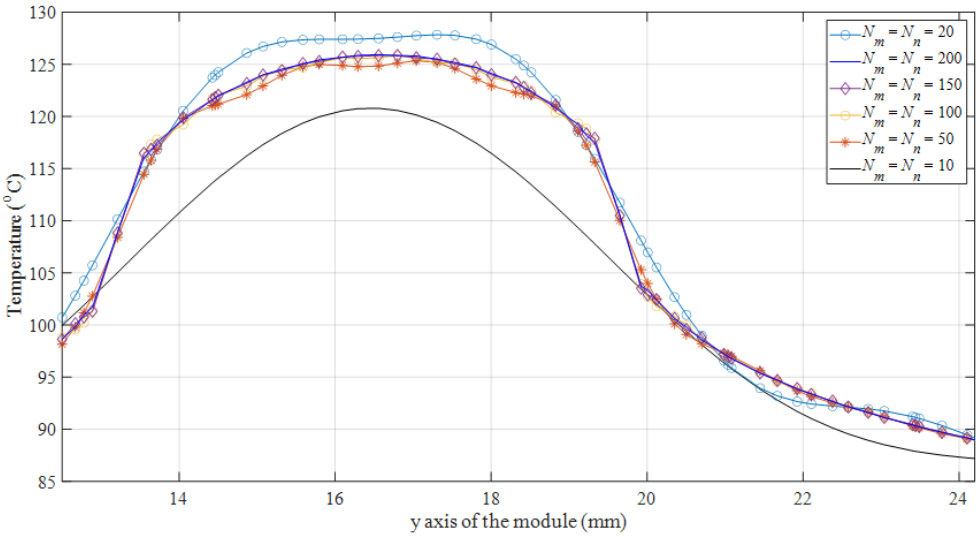


Figure 4.4: Comparison between the model and simulation along the line X = 20.152 (mm)

These figures show that convergence is achieved when N_m and N_n are both atleast 150. Before that, oscillation is observed due to the presence of the sinusoidal terms in the expression of the temperature.

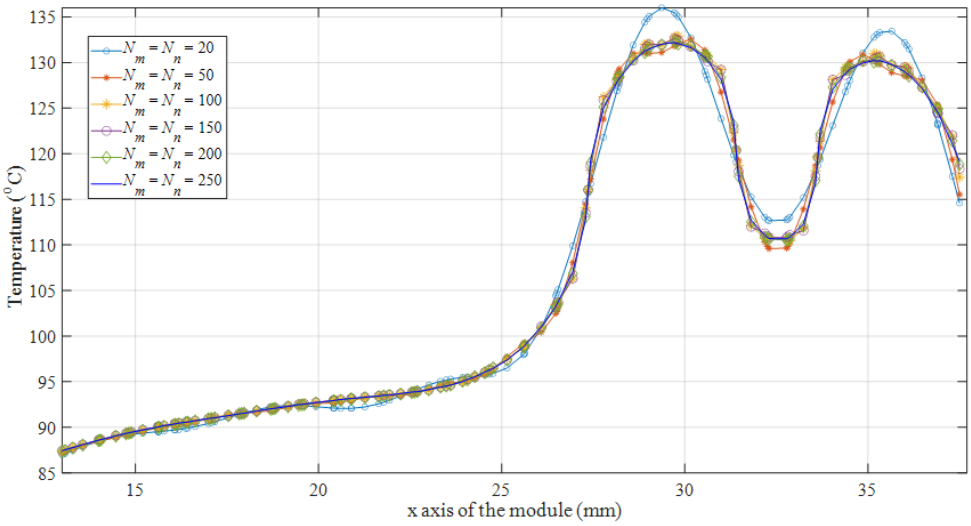


Figure 4.5: Comparison between the model and simulation along the line Y = 22.282 (mm)

4.3 Application of the thermal model of an N-layer structure to a power module

The top view of the power module studied in this work (Microsemi Power Module Products, part no. APTMC120AM20CT1NG) is shown in Figure 4.6. Relevant dimensions and material properties are given in Table 4.3.

4.3.1 The RNLF method and the simulation of different structures

The RNLF method assumes that all layers occupy the full extent of the rectangular surface. However, in real power modules, the top copper layer of

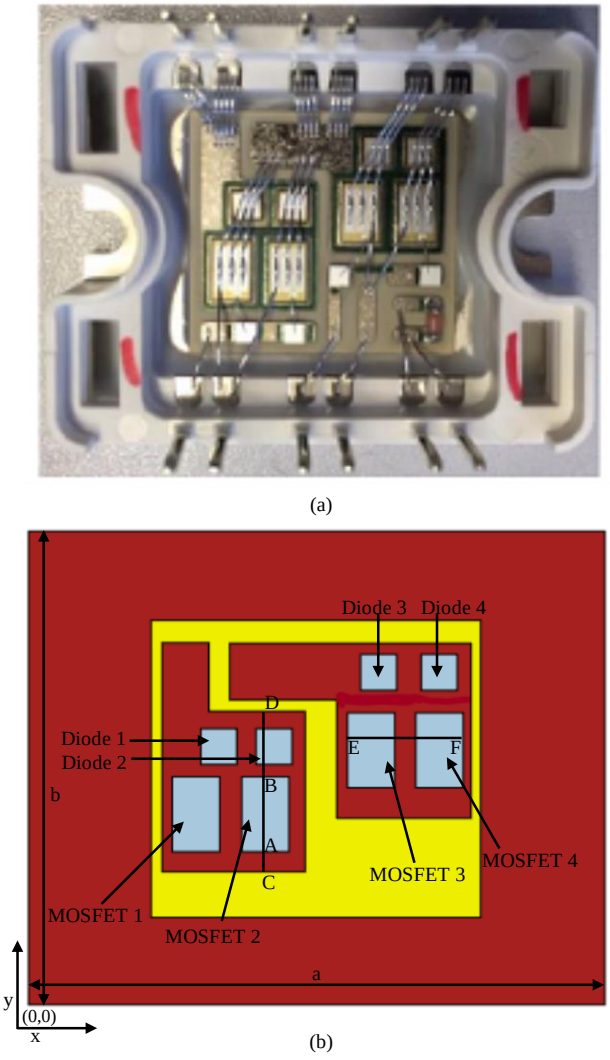


Figure 4.6: (a) Top view of a commercial power module (courtesy of Microsemi Power Module Products), (b) Equivalent schematic view showing the devices (heat sources) and the lines AB, CD and EF.

the DBC (Direct Bonded Copper) stack is patterned and the substrate is smaller than the baseplate. Therefore, in order to justify the application of

Table 4.3: Material assembly and the relevant properties of the SiC power module (courtesy of Microsemi Power Module Products)

Layers (Figure 4.6)	Material	Size (mm^2)	Thickness (mm)	k (W/(mK))
1	SiC MOSFET	4.04×6.44	0.18	370
	SiC Diode	3.08×3.08	0.377	370
2	MOSFET solder	4.04×6.44	0.09	30
	Diode solder	3.08×3.08	0.09	30
3	Copper	28.2×25.54	0.3	390
4	Si_3N_4 (Substrate)	28.2×25.54	0.32	90
5	Copper	28.2×25.54	0.3	390
6	Solder	28.2×25.54	0.2	30
7	Copper (Baseplate)	49.46×40.8	2.5	390
8	Thermal grease	49.46×40.8	0.10	2.5

the RNLF method to the modelling of power modules, it must be argued that the patterning and the limited extent of the DBC stack does not greatly affect the temperature field, particularly in the key regions around the die. The solder layer and the DBC stack are very thin compared to their lengths and widths. Hence, it is reasonable to assume that heat-spreading in these layers occurs only near the edges of the dies and does not extend far beyond them. To verify this assumption, a number of COMSOL FEM models are used to investigate the effects of the simplifications required to reduce the complex power module to a simpler structure which can be solved using the RNLF method. The simplified structures are classified based on three features: copper layer type, dissipation type (area or volume) and solder layer type. *Area dissipation* means there is no die and all the heat enters the

corresponding chip area perpendicularly to the surface. *Volume dissipation* means the presence of the die with internal heat generation. The simplified structures are described in Table 4.4. In this work, a relatively thick heat spreader of Aluminium alloy is used to create an isothermal surface as the boundary condition at the bottom of the heat spreader (thick blue block in Figures 4.7-4.11) which will be discussed in the next chapter. It is important to highlight that the PVU structure most closely matches with the structure of the power module under consideration in this work. From that, the subsequent structures are obtained by step-by-step simplification. In this process, the CAC is the simplest structure. Additionally, the assumptions

Table 4.4: Different structures for simulation

Copper	Dissipation	Solder	Structure-acronyms	Fig. no.
Patterned	Volume	Under the die area only	PVU	4.7
Patterned	Area	Under the die area only	PAU	4.8
Continuous	Volume	Under the die area only	CVU	4.9
Continuous	Area	Under the die area only	CAU	4.10
Continuous	Area	Thermal Resistance	CAR	4.10
Continuous	Area	Continuous	CAC	4.11

that the sides and top surface are adiabatic are reasonable because a conventional power module is encapsulated by plastic and the gap between the top surface (where the dies are situated) and plastic casing is filled by silicon gel for improved electrical insulation. The assumption of perfect thermal contact between different layers is also reasonable as modern power semicon-

ductor modules are very much well-constructed. The thermal grease layer is modelled as a layer of uniform thickness.

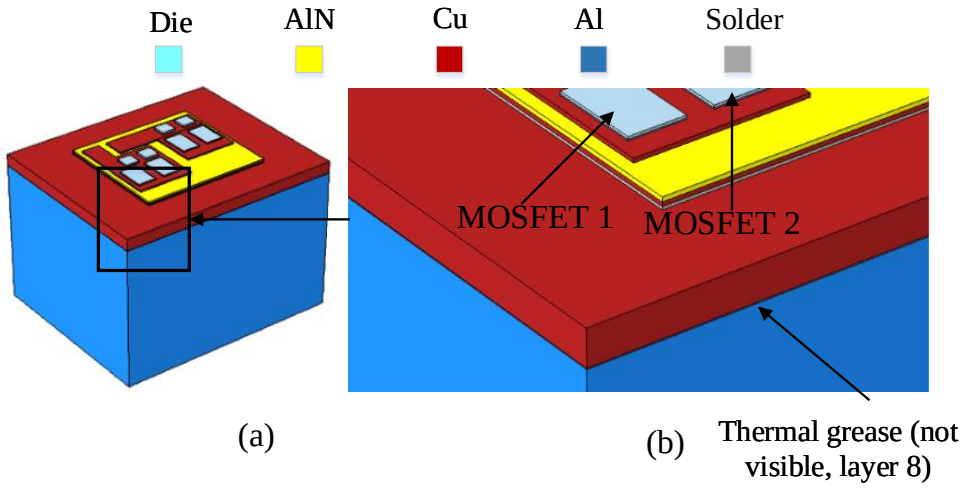


Figure 4.7: (a) Three dimensional view of the PVU (presence of die), (b) Magnified view of the upper part of the structure.

4.3.2 Simulation results and relevant discussion

The temperatures of the MOSFET devices are of particular interest because these typically represent the hottest, mostly thermally sensitive devices. Therefore, in Figure 4.13 the temperature profile along the line AB in Figure 4.12 (x = 20.152 mm) which cuts through MOSFET 2 over the solder layer is selected for detailed examination. It should be noted that the side view of AB for the COMSOL FEM (PVU) model is different to the side view of AB in the RNLF method (see Figure 4.12). Figure 4.14 illustrates

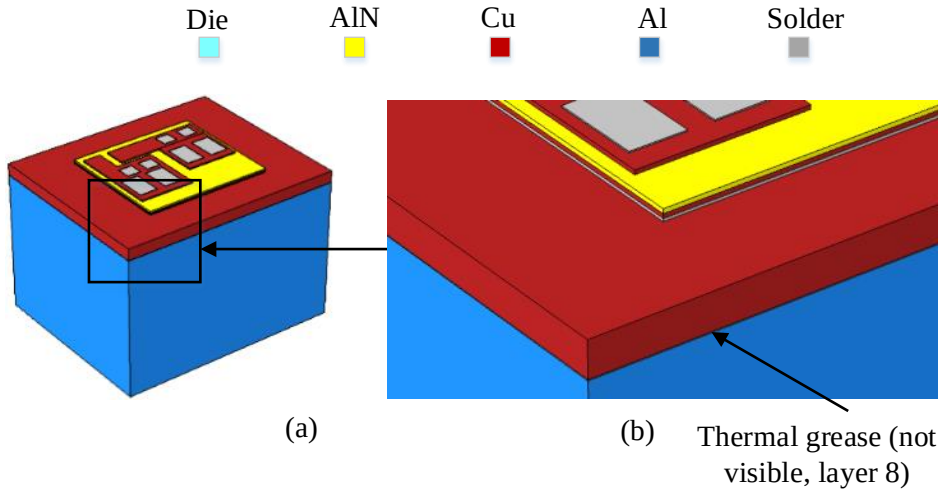


Figure 4.8: (a) Three dimensional view of the PAU (No die, only solder), (b) Magnified view of the upper part of the structure.

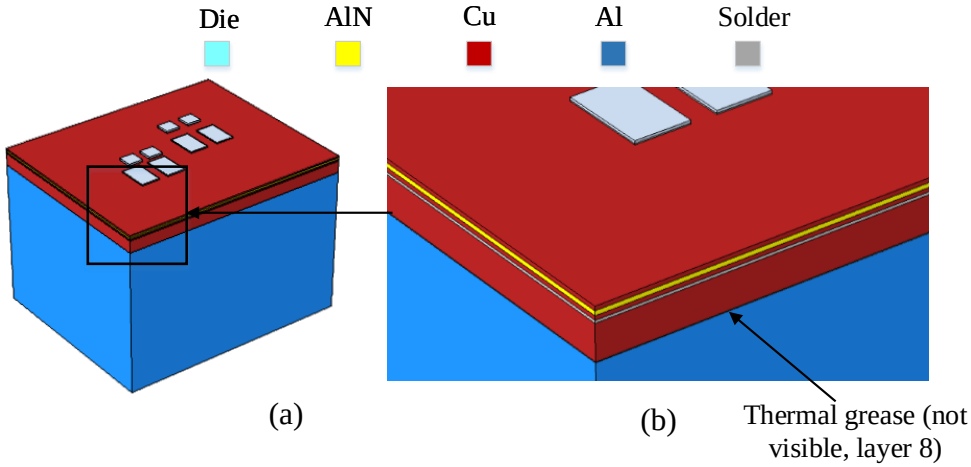


Figure 4.9: (a) Three dimensional view of the CVU (presence of die), (b) Magnified view of the upper part of the structure.

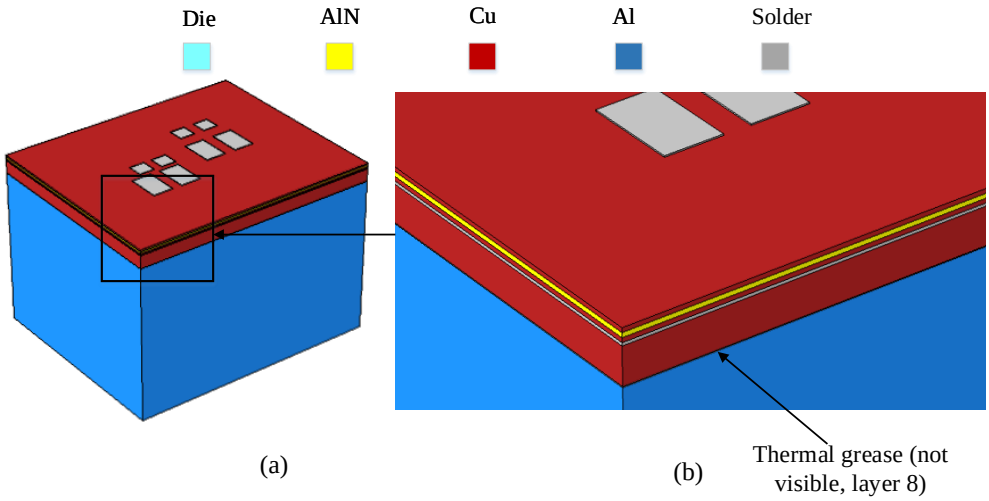


Figure 4.10: (a) Three dimensional view of both the CAU (No die, only solder) and CAR, (b) Magnified view of the upper part of the structure.

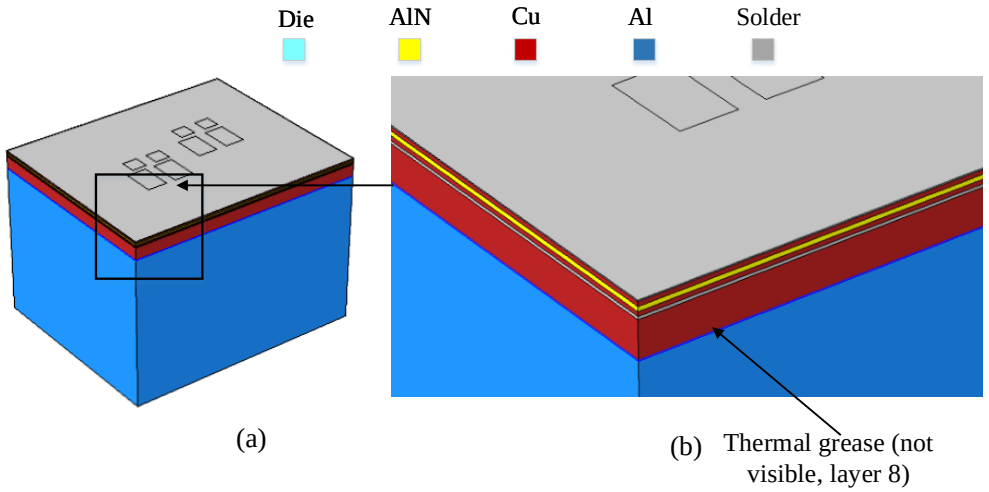


Figure 4.11: (a) 3D view of the CAC, (b) Magnified view of the upper part of the structure.

the differences between the temperature profiles of different structures at the midpoint of AB. All temperatures are calculated on the top surface of the solder (just underneath the die). This closely reflects the die temperature because the temperature within the die is almost constant due to the high thermal conductivity of SiC. Figures 4.7-4.9 show the relevant diagrams of

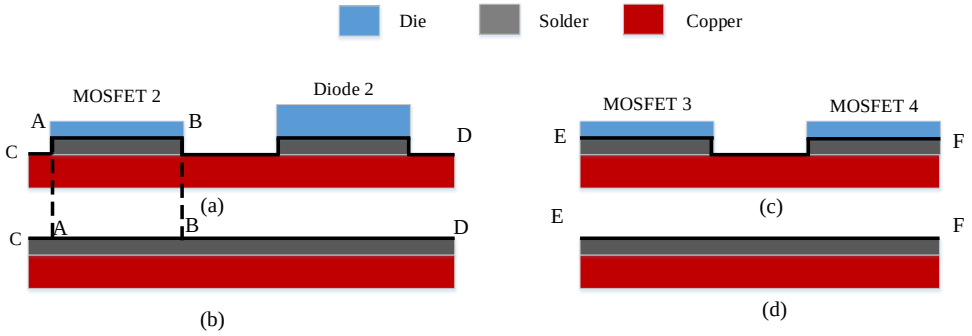


Figure 4.12: (a) Side views of the lines AB and CD corresponding to COMSOL FEM (PVU) model, (b) Side views of lines AB and CD corresponding to the RNLF method, (c) Side view of line EF corresponding to COMSOL FEM (PVU) model, (d) Side view of line EF corresponding to the RNLF method.

the PVU, PAU and the CVU structures respectively. Figure 4.10 shows both the CAU and the CAR structures. Figure 4.11 shows the CAC structure which corresponds to the RNFL method.

The PAU structure demonstrates higher temperature compared to the PVU structure except at the edges of the dies. At the edges, the PVU structure shows lower temperature gradient compared to what the PAU structure shows. The only difference between the PAU and the PVU structures is the presence of dies. Therefore, it can be concluded that in the structure corre-

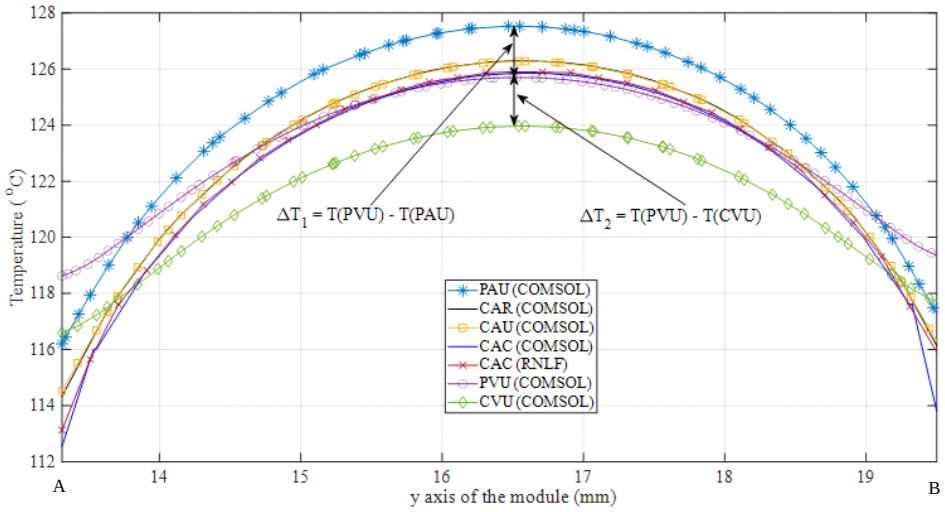


Figure 4.13: Comparison of the simulation results for different structures along the line AB ($N_m = N_n = 200$ for CAC (RNLF)).

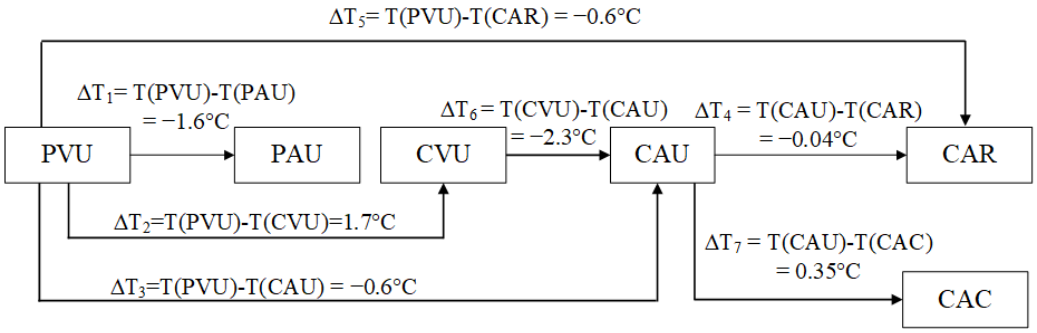


Figure 4.14: Temperature differences between different structures at the midpoint of line AB ($N_m = N_n = 200$ for CAC RNLF).

sponding to the PVU, there is some heat spreading within the die such that all the heat flux is not normal on the top surface of the solder under the die. However, the effect may be considered relatively weak.

The PVU structure gives higher temperature compared to the CVU struc-

ture because of the small effect of the heat spreading in the continuous copper layer in the latter. It is observed that these structures show almost a constant temperature difference (approximately 2°C) between them which suggests that the patterning of Copper decreases the effective thermal conductivity of the layer thereby increasing the thermal resistivity. The same phenomenon is observed between the PAU and CAU structures.

In the CAR structure, the temperature profile is obtained by adding a constant temperature rise (corresponding to a simple thermal resistance model of the solder layer) to the temperature distribution of the relevant area of copper surface. This is valid because the solder layer is very thin and its thermal conductivity is low, so there is little thermal spreading and it can be well approximated as a thermal resistance. It is observed that there is a very close match between the temperature profiles of the CAU and the CAR structures confirming this assumption.

The temperature-profile given by the PVU structure matches very closely with those of the CAU structure, the CAR structure and the CAC structures in the middle region of the die. However, at the both ends of the region of our interest, the CAU and the CAR structures differ from the PVU structure by approximately 4.1°C and the shape of temperature-profile of the PVU structure is different to those of the CAR and the CAU structures. The fact that all the structures show similar temperature-distribution in the middle region of the die suggests that the distribution of heat flux is very similar here.

An important implication of the RNLF method is that corresponding stress gradient across the die is higher compared to that obtained from the FEM because there is a positive correlation between the thermal expansion (on which resulting stress is dependant) of a material and its temperature and the temperature gradient in that region predicted by the RNLF method is higher.

4.3.3 Comparison of the computational time

The time required to calculate the steady-state temperature of the midpoint of MOSFET 3 by the RNLF method is approximately 0.5 s by using a relatively unoptimised MATLAB script on a standard laptop (Intel Core i5 7200U, 8GB RAM). On the other hand, it takes approximately 33 s to compute the temperature of the same point by COMSOL Multiphysics on the same machine.

4.4 Some applications of the RNLF method

The RNLF method can be used for calculating thermal spreading resistance and hence, total thermal resistance. Moreover, it can be used to understand the heat spreading in different layers. These are explained here.

4.4.1 Thermal spreading resistance

The thermal spreading resistance may be computed using the mean temperature-rise of the heat source. From [81],

$$\begin{aligned}
&\theta_{1,s}(x,y,z) = A_{10} + B_{10}z \\
&+ \sum_{m=1}^{\infty} \cos\left(\frac{m\pi}{a}x\right)[A_{1m}\cosh\left(\frac{n\pi}{a}z\right) + B_{1m}\sinh\left(\frac{m\pi}{a}z\right)] \\
&+ \sum_{n=1}^{\infty} \cos\left(\frac{n\pi}{b}y)[A_{1n}\cosh\left(\frac{n\pi}{b}z\right) + B_{1n}\sinh\left(\frac{n\pi}{b}z\right)\right] \\
&+ \sum_{m=1}^{\infty}\sum_{n=1}^{\infty} \cos\left(\frac{m\pi}{a}x\right)\cos(\frac{n\pi}{b}y\Big)[A_{1mn}\cosh(\beta_{mn}z) \\
&+ B_{1\bar{m}\bar{n}}\sinh(\beta_{mn}z)],
\end{aligned} \tag{4.2}$$

The average temperature-rise of the heat source can be obtained by integrating (4.2) over the heat source area. Executing the necessary mathematical operations leads to the following expression for the average temperature-rise:

$$\begin{aligned}
&\bar{\theta}_1(x,y,z) = A_{10} + 2\sum_{m=1}^{\infty} A_{1m}\frac{\cos(\lambda_m X_c)\sin(\frac{1}{2}\lambda_{\bar{m}}c)}{\lambda_{\bar{m}}c} + \\
&+ 2\sum_{\bar{n}=1}^{\infty} A_{1\bar{n}}\frac{\cos(\delta_{\bar{n}}Y_c)\sin(\frac{1}{2}\delta_{\bar{n}}d)}{\delta_{\bar{n}}d} + 4\sum_{\bar{m}=1}^{\infty}\sum_{\bar{n}=1}^{\infty} A_{1\bar{m}\bar{n}}\frac{\cos(\delta_{\bar{n}}Y_c)\sin(\frac{1}{2}\delta_{\bar{n}}d)\cos(\lambda_{\bar{m}}X_c)\sin(\frac{1}{2}\lambda_{\bar{m}}c)}{\delta_{\bar{n}}\lambda_{\bar{m}}dc}
\end{aligned} \tag{4.3}$$

where

$$\lambda_{\bar{m}} = \frac{\bar{m}\pi}{a}, \delta_{\bar{n}} = \frac{\bar{n}\pi}{b}$$

It is important to highlight that (4.3) is similar to the expression of average temperature-rise or thermal resistance derived in [49]. Now, thermal spreading resistance, R_{sp} is calculated as

$$R_T = \frac{\bar{\theta}_{1,s}}{Q} = R_{1D} + R_{sp} \tag{4.4}$$

where R_{1D} is the one-dimensional thermal resistance. By inspection, it can be said that series terms in (4.3) are the thermal spreading resistance and $R_{1D} = A_{10}$ is the one-dimensional thermal resistance which is equal to 0.01075 K/W for all MOSFETs. The spreading thermal resistances associated with each MOSFET are given in Table 4.5. The spreading thermal

Table 4.5: One dimensional and spreading thermal resistances of MOSFETs for the SiC power module

MOSFET	X_c (mm)	Y_c (mm)	R_{sp} (K/W)
1	14.41	16.43	0.4074
2	20.34	16.43	0.4074
3	29.38	21.03	0.4076
4	35.65	21.03	0.4076
example	45.00	37.00	0.4524

resistances of MOSFETs 1-4 are very similar because they are all placed near the centre of the module and so share very similar thermal paths to ambient. An example MOSFET placed near the corner of the module exhibits a significantly larger spreading thermal resistance. Note that MOSFETs 3 and 4

exhibit higher temperatures because they dissipate more power compared to MOSFETs 1 and 2, not because they have a higher spreading resistance.

4.4.2 Temperature distribution in different layers

To determine the temperature distribution in a particular layer, one needs to know the relevant coefficients. Temperature distribution on the planes situated in the middle of the second third, fourth and fifth layers of the rectangular N-layer structure under consideration is given in Figures 4.15, 4.16, 4.17, 4.18 4.19 and 4.20 respectively. By inspection, it can be concluded that heat spreading occurs around the edges of dies in the first five layers. Heat spreading is more prominent in the sixth layer.

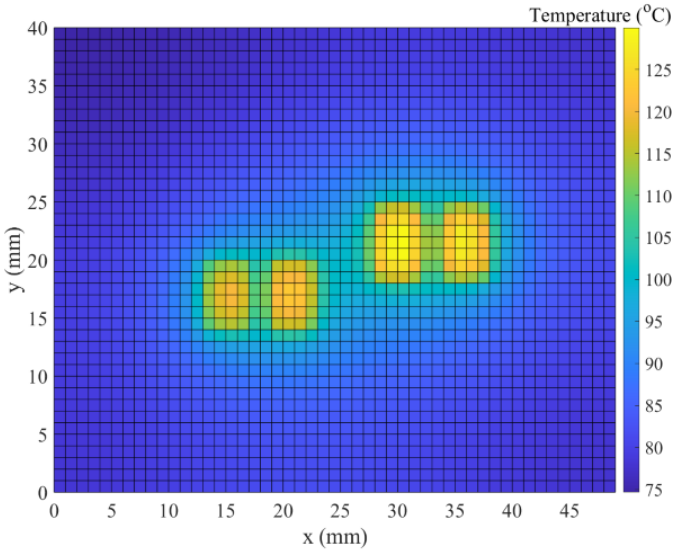


Figure 4.15: Temperature distribution in the middle of the second layer (Solder) of the rectangular N-layer structure

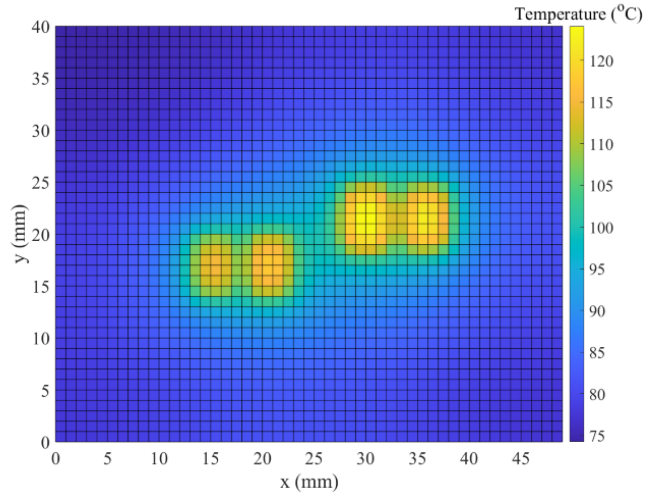


Figure 4.16: Temperature distribution in the middle of the second layer (Solder) of the rectangular N-layer structure

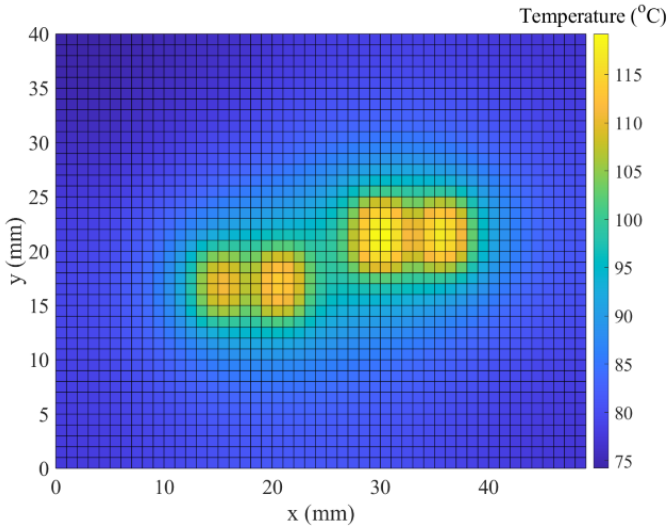


Figure 4.17: Temperature distribution in middle of the third layer (Copper) of the rectangular N-layer structure

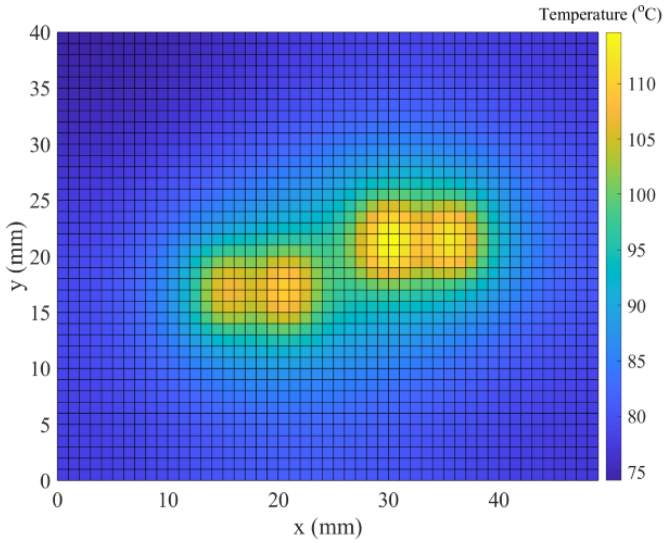


Figure 4.18: Temperature distribution in middle of the fourth layer of the rectangular N-layer structure

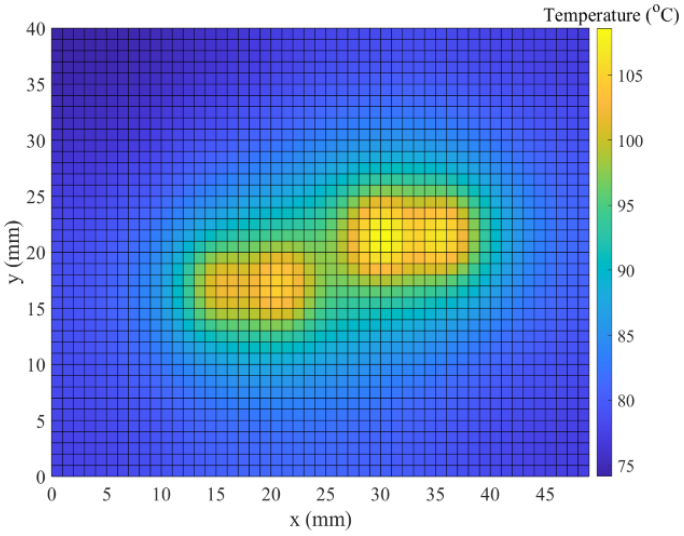


Figure 4.19: Temperature distribution in middle of the fifth layer of the rectangular N-layer structure

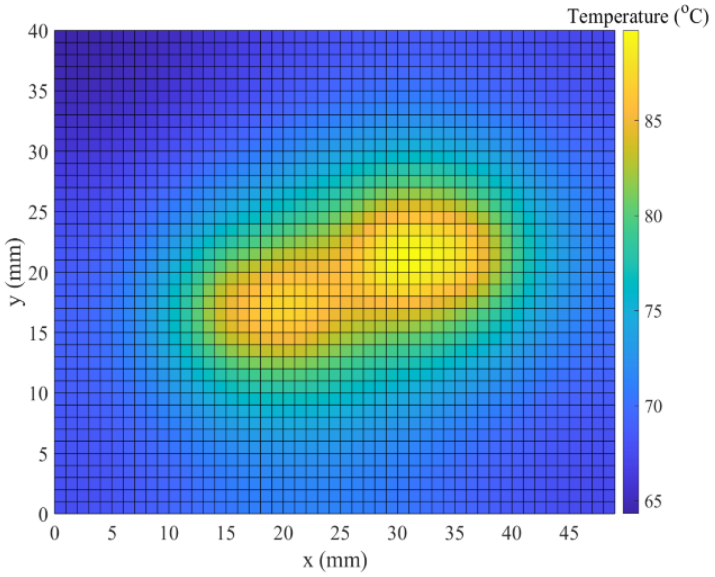


Figure 4.20: Temperature distribution in middle of the fifth layer of the rectangular N-layer structure

4.5 Effect of the patterned Copper layer on the temperature distribution

It is worthwhile to investigate the effect of the patterned Copper layer on the temperature distribution because it may provide us an insight into the limitations of the RNLF method. To that end, thickness of the corresponding Copper layers in the PVU and CAC structures are increased from 0.3 mm to 1.5 mm. The temperature of the midpoint of line AB is considered for the comparison between both cases. From the Table 4.6, it is observed that temperature decreases for both structures with the increasing value of the thickness of the first Copper layer. However, temperature decreases more

Table 4.6: Comparison for different values of thickness of the patterned copper layer

Thickness (mm)	Temperature (°C)-PVU	Temperature (°C)-CAC	Difference (%)
0.3	123.02	123.01	0.01
0.6	121.17	119.32	2.70
0.9	120.95	116.95	5.85
1.2	119.84	115.32	6.72
1.5	119.71	114.16	8.27

rapidly in the CAC structure because heat spreading is more prominent in the continuous Copper layer than what it is in the patterned Copper layer in the PVU structure. It implies that the CAC structure provides satisfactory results as long as the heat spreading within the DBC stack is not that great. However, it is worthwhile to mention that the thickness of the Copper layers in the DBC stack is typically around 0.3 mm implying that our assumption regarding heat spreading in the DBC stack is valid for most of the practical applications. It is important to mention that the difference in this table is defined by

$$\text{Difference} = \frac{T_{\text{PVU}} - T_{\text{CAC}}}{T_{\text{PVU}} - 52.635} \tag{4.5}$$

where T_{PVU} and T_{CAC} are temperatures obtained from the PVU and CAC structures respectively.

4.6 Validation and convergence of the transient thermal model or TRNLF method by COMSOL Multiphysics

The transient thermal model can be denoted as "Transient Rectangular N-layer Fourier" or TRNLF method. For the model and simulation, the heat dissipation (step input) in MOSFETs M1-4 are 63.8 W, 63.8 W, 76.9 W and 76.9 W respectively. Figure 4.21 shows the comparison of the temperature response for the midpoint of MOSFET 3 (point B) predicted by COMSOL Multiphysics and TRNLF method and the convergence of the latter at $t = 60$ ms. This time point is chosen as it is in the sub-transient region when there is relatively high-frequency spatial and temporal temperature behaviour, which will be evident in higher-order Fourier terms. The error at any point in time is defined by the following equation:

$$\text{error}(t) = \frac{T_{\text{S}}(t) - T_{\text{M}}(t)}{T_{\text{S}}(t) - T_{\text{amb}}} \tag{4.6}$$

where $T_{\text{S}}(t)$ is the simulation temperature, $T_{\text{M}}(t)$ is the model temperature and T_{amb} is the ambient temperature.

The figure shows the convergence of temperature for different values of $\bar{l}$ (number of eigenvalues associated with the eigenfunctions in z direction). It is observed that the effect of $\bar{l}$ on the convergence of the temperature is relatively weak compared to that of $\bar{m}$ or $\bar{n}$ ($\bar{l} > 2$ and $\bar{m} = \bar{n} > 10$ gives

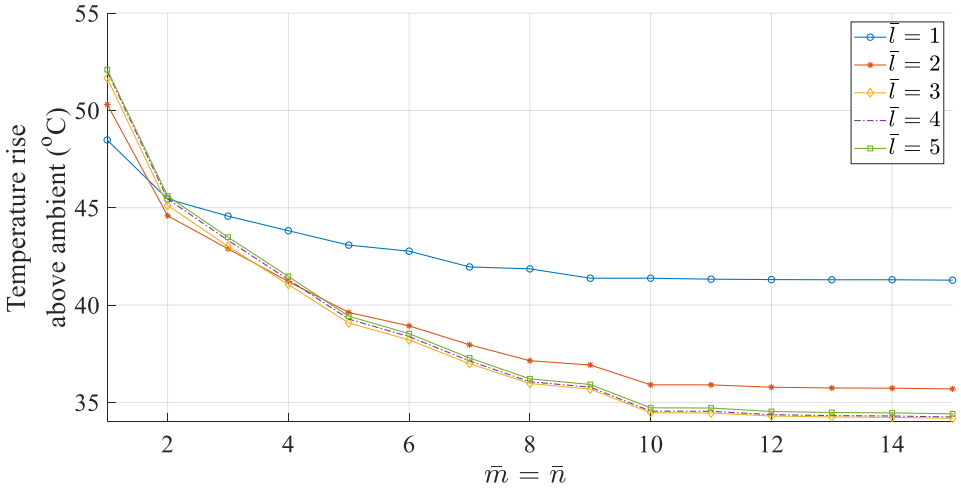


Figure 4.21: Convergence of the temperature of the midpoint of MOSFET 3 at $t = 60$ ms

good convergence). In $A_{\bar{m}0\bar{l}}$, $A_{0\bar{n}\bar{l}}$ and $A_{\bar{m}\bar{l}\bar{n}}$, $\bar{m}$ and $\bar{n}$ are present explicitly in the arguments of sine and cosine hyperbolic functions. These functions are unbounded and increase exponentially with the increment of arguments. On the other hand, $\bar{l}$ only affects the sinusoidal terms of the eigenfunctions in z direction which are bounded. Therefore, the effect of high-order terms corresponding to $\bar{m}$ or $\bar{n}$ is more pronounced than that of $\bar{l}$. The similar trend thing is observed for other time instances. Based on this observation, it can be concluded that a low value of $\bar{l}$ is acceptable, which can be exploited to reduce computational effort of the TRNLF method.

4.7 Application of the TRNLF method for the transient thermal modelling of a power module

As discussed previously, the CAC structure gives good results because the patterning of the Copper and the limited extent of the DBC stack does not greatly affect the temperature field, particularly in the important regions around the die. Therefore, only this structure is considered in this section to compare with the PVU structure. Table 4.7 shows densities and specific heat capacities of the different materials used in the power module.

Table 4.7: Material properties for the SiC power module (part no. APTMC120AM20CT1NG, Courtesy of Microsemi Power Module Products)

Materials	Density (ρ) (kg/m^3)	Specific heat capacity (c) (J/(kgK))	Thermal diffusivity (α) (cm^2/s)
SiC	3216	690	1.67
Si_3N_4	3100	700	0.415
Solder (die attach)	10700	150	0.187
Copper	8960	385	1.13
Solder (DBC attach)	7400	240	0.169
Thermal grease	2500	3000	0.00330
Aluminium alloy	2700	900	0.741

4.7.1 Simulation results and discussion

Figures 4.22 and 4.23 show the comparison of the temperature response for the midpoints of MOSFET M1 and M3 (shown in Figure 4.6) predicted by COMSOL Multiphysics and TRNLF method and the convergence of the latter. The error at any point in time is defined by Eq. (4.6). These figures

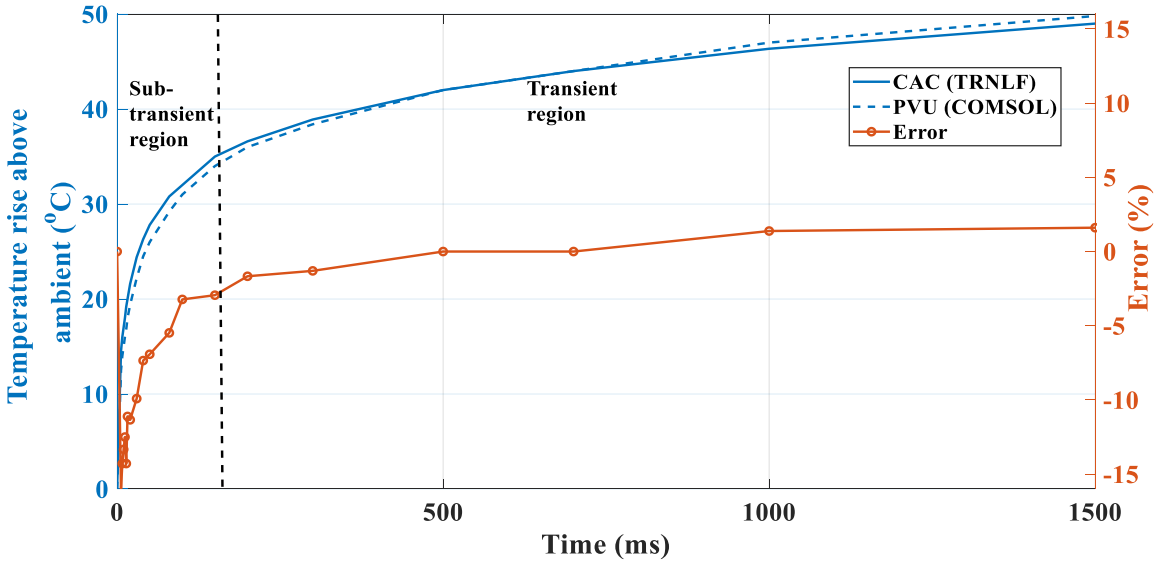


Figure 4.22: Comparison between the PVU and the CAC for point the midpoint of MOSFET 1

can be roughly divided into two regions. The rate of temperature rise in the sub-transient region is significantly higher than that in the transient region. The TRLNF model predicts higher temperature than that given by the PVU structure FEM simulation in the sub-transient region. This is because, in the CAC model, heat flux is constant on the top surface at all times. In

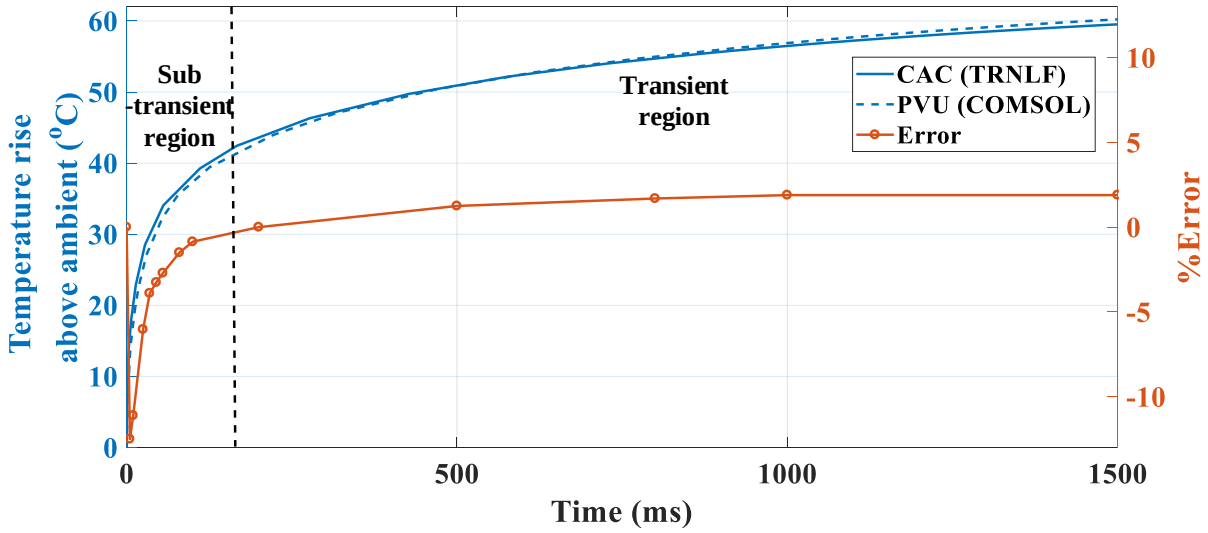


Figure 4.23: Comparison between the PVU and the CAC for point the mid-point of MOSFET 3

contrast, in the PVU model, the finite thermal diffusivity of the die material is included and therefore it takes a short period for the heat flux at the top of the solder layer to reach a constant value. This is a small effect as the die is physically small and the thermal diffusivity of Silicon Carbide is relatively high. When the die approaches thermal equilibrium the PVU model gives a slightly higher temperature than that suggested by the CAC model. This is because the temperature measurement is taken on the top of the die in the PVU model, rather than on the top of the solder as in the CAC model.

An important implication of the TRNLF method is that for the short time interval (in the sub-transient region) it predicts higher temperature rise than that predicted by the FEM method. As there is a positive correlation between stress and temperature rise, the TRNLF method will predict higher

stress and hence lower lifetime for the devices.

4.7.2 Comparison of the computational time

The total computational effort required by the TRNLF method can be separated into three parts: time to extract eigenvalues, time to calculate the coefficients of the eigenfunctions and time to calculate the temperature response. For the examples used in this paper, using a relatively unoptimised MATLAB script running on a standard laptop (Intel Core i5 7200U, 8GB RAM), the time taken to extract 25 eigenvalues is approximately 3.5 minutes, time taken to calculate the coefficients is approximately 40 seconds and time taken to calculate the temperature response is 2-3 seconds. Therefore, the total time taken to compute the temperature response of a particular point at a particular instant is dominated by calculation of eigenvalues and the coefficients of eigenfunctions. However, the eigenvalues and the coefficients of eigenfunctions only need to be evaluated once for a particular geometry and material combination (see Fig. 3.5). Once this is done, the temperature response to a step input (and by implication, an arbitrary waveshape) can be calculated quickly. More importantly, the determination of eigenvalues and coefficients only depend on thickness and material properties of each layer, not on the length and width or the position of the chip. Therefore, TRNLF method will be useful for the thermal optimisation problem of the applications where the thickness and material of each layer is fixed. In contrast, a simulation in COMSOL Multiphysics cannot directly calculate the tempera-

ture response at a particular space/time point. To calculate the temperature of a particular point at a particular time, a FEM system must solve the whole system for previous instants. As a comparison, on the same machine, COMSOL Multiphysics takes approximately 10-12 minutes to calculate the temperature field at $t = 3$s using the default settings.

Chapter 5

Experimental verification of the steady-state and transient modelling

In this chapter, experimental set-up to validate the thermal models using a SiC module (part no. APTMC120AM20CT1NG) is described and relevant results are discussed.

5.1 Experimental set-up

The experimental set-up is essentially the same for validating steady-state and transient thermal models. This set-up is divided into two parts: mechanical and electrical. These are discussed in the following sections.

5.1.1 Mechanical set-up

A liquid-cooling bath (not shown in the figure) circulates water at a specified temperature through the pipes connected with the heatsink. It circulates water through the pipes connected with the heatsink (part number is 416501U00000G, manufacturer is Aavid Thermalloy). Appropriate compression fittings are used to connect the pipes with the heatsink and the cooling bath. The heatsink is kept vertical with the help of two retort clamps. The bases of the clamps are kept fixed by G-clamps. The purpose of this arrangement is to facilitate the image-capturing by an IR camera supported by a tripod. Figure 5.1 shows this arrangement.

A key requirement for the experiment is to make an isothermal surface under the copper baseplate as a boundary condition. It is chosen because it makes our thermal models convenient to apply. An extremely high performance liquid-cooled heatsink attached directly with a power module may achieve that goal but this kind of heatsink is very expensive. Therefore, a heat diffuser made of Aluminium alloy is used in this experiment to facilitate the heat spreading and create an isothermal surface within that diffuser. This fact can be demonstrated by simulation with COMSOL Multiphysics.

The effect of the diffuser is demonstrated in Figure 5.2. A K-type thermocouple is used to measure the temperature of the midpoint of the plane shown in this figure. It gives a reading of 52.6°C which is close to the simulation temperature of 51.4°C. Therefore, in this work 52.6°C is considered the temperature of the isothermal plane.

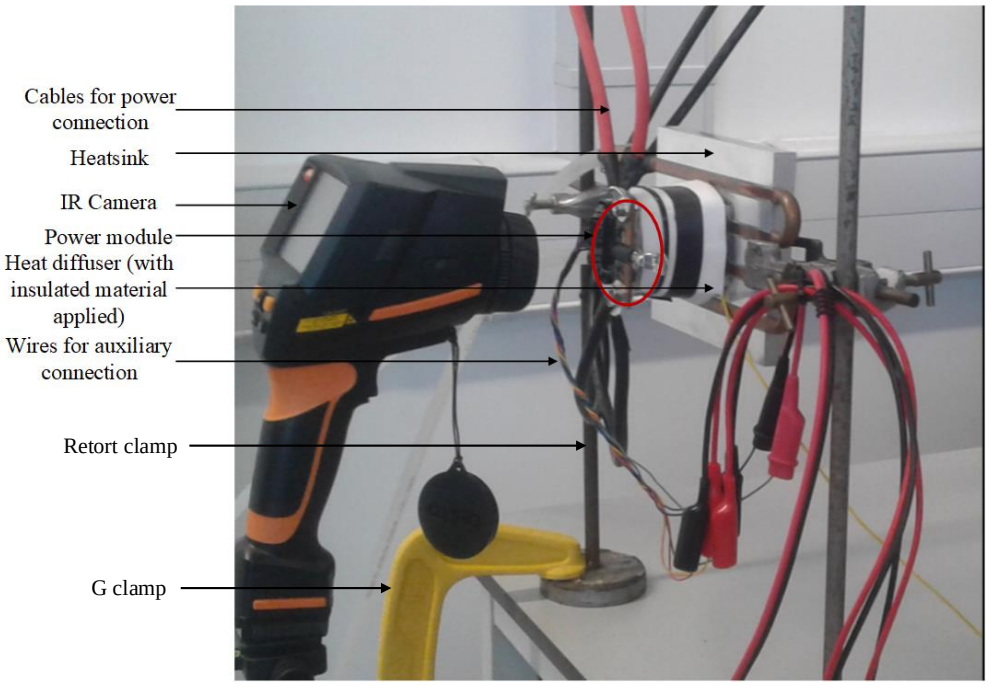


Figure 5.1: Experimental set-up showing the positioning of the IR camera and the power module.

Rather than modelling the cooling tubes embedded within the heatsink, two inlets and two outlets are considered on COMSOL Multiphysics. These are positioned alternately on the xz surface of the heatsink. Water is used as liquid and flow rate is 2 GPM (Gallon per Minute). Therefore, the flow of water is considered turbulent for high Reynolds number. The inlet temperature of water is 22°C. The heat diffuser is wrapped by insulating foam so that heat cannot be transferred to the ambient. It has been done to create the boundary condition of our thermal model. It should be mentioned that thermal grease is applied on the bottom surface of the heat diffuser to fill up

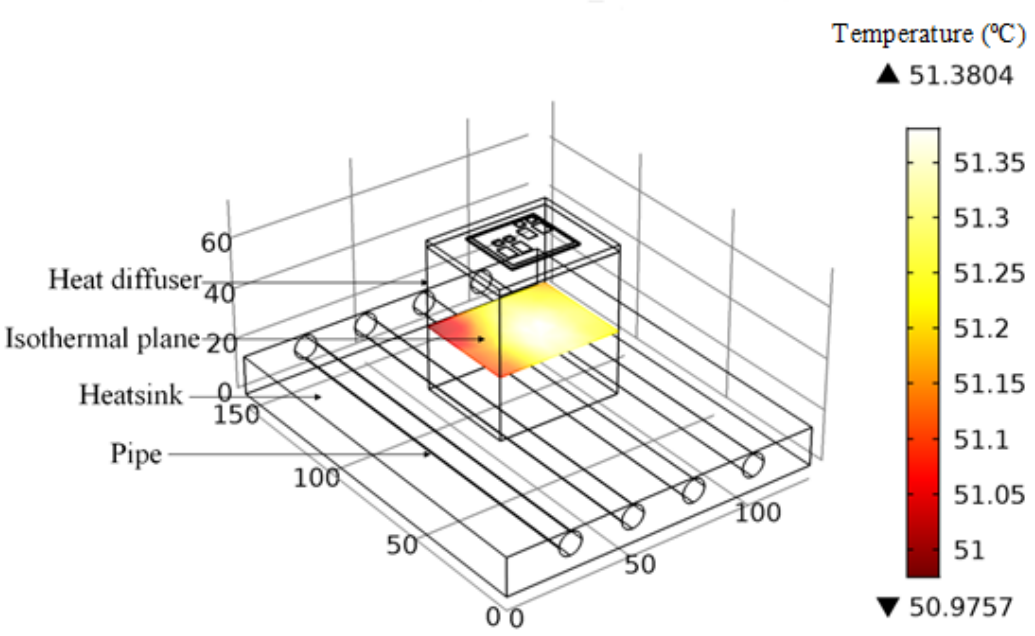


Figure 5.2: Model in COMSOL Multiphysics showing the isothermal plane within the heat diffuser (note the low temperature difference across the plane).

the gaps created due to the roughness of the surface.

5.1.2 Preparation of the module

Power modules typically use a plastic housing with the void between the dies and housing filled by silicone gel [6] for improved electrical insulation. However, as the silicone gel is opaque to infrared radiation, in order to allow the capture of thermal images of the top surface of the module the sample module used in this work was provided by the manufacturer without any silicon gel (see Fig. 5.10). Furthermore, the surface of the module is replete

with shiny copper traces, semiconductor devices and wirebonds with the emissivity much lower than 1, which would prevent the IR camera from capturing accurate data. Therefore, black paint is sprayed a number of times over the top surface of the power module in order to raise the emissivity to close to 1. The value of emissivity setting used in this work is 0.98.

5.1.3 Electrical set-up

Figure 5.3 shows the circuit diagram of the electrical set-up and important electrical connections. A DC power supply is used as a current source. Two different voltage sources are used to turn on the MOSFETs. These are held on continuously using a constant $V_{gs} = 20$ V.

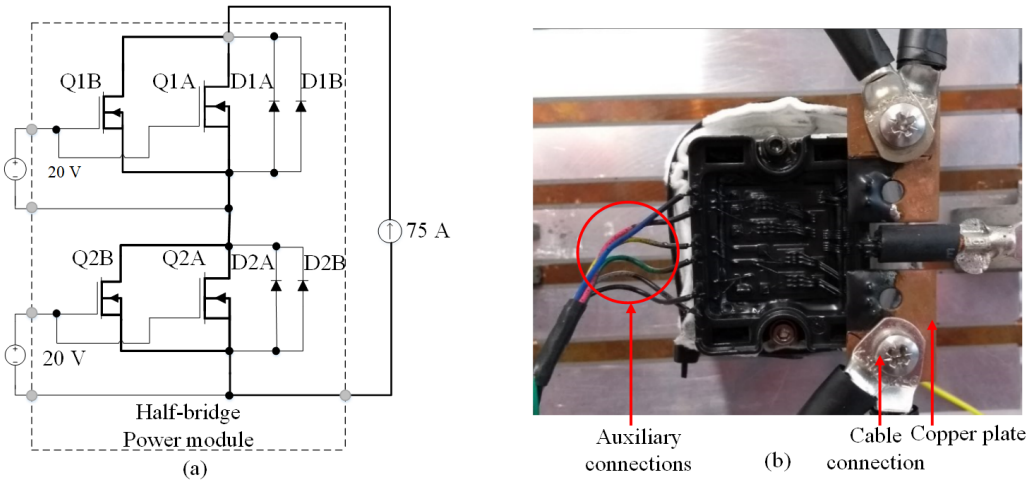


Figure 5.3: (a) Schematic diagram of the circuit of the experiment (current path shown in bold), (b) Front view of the module with the matt black paint applied.

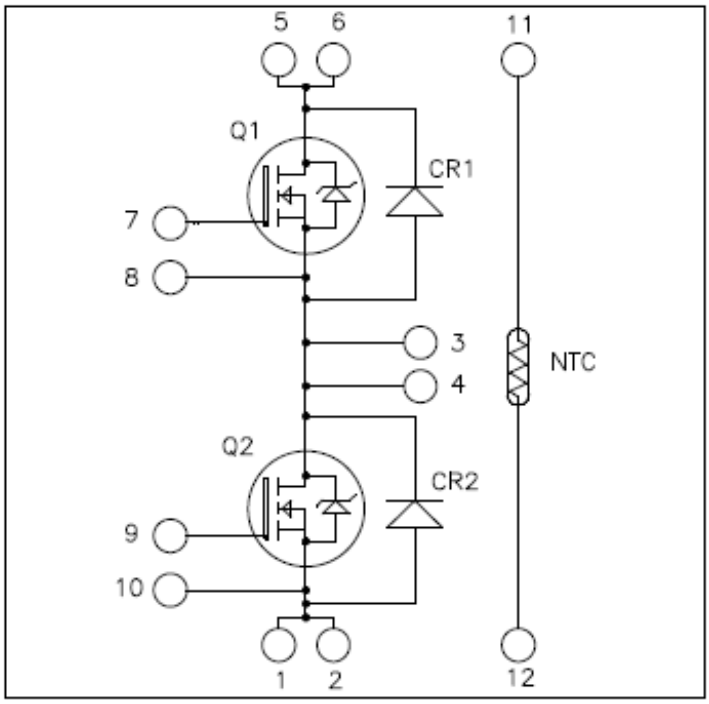


Figure 5.4: Pin diagram of the half-bridge power module

Figure 5.4 shows the detailed pin diagram of the half-bridge power module used in this experiment. Small copper plates are used for the power connection of this module. Appropriate holes are drilled in the copper plates for soldering pins and cable connections. One copper plate is used for pin 5 and 6 and other copper plate is used for pin 1 and 6. Pins 3 and 4 are shorted together by being soldered to a crimped cable. The utmost care has been taken while connecting the cables with screw and washer so that pins connected with the copper plates do not bend. The cables are supported by being tied to the retort clamp with zip ties. The drain-source voltage of each MOSFET is measured and used to calculate the power dissipation which is

assumed to be split equally between the parallel connected MOSFET dies. For the transient case, a current probe is used to measure the current flowing through the MOSFETs and a digital oscilloscope is used to measure the drain-source voltage of each MOSFET and hence allow the power dissipation of the MOSFETs to be calculated.

5.2 Validation of the models

Prior to the further discussion, it is worthwhile to mention the underlying assumptions of this work and their justification.

a) The thickness of the topmost copper layer of the DBC (Direct Bonded Copper) stack is so small compared to its length and width that there is negligible heat spreading in that Copper layer. So, in terms of heat spreading it does not matter whether the Copper layer is continuous or patterned or not.

b) All the power is dissipated by the chips. This is a reasonable assumption because power dissipation in wire bonds, copper traces and electrical terminals is negligible.

c) The sidewalls and the top surface of the module are considered insulated. This assumption is reasonable as almost all the heat generated by the dies is removed through the highly thermally-conductive base plate, with only a small fraction lost (<5%) to radiation and natural convection from the other sides.

d) It is assumed that perfect thermal contact is made between the layers in the module itself and between the module and diffusion block (no voids in solder and thermal grease layers). These are reasonable assumptions for well-assembled modules and heatsink components.

5.2.1 Validation of the steady-state model

The load current is 75 A and is assumed to be shared equally between the parallel-connected MOSFETs. Measuring the V_{ds} of MOSFETs, it is calculated that $P_{\text{MOSFET1}} = P_{\text{MOSFET2}} = 63.75$ W and $P_{\text{MOSFET3}} = P_{\text{MOSFET4}} = 76.87$ W

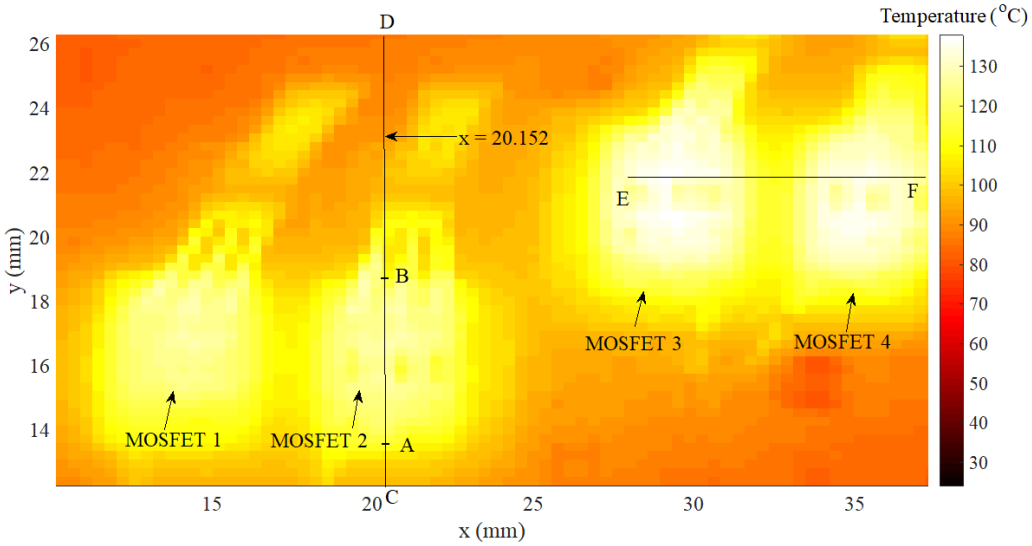


Figure 5.5: Thermal image in the region of interest captured by the IR camera showing lines AB, CD and EF.

Figures 5.5 and 5.6 show the experimental and model temperature distri-

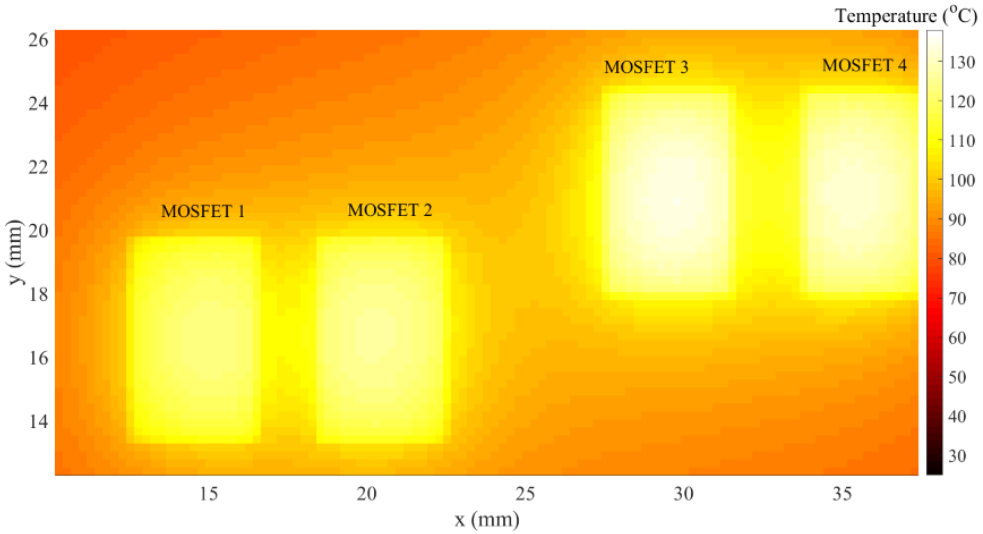


Figure 5.6: Thermal distribution in the region of interest obtained by the model

butions respectively in the region of our interest. Figures 5.7 and 5.8 show the comparisons between the experiment, RNLF method and COMSOL FEM (PVU) model along the lines CD and EF. The error between the experiment and the model or simulation is given by 5.1.

$$e = \frac{T_{\text{ref}} - T_{\text{test}}}{T_{\text{ref}} - 52.6°\text{C}}, \tag{5.1}$$

where $T_{\text{ref}} = T_{\text{exp}}$ for the first two error columns and $T_{\text{ref}} = T_{\text{FEM}}$ and $T_{\text{test}} = T_{\text{RNLF}}$ for the last column of Table 5.1.

In Figures 5.7 and 5.8, the graphs obtained from the RNLF method and COMSOL simulation (PVU) closely match with the corresponding experimental graphs, especially in the middle regions of the MOSFETs. In Figure

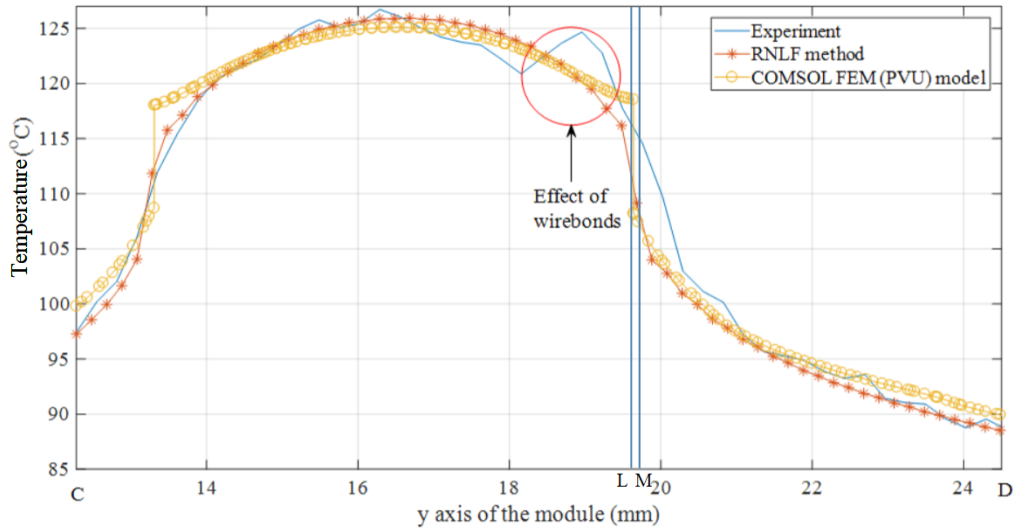


Figure 5.7: Comparison between the experiment, RNLF method and COMSOL FEM (PVU) model along line CD.

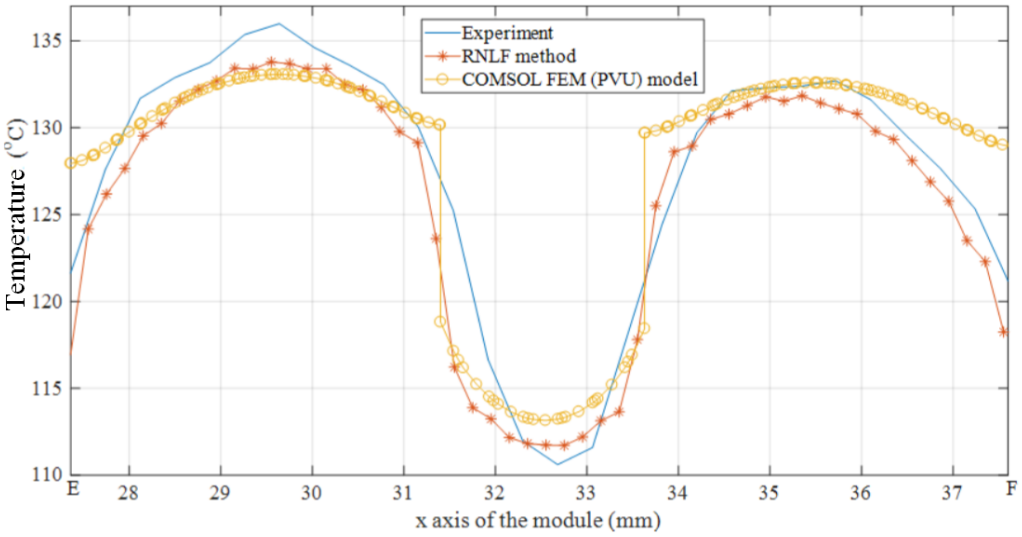


Figure 5.8: Comparison between the experiment, RNLF method and COMSOL FEM (PVU) Model along line EF.

Table 5.1: Comparison between the experiment, COMSOL FEM (PVU) model and the RNLF method

MOSFET No.	Exp. (°C)	FEM (°C)	RNLF (°C)	Error (%) Exp. to FEM	Error (%) Exp. to RNLF	Error (%) FEM to RNLF
2	126.7	125.1	125.9	2.16	1.10	−1.10
3	136.0	133.1	133.8	3.44	2.64	−0.87
4	132.4	132.6	131.8	−0.25	0.75	−1.00

5.7, a peak is observed at the right edge due to the wirebond. In both figures, it is observed that the temperature predicted by FEM (PVU) drops sharply just around the edges of the die. This is because as we traverse along lines CD or EF, we encounter non-homogeneity in terms of thermal conductivities of materials. For example, two points L and M are considered on line CD in Figure 5.7 for the FEM (PVU). L is located on the edge of die and M is located on the patterned Copper layer which does not generate any internal heat in FEM (PVU) model thereby demonstrating lower temperature (approximately 10°C difference) compared to what is observed for M. On the other hand, both L and M are located on the same solder layer in the CAC structure. Therefore, there is no non-homogeneity in terms of material for line CD in the CAC structure and hence less temperature gradient.

In Figure 5.8, a portion of line EF falls on the patterned Copper layer of the FEM (PVU) structure. The same portion falls on the solder layer in the CAC (RNLF) structure. As discussed in the previous chapter, the patterned Copper layer offers higher thermal resistance. Therefore, FEM (PVU)

demonstrates slightly higher temperature than what the CAC (RNLF) structure demonstrates in this region.

From these figures, it can be concluded that the RNLF method captures the experimental temperature distribution better compared to the FEM around the edges of the dies, although FEM (PVU) closely represents the actual power module structure. One potential contribution would be the heat transfer through wire bonds. Another potential contribution might be the presence of black paint which was sprayed several times over the top surface and heat may be transferred from the power module to the ambient through this black paint by conduction, convection and radiation. FEM does not capture these effects, however, RNLF method's CAC structure with its larger solder layer and better heat spreading might be offsetting temperatures (around edges) and indirectly addressing these minor mechanisms.

5.2.2 Validation of transient thermal model

An experiment is carried out to validate the TRNLF model and COMSOL Multiphysics solutions. At the beginning of the experiment, the MOSFETs are held on continuously using a constant gate-source voltage of 20 V. The DC power source is turned on and the resulting transient thermal behaviour is recorded by the camera. A thermal camera with video capturing facility (FLIR A655sc 25°) is used. The experimental set-up with this camera is shown in Fig. 5.9. The MOSFET dies are denoted by M1, M2, M3 and M4 respectively in Fig. 5.10. The midpoint (corresponding to point B in Fig. 8)

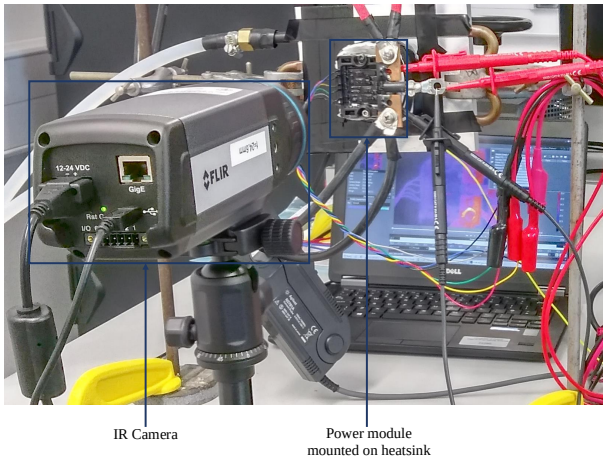


Figure 5.9: Experimental set-up showing the thermal camera and power module

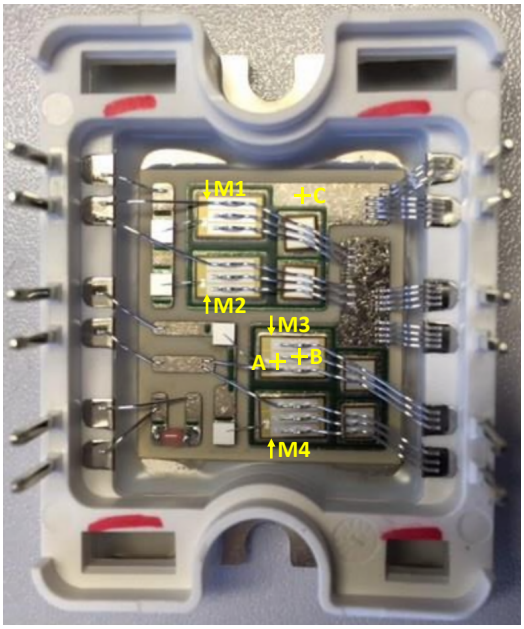


Figure 5.10: Location of MOSFET dies M1-4 and points A, B and C on the power module

of MOSFET 3 is obstructed by a bondwire and so the temperature measured at this point does not accurately effect the real temperature of the die. Hence, a point unobstructed by the bondwire (corresponding to point A) yet close to the midpoint is used instead. A series of snapshots taken from the video data of the power module operating during the thermal transient is presented in Fig. 5.11. It can be seen that the heat generated by the MOSFET dies

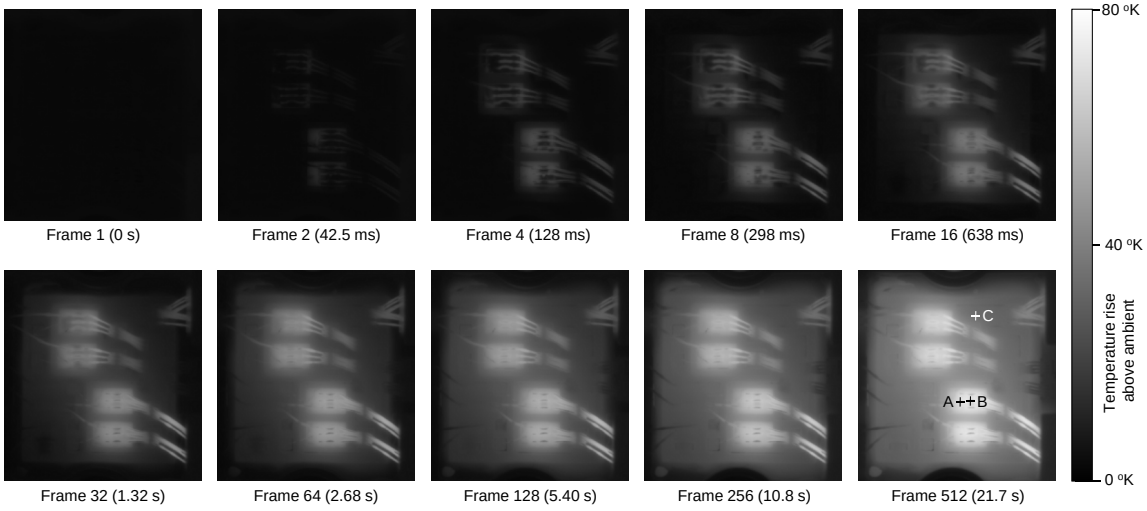


Figure 5.11: A series of frames showing the temperature on the surface of the module

diffuses throughout the module over a period of approximately 3 seconds.

The detector of the camera used in this experiment is described by the manufacturer as having a time constant of approximately 10 ms. It is assumed that this camera works as a first-order low-pass filter with unity gain according to

$$H(s) = \frac{1}{1 + s\tau_c} \tag{5.2}$$

where $\tau_c = 10$ ms is the time constant of the filter.

After the data from the model/simulation are passed through this filter, a close match with the experimental data is achieved, as shown in Figures 5.12 and 5.13. The error between the filtered data and experimental data is given by

$$\text{error}(t) = \frac{T_{\text{exp}}(t) - T_{\text{CACf}}(t)}{T_{\text{exp}}(t) - T_{\text{amb}}} \tag{5.3}$$

where T_{exp} is the instantaneous temperature recorded by the thermal camera and T_{CACf} is the instantaneous temperature generated by the TRNLF CAC model after it has been passed through the low pass filter. The maximum error in the subtransient and transient regions is approximately -5% and 3% respectively. A better match between the experiment and simulation/model

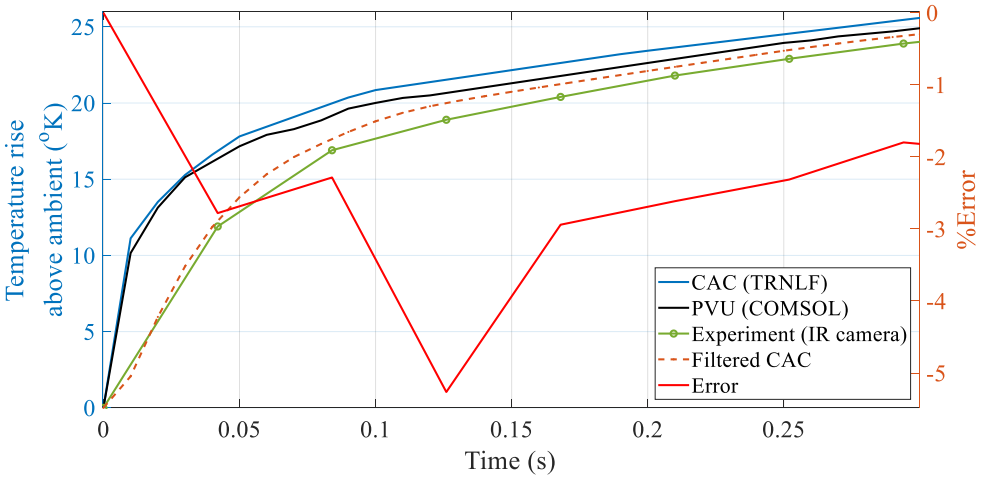


Figure 5.12: Comparison between experimental, simulation and low-pass filtered simulation for point A in the subtransient region

can be expected at points where the temperature change is relatively slow

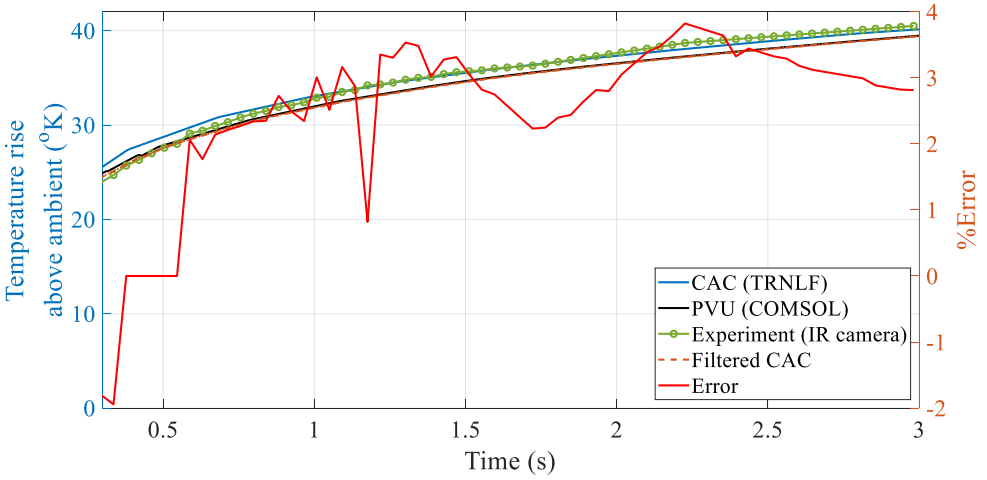


Figure 5.13: Comparison between experimental, simulation and low-pass filtered simulation for point A in the transient region

because the limited frequency response of the thermal camera will have less effect. Such a point is C which is situated on the first copper layer of the DBC substrate. A good match between the experiment and simulation/model is observed for this point (see Fig. 5.14) without the application of the low-pass filter.

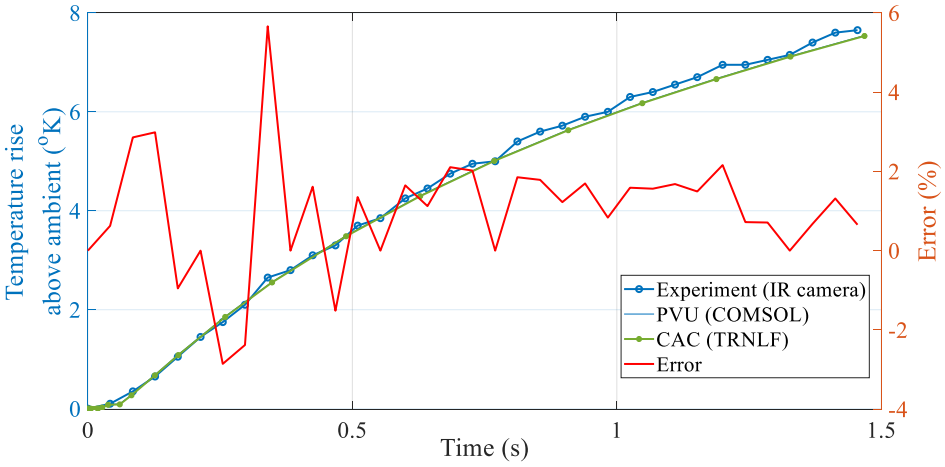


Figure 5.14: Comparison between the experiment and simulation for point C

Chapter 6

Conclusion

In this work, a Fourier-based method for the steady-state thermal modelling of a rectangular N-layer structure, termed the RNLF (Rectangular N-layer Fourier) method, is developed mathematically at first and verified by COMSOL Multiphysics. This method is then successfully applied to a commercial power electronic module with some simplified assumptions. An excellent match is observed between the junction temperature of the chips in the power module and that predicted by the RNLF method despite those assumptions. Based on the steady-state modelling, a semi-analytical method of transient thermal modelling for rectangular N-layered structures, named the TRNLF method, is developed. This method is validated against FEM simulation and experiment using the same commercial power module. An excellent match is observed between the TRNLF method, FEM simulation and experiment after taking into account the time constant of the thermal camera used in

the experiment. It has been found that the RNLF method can compute the temperature response of few points relatively quickly compared to FEM simulations thereby rendering it suitable for fast optimisation of power electronic converters. However, if the number of points increases, the RNLF method may not hold the computational advantage over FEM simulations. On the other hand, the time taken for the calculation of temperature rise by the TRNLF method is dominated by the calculation of eigenvalues. The determination of eigenvalues solely depend on the length, width and thickness of each layer of the rectangular N-layer structure. Therefore, once obtained, the eigenvalues can be used to determine the thermal response for any position of the heat sources relatively quickly. However, like the RNLF method, it may not hold advantage over the FEM simulation in terms of computational time if the number of points for temperature calculation is high.

6.1 Discussion on the merits and limitations of the RNLF and TRNLF methods

the RNLF method is relatively simple because the major mathematical challenge involving this is the determination of Fourier coefficients which can be obtained by taking advantage of the recursive properties of these coefficients. Moreover, it is not iterative which makes it an attractive option for the optimisation. Given the analytical nature of this method, it can be used to quickly estimate the maximum junction temperature of semiconductor

devices with sufficient accuracy.

The TRNLF method is essentially extended upon the RNLF method. Like the RNLF method, its major strength is the relatively straightforward and general expression of Fourier coefficients compared to those of [82]. Moreover, the method does not require a large matrix inversion which is necessary in [83] and [84] or other mesh-based solutions.

Although three-dimensional analytical/semi-analytical methods have been investigated previously, this presents the first exposition of a Fourier based three-dimensional steady-state and transient models for an arbitrary N-layer rectangular structure which is particularly suited to the modelling of power modules. A very important aspect of these models is they can easily take into account the thermal coupling effect of the semiconductor devices.

However, it is important to discuss some limitations of these models. They can be successfully applied to power modules as long as the heat spreading in the DBC stack of the power module is negligible. Mathematically, the separation of variable method used in this work is applicable for the linear system. Therefore, if the material properties are dependent on the temperature, the methods developed in this work may not work well. In that case, an iterative approach may be adopted. In terms of computational time, these methods offer advantage over FEM simulations if the number of points for temperature calculation is low.

6.2 Future work

Some possible extensions of the models of this work are discussed below.

1) The models developed in this work can be used to understand the effect of various parameters, such as - thermal conductivity, diffusivity, convective heat transfer coefficient, length and width of module on the junction temperature of the semiconductor devices of a power module. Therefore, these models may be proved to be a valuable tool for the designers to select different materials for a power module.

2) In this work, an isothermal surface is artificially created to validate the models experimentally with relative simplicity. In future, these models may be experimentally verified in a practical power electronic converter where the value of convection coefficient is finite.

3) The RNLF method might be used to estimate the thickness or thermal conductivity of a particular material (for example the thermal grease layer) given a surface temperature profile in steady-state condition is found experimentally.

4) These models may be particularly useful for the fast thermal optimization of the power module. For example, if the thickness of each layer is considered fixed, then the length, width and the positions of dies can be optimized subject to some electrical and thermo-mechanical constraints. The optimization can be simpler because the both the RNLF and TRNLF methods are smooth with dimensional changes (unlike FEM) and are com-

putationally efficient when evaluating temperatures of only a few points.

5) The reliability of a device depends on the maximum temperature swing in the junction. Therefore, the TRNLF method can be used in the reliability analysis because it can predict maximum swing in the junction temperature.

6) Although the focus of this work has been on power electronic modules, the RNLF and TRNLF methods may be used in other applications in layered structures, assuming that suitable simplifications can be made in these cases. For example, the thermal modelling of discrete chip packages can be done using these methods.

Bibliography

[1] R. W. Erickson and D. Maksimovic, *Fundamentals of power electronics*. Springer Science & Business Media, 2007.

[2] BP, "BP statistical review of world energy june 2014," *BP World Energy Review*, 2014.

[3] I. Pineda, S. Azau, J. Moccia, and J. Wilkes, "Wind in power, 2013 european statistics," *The European Wind Energy Association, Last accessed Jan*, vol. 8, p. 2015, 2014.

[4] E. Aberg, R. Adib, F. Appavou, A. Brown, S. Dwyer, R. Adib, H. Murdock *et al.*, "Renewables 2018. global status report 2018," 2018.

[5] S. Chu, Y. Cui, and N. Liu, "The path towards sustainable energy," *Nature materials*, vol. 16, no. 1, p. 16, 2017.

[6] M. A. Eleffendi, "In-service estimation of state of health of power modules," Ph.D. dissertation, University of Nottingham, 2015.

[7] E. Vagnon, P.-O. Jeannin, J.-C. Crébier, and Y. Avenas, "A bus-bar-like power module based on three-dimensional power-chip-on-chip hybrid integration," *IEEE Transactions on industry applications*, vol. 46, no. 5, pp. 2046–2055, 2010.

[8] J. N. Calata, J. G. Bai, X. Liu, S. Wen, and G.-Q. Lu, "Three-dimensional packaging for power semiconductor devices and modules," *IEEE Transactions on Advanced Packaging*, vol. 28, no. 3, pp. 404–412, 2005.

[9] X. Liu, S. Haque, and G.-Q. Lu, "Three-dimensional flip-chip on flex packaging for power electronics applications," *IEEE transactions on Advanced Packaging*, vol. 24, no. 1, pp. 1–9, 2001.

[10] M. H. Rashid, *Power electronics handbook*. Butterworth-Heinemann, 2017.

[11] Y. Kuromitsu, Y. Nagatomo, K. Akiyama, N. Shibata, and Y. Ikuhara, "Direct-bonded aluminum on aluminum nitride substrates by transient liquid phase bonding," *Journal of the Ceramic Society of Japan*, vol. 125, no. 3, pp. 165–167, 2017.

[12] B. J. Baliga, *The IGBT device: physics, design and applications of the insulated gate bipolar transistor*. William Andrew, 2015.

[13] Y. Liu, *Power electronic packaging: design, assembly process, reliability and modeling*. Springer Science & Business Media, 2012.

[14] B. W. Williams, *Power electronics: devices, drivers and applications*. Macmillan International Higher Education, 1987.

[15] C. Qian, A. M. Gheitaghy, J. Fan, H. Tang, B. Sun, H. Ye, and G. Zhang, "Thermal management on IGBT power electronic devices and modules," *IEEE Access*, vol. 6, pp. 12 868–12 884, 2018.

[16] T. Krebs, S. Duch, W. Schmitt, S. Kötter, P. Prenosil, and S. Thomas, "A breakthrough in power electronics reliability—new die attach and wire bonding materials," in *2013 IEEE 63rd Electronic Components and Technology Conference*. IEEE, 2013, pp. 1746–1752.

[17] P. Mumby-Croft, D. Li, X. Dai, and G. Liu, "High-performance packaging technology for wide bandgap semiconductor modules," *Disruptive Wide Bandgap Semiconductors, Related Technologies, and Their Applications*, p. 65, 2018.

[18] C. Buttay, A. Masson, J. Li, M. Johnson, M. Lazar, C. Raynaud, and H. Morel, "Die attach of power devices using silver sintering–bonding process optimisation and characterization," *Additional Papers and Presentations*, vol. 2011, no. HITEN, pp. 000 084–000 090, 2011.

[19] Y. Yamano, T. Komiyama, M. Takahashi, S. Kobayashi, K. Nitta, and Y. Saito, "Measurement of surface and volume resistivity for alumina ceramics under vacuum condition," in *2008 23rd International Sympo-*

sium on Discharges and Electrical Insulation in Vacuum, vol. 1. IEEE, 2008, pp. 35–38.

[20] P. Auerkari, *Mechanical and physical properties of engineering alumina ceramics*. Technical Research Centre of Finland Espoo, 1996.

[21] T. Kim, J. Kim, R. Dalmau, R. Schlesser, E. Preble, and X. Jiang, "High-temperature electromechanical characterization of AlN single crystals," *IEEE transactions on Ultrasonics, Ferroelectrics, and Frequency control*, vol. 62, no. 10, pp. 1880–1887, 2015.

[22] H. S. Dow, W. S. Kim, and J. W. Lee, "Thermal and electrical properties of silicon nitride substrates," *AIP Advances*, vol. 7, no. 9, p. 095022, 2017.

[23] H. A. Mantooth, K. Peng, E. Santi, and J. L. Hudgins, "Modeling of wide bandgap power semiconductor devices—part I," *IEEE Transactions on Electron Devices*, vol. 62, no. 2, pp. 423–433, 2014.

[24] J. Millán, P. Godignon, X. Perpiñà, A. Pérez-Tomás, and J. Rebollo, "A survey of wide bandgap power semiconductor devices," *IEEE transactions on Power Electronics*, vol. 29, no. 5, pp. 2155–2163, 2013.

[25] F. Blaabjerg, M. Liserre, and K. Ma, "Power Electronics Converters for Wind Turbine Systems," *IEEE Transactions on industry applications*, vol. 48, no. 2, pp. 708–719, 2011.

[26] L. M. Moore and H. N. Post, "Five years of operating experience at a large, utility-scale photovoltaic generating plant," *Progress in Photovoltaics: Research and Applications*, vol. 16, no. 3, pp. 249–259, 2008.

[27] S. Yang, A. Bryant, P. Mawby, D. Xiang, L. Ran, and P. Tavner, "An industry-based survey of reliability in power electronic converters," *IEEE transactions on Industry Applications*, vol. 47, no. 3, pp. 1441–1451, 2011.

[28] P. Lyding, S. Faulstich, B. Hahn, and P. Tavner, "Reliability of the electrical parts of wind energy systems-a statistical evaluation of practical experiences," in *EPE Wind Energy Chapter Symposium*, 2010.

[29] E. Wolfgang, "Examples for failures in power electronics systems, presented at ecpe tutorial on reliability of power electronic systems," *Nuremberg, Germany*, 2007.

[30] F. W. Fuchs, "Some diagnosis methods for voltage source inverters in variable speed drives with induction machines-a survey," in *IECON'03. 29th Annual Conference of the IEEE Industrial Electronics Society (IEEE Cat. No. 03CH37468)*, vol. 2. IEEE, 2003, pp. 1378–1385.

[31] S. Yang, D. Xiang, A. Bryant, P. Mawby, L. Ran, and P. Tavner, "Condition monitoring for device reliability in power electronic converters: A review," *IEEE Transactions on Power Electronics*, vol. 25, no. 11, pp. 2734–2752, 2010.

[32] M. Musallam and C. M. Johnson, "Real-time compact thermal models for health management of power electronics," *IEEE Transactions on Power Electronics*, vol. 25, no. 6, pp. 1416–1425, 2010.

[33] R. John, O. Vermesan, and R. Bayerer, "High temperature power electronics IGBT modules for electrical and hybrid vehicles," *IMAPS, High Temperature Electronics Network (HiTEN)*, pp. 199–204, 2009.

[34] Y. Avenas, L. Dupont, and Z. Khatir, "Temperature measurement of power semiconductor devices by thermo-sensitive electrical parameters—a review," *IEEE transactions on power electronics*, vol. 27, no. 6, pp. 3081–3092, 2011.

[35] N. Baker, M. Liserre, L. Dupont, and Y. Avenas, "Improved Reliability of Power Modules: A Review of Online Junction Temperature Measurement Methods," *IEEE Industrial Electronics Magazine*, vol. 3, no. 8, pp. 17–27, 2014.

[36] H. Huang and P. Mawby, "A lifetime estimation technique for voltage source inverters," *IEEE Transactions on Power Electronics*, vol. 28, no. 8, pp. 4113–4119, 2012.

[37] M. Musallam, C. M. Johnson, C. Yin, H. Lu, and C. Bailey, "In-service life consumption estimation in power modules," in *2008 13th International Power Electronics and Motion Control Conference*. IEEE, 2008, pp. 76–83.

[38] N. Patil, J. Celaya, D. Das, K. Goebel, and M. Pecht, "Precursor parameter identification for insulated gate bipolar transistor (igbt) prognostics," *IEEE Transactions on Reliability*, vol. 58, no. 2, pp. 271–276, 2009.

[39] N. Patil, D. Das, and M. Pecht, "A prognostic approach for non-punch through and field stop igbts," *Microelectronics Reliability*, vol. 52, no. 3, pp. 482–488, 2012.

[40] S. Li, L. M. Tolbert, F. Wang, and F. Z. Peng, "P-cell and n-cell based igbt module: Layout design, parasitic extraction, and experimental verification," in *2011 Twenty-Sixth Annual IEEE Applied Power Electronics Conference and Exposition (APEC)*. IEEE, 2011, pp. 372–378.

[41] A. Wintrich, U. Nicolai, W. Tursky, and T. Reimann, "Application Manual Power Semiconductors," 2011.

[42] S. Kakaç, Y. Yener, and C. P. Naveira-Cotta, *Heat Conduction*. CRC Press, 2018.

[43] U. Drofenik and J. W. Kolar, "Teaching thermal design of power electronic systems with web-based interactive educational software," in *Eighteenth Annual IEEE Applied Power Electronics Conference and Exposition, 2003. APEC'03.*, vol. 2. IEEE, 2003, pp. 1029–1036.

[44] F. Incropera and D. DeWitt, "Introduction to heat transfer," 1985.

[45] K. E. Mortenson, "Transistor junction temperature as a function of time," *Proceedings of the IRE*, vol. 45, no. 4, pp. 504–513, 1957.

[46] D. P. Kennedy, "Spreading resistance in cylindrical semiconductor devices," *Journal of applied physics*, vol. 31, no. 8, pp. 1490–1497, 1960.

[47] A. G. Kokkas, "Thermal analysis of multiple-layer structures," *IEEE Transactions on Electron Devices*, vol. 21, no. 11, pp. 674–681, 1974.

[48] G. N. Ellison, "Maximum thermal spreading resistance for rectangular sources and plates with nonunity aspect ratios," *IEEE Transactions on Components and Packaging Technologies*, vol. 26, no. 2, pp. 439–454, 2003.

[49] Y. Muzychka, J. Culham, and M. Yovanovich, "Thermal spreading resistance of eccentric heat sources on rectangular flux channels," *Journal of Electronic packaging*, vol. 125, no. 2, pp. 178–185, 2003.

[50] Y. S. Muzychka, K. R. Bagnall, and E. N. Wang, "Thermal spreading resistance and heat source temperature in compound orthotropic systems with interfacial resistance," *IEEE Transactions on Components, Packaging and Manufacturing Technology*, vol. 3, no. 11, pp. 1826–1841, 2013.

[51] G. N. Ellison, "Thermal analysis of microelectric packages and printed circuit boards using an analytic solution to the heat conduction equa-

tion," *Advances in Engineering Software*, vol. 22, no. 2, pp. 99–111, 1995.

[52] J. Geer, A. Desai, and B. Sammakia, "Heat conduction in multilayered rectangular domains," *Journal of Electronic Packaging*, vol. 129, no. 4, pp. 440–451, 2007.

[53] N. Zommer and D. Feucht, "Analytical thermal response of a multiple-layer device under the semi-infinite approximation," *IEEE Transactions on Electron Devices*, vol. 25, no. 4, pp. 441–448, 1978.

[54] R. David, "Computerized thermal analysis of hybrid circuits," *IEEE Transactions on Parts, Hybrids, and Packaging*, vol. 13, no. 3, pp. 283–290, 1977.

[55] D. Guan, M. Marz, and J. Liang, "Analytical solution of thermal spreading resistance in power electronics," *IEEE Transactions on Components, Packaging and Manufacturing Technology*, vol. 2, no. 2, pp. 278–285, 2012.

[56] I. R. Swan, A. T. Bryant, and P. A. Mawby, "Fast thermal models for power device packaging," in *2008 IEEE Industry Applications Society Annual Meeting*. IEEE, 2008, pp. 1–8.

[57] I. Swan, A. Bryant, P. A. Mawby, T. Ueta, T. Nishijima, and K. Hamada, "A fast loss and temperature simulation method for power

converters, part II: 3-D thermal model of power module," *IEEE Transactions on Power Electronics*, vol. 27, no. 1, pp. 258–268, 2011.

[58] F. Masana, "A new approach to the dynamic thermal modelling of semiconductor packages," *Microelectronics Reliability*, vol. 41, no. 6, pp. 901–912, 2001.

[59] ——, "Thermal characterisation of power modules," *Microelectronics Reliability*, vol. 40, no. 1, pp. 155–161, 2000.

[60] S. S. Wen and G.-Q. Lu, "Finite element modeling of heat transfer and thermal stresses for three-dimensional packaging of power electronics modules," in *Proceedings IPEMC 2000. Third International Power Electronics and Motion Control Conference (IEEE Cat. No. 00EX435)*, vol. 1. IEEE, 2000, pp. 496–501.

[61] W. E. Newell, "Transient thermal analysis of solid-state power devices–making a dreaded process easy," *IEEE Transactions on Industry Applications*, no. 4, pp. 405–420, 1976.

[62] M. März and P. Nance, "Thermal modeling of power electronic systems," *Infineon Technologies AG Munich*, 2000.

[63] V. Székely and T. Van Bien, "Fine structure of heat flow path in semiconductor devices: a measurement and identification method," *Solid-State Electronics*, vol. 31, no. 9, pp. 1363–1368, 1988.

[64] L. Weinberg, *Network analysis and synthesis*. McGraw-Hill New York, 1962, vol. 17.

[65] P. R. Strickland, "The thermal equivalent circuit of a transistor," *IBM Journal of research and development*, vol. 3, no. 1, pp. 35–45, 1959.

[66] A. Zanin, "SKiM IGBT modules," *Mounting Instructions: Semikron*, 2014.

[67] D. Domes and U. Schwarzer, "IGBT-module integrated current and temperature sense features based on sigma-delta converter," *PCIM 2009, Nürnberg, Germany*, 2009.

[68] P.-L. Doumergue and C. de Magret, "Using NTC temperature sensors integrated into power modules," *Advanced Power Technology*, 2004.

[69] I. Bakun, N. Čobanov, and Ž. Jakopović, "Real-time measurement of IGBT's operating temperature," *Automatika*, vol. 52, no. 4, pp. 295–305, 2011.

[70] Z. Jakopovic, Z. Bencic, and F. Kolonic, "Important properties of transient thermal impedance for mos-gated power semiconductors," in *ISIE'99. Proceedings of the IEEE International Symposium on Industrial Electronics (Cat. No. 99TH8465)*, vol. 2. IEEE, 1999, pp. 574–578.

[71] N. Baker, M. Liserre, L. Dupont, and Y. Avenas, "Junction temperature measurements via thermo-sensitive electrical parameters and their

application to condition monitoring and active thermal control of power converters," in *IECON 2013-39th Annual Conference of the IEEE Industrial Electronics Society*. IEEE, 2013, pp. 942–948.

[72] L. Dupont, Y. Avenas, and P.-O. Jeannin, "Comparison of junction temperature evaluations in a power IGBT module using an IR camera and three thermosensitive electrical parameters," *IEEE Transactions on Industry Applications*, vol. 49, no. 4, pp. 1599–1608, 2013.

[73] H. Kuhn and A. Mertens, "On-line junction temperature measurement of igbts based on temperature sensitive electrical parameters," in *2009 13th European Conference on Power Electronics and Applications*. IEEE, 2009, pp. 1–10.

[74] É. Pinet, S. Ellyson, and F. Borne, "Temperature fiber-optic point sensors: Commercial technologies and industrial applications," *FISO Technologies*, vol. 46, 2010.

[75] B. Meggitt, "Fiber optics in sensor instrumentation," in *Instrumentation Reference Book*. Elsevier, 2003, pp. 170–199.

[76] M. N. Ozisik, *Boundary value problems of heat conduction*. Courier Corporation, 2002.

[77] H. S. Carslaw and J. C. Jaeger, "Conduction of heat in solids," *Oxford: Clarendon Press, 1959, 2nd ed.*, 1959.

[78] J. Zhu, H. Park, J.-Y. Chen, X. Gu, H. Zhang, S. Karthikeyan, N. Wendel, S. A. Campbell, M. Dawber, X. Du *et al.*, "Revealing the origins of 3D anisotropic thermal conductivities of black phosphorus," *Advanced Electronic Materials*, vol. 2, no. 5, p. 1600040, 2016.

[79] M. N. Ozisik, *HEAT CONDUCTION*, 1st ed. New York: JOHN WILEY AND SONS, 1980.

[80] J. W. Brown and R. V. Churchill, *Fourier series and boundary value problems*. McGraw-Hill New York, 2001, vol. 6.

[81] K. R. Choudhury and D. J. Rogers, "Steady-State Thermal Modeling of a Power Module: An n-layer fourier approach," *IEEE Transactions on Power Electronics*, vol. 34, no. 2, pp. 1500–1508, 2019.

[82] V. Kadambi and N. Abuaf, "An analysis of the thermal response of power chip packages," *IEEE Transactions on Electron Devices*, vol. 32, no. 6, pp. 1024–1033, 1985.

[83] W. Huang, S. Ghosh, S. Velusamy, K. Sankaranarayanan, K. Skadron, and M. R. Stan, "Hotspot: A compact thermal modeling methodology for early-stage VLSI design," *IEEE Transactions on Very Large Scale Integration (VLSI) Systems*, vol. 14, no. 5, pp. 501–513, 2006.

[84] A. Sridhar, A. Vincenzi, D. Atienza, and T. Brunschwiler, "3D-ICE: A compact thermal model for early-stage design of liquid-cooled ICs," *IEEE Transactions on Computers*, vol. 63, no. 10, pp. 2576–2589, 2013.